ISTANBUL TECHNICAL UNIVERSITY ★ GRADUATE SCHOOL OF SCIENCE ENGINEERING AND TECHNOLOGY

DETECTION OF URBAN EXPANSION IN TURKEY BY USING SPECTRALLY UNMIXED LANDSAT IMAGES AND NIGHTTIME DMSP-OLS IMAGES

Ph.D. Thesis

Cihan UYSAL

Department of Geomatics Engineering

Geomatics Engineering Programme

Thesis Advisor: Prof. Dr. Derya MAKTAV
Anabilim Dalı :   Herhangi Mühendislik, Bilim
Programı :   Herhangi Program

JUNE 2015

DETECTION OF URBAN EXPANSION IN TURKEY BY USING SPECTRALLY UNMIXED LANDSAT IMAGES AND NIGHTTIME DMSP-OLS IMAGES

Ph.D. THESIS

Cihan UYSAL
(501092605)

Department of Geomatics Engineering

Geomatics Engineering Programme

Thesis Advisor: Prof. Dr. Derya MAKTAV
Anabilim Dalı :   Herhangi Mühendislik, Bilim
Programı :   Herhangi Program

JUNE 2015

İSTANBUL TEKNİK ÜNİVERSİTESİ ★ FEN BİLİMLERİ ENSTİTÜSÜ

TÜRKİYE'DE KENTSEL YAYILMANIN, SPEKTRAL UNMIXED LANDSAT GÖRÜNTÜLERİNDEN VE DMSP-OLS GECE GÖRÜNTÜLERİNDEN SAPTANMASI

DOKTORA TEZİ

Cihan UYSAL
(501092605)

Geomatik Mühendisliği Anabilim Dalı

Geomatik Mühendisliği Programı

Tez Danışmanı: Prof. Dr. Derya MAKTAV
Anabilim Dalı :   Herhangi Mühendislik, Bilim
Programı :   Herhangi Program

HAZİRAN 2015

Cihan Uysal, a **Ph.D.** student of ITU **Institute of / Graduate School of Science Engineering and Technology** student ID 501092605, successfully defended the **thesis/dissertation** entitled "**DETECTION OF URBAN EXPANSION IN TURKEY BY USING SPECTRALLY UNMIXED LANDSAT IMAGES AND NIGHTTIME DMSP-OLS IMAGES**", which he prepared after fulfilling the requirements specified in the associated legislations, before the jury whose signatures are below.

Thesis Advisor :   **Prof. Dr. Derya MAKTAV**
İstanbul Technical University

Jury Members :   **Prof. Dr. Filiz SUNAR**
İstanbul Technical University

Prof. Dr. Bülent BAYRAM
Yıldız Technical University

Assoc. Prof. Dr. Hayriye Eşbah TUNÇAY
İstanbul Technical University

Assoc. Prof. Dr. Hüseyin TOPAN
Bülent Ecevit University

Date of Submission : 04 June 2015
Date of Defense :   24 June 2015

To my family,

FOREWORD

June 2015

Cihan UYSAL
Geomatics Engineer

x

TABLE OF CONTENTS

ABBREVIATIONS

AVHRR   : Advanced Very High Resolution Radiometer
AVIRIS   : Advanced Visible/Infrared Image Spectrometer
CC   : Cubic Convolution
D   : Dark Surface
DMSP   : Defense Meteorological Satellites Program
DN   : Digital Number
DSVD   : Difference of S-V-D layers
ETM   : Enhanced Thematic Mapper
GIS   : Geographic Information Systems
GOES   : Geostationary Operational Environmental Satellite
IR   : Infrared
ISODATA   : Iterative Self-Organized Data Analysis Technique Algorithm
LCLU   : Land Cover and Land Use
LSU   : Linear Spectral Unmixing
MSS   : Multispectral Scanner
NASA   : National Aeronautics and Space Administration
NDVI   : Normalized Difference Vegetation Index
NGDC   : National Geophysical Data Center
NIR   : Near Infrared
NN   : Nearest Neighbor
NOAA   : National Oceanic and Atmospheric Administration
OLI   : Operational Land Imager
OLS   : Operational Linescan
PCA   : Principal Component Analysis
S   : Substrate
SMA   : Spectral Mixture Analysis
TM   : Thematic Mapper
ToA   : Top of Atmosphere
USGS   : United States Geological Survey
UTM   : Universal Transverse Mercator
V   : Vegetation
VIS   : Vegetation-Impervious Surface-Soil
WGS   : World Geodetic System

LIST OF TABLES

LIST OF FIGURES

DETECTION OF URBAN EXPANSION IN TURKEY BY USING SPECTRALLY UNMIXED LANDSAT IMAGES AND NIGHTTIME DMSP-OLS IMAGES

SUMMARY

One of the main impacts of globalization has been the rapid expansion of urban areas. Urban areas are dynamic, with the potential to continually increase in size as horizantally and/or vertically. Over the last few decades, urbanization have increased in Turkey and it gained momentum after 1980s. Immigration from rural areas to cities due to the limited agriculture economy, and insufficient job and education opportunities played a fundamental role in this increase. Sometimes urban growth cannot be controlled; in such cases, expanding urban areas may damage natural resources and instigate land cover and land use change. Therefore, urban areas should be monitored periodically. Remote sensing is a reliable tool to monitor urban growth.

In this study, Istanbul, Ankara, Izmir, Izmit, Bursa, Kayseri and Manisa which are developed and developing cities of Turkey, were selected as the study areas. As a method, the study areas were valuated for urban growth using spectral mixture analysis method. Remotely sensed images provide a fundamental tool of land cover and land use maps. However, this source lacks spatial detail because each pixel contains only one value for the denoted area. Heterogeneous areas, including urban areas, may therefore result in misclassifications. By unmixing a pixel into its components, it is possible to enable a more accurate classification of the area. Spectral mixture analysis uses linear mixture models to provide physical representations of land surface reflectance. In this study, spectral mixture analysis method was applied to Landsat images for three different dates (1984 or 1987, 1999 and 2009 or 2010). This method also was applied to determine and analyse seismic hazard and effects of it in Istanbul and Izmit. In this study, nighttime images acquired by Defense Meteorological Satellites Program/Operational Linescan System have been also used. Especially these images have provided important assistance to determine urban areas. The results of the study show changes in land cover and urban growth areas, which were determined using spectral mixture analysis as an alternative method.

TÜRKİYE'DE KENTSEL YAYILMANIN, SPEKTRAL UNMIXED LANDSAT GÖRÜNTÜLERİNDEN VE DMSP-OLS GECE GÖRÜNTÜLERİNDEN SAPTANMASI

ÖZET

Kentleşme 1950'lerden beri dünyada hızla artmaktadır. Türkiye'de ise kentleşme 1980'lerden sonra ivme kazanmıştır. Tarım ekonomisinin sınırlı olması, iş ve eğitim fırsatlarının yetersiz olması vb. nedenlerden dolayı kırsal alanlardan kentlere olan göçler bu artışta temel rol oynamıştır. Bu göçler, başta İstanbul olmak üzere, Ankara, İzmir, Bursa ve Antalya gibi sanayileşmenin ve/veya turizmin ön planda olduğu büyük kentlere doğru olmuştur. Özellikle de gelişmekte olan ülkeler için kentleşme, kentsel büyümenin sürdürülebilmesi ve ülke kalkınması açısından gerekli bir olgudur. Fakat bu büyüme kontrollü ve planlı bir şekilde olmalıdır, aksi durumda kentlerin kontrolsüz büyümesi, plansız alt yapılaşma ve doğal kaynakların yanlış kullanılması birçok çevresel soruna sebep olabilir. Bu yüzden, dinamik yapıya sahip olan kentsel alanların periyodik olarak izlenmesi gerekir.

Uydu ve bilgi teknolojilerindeki ilerlemeler sayesinde uzaktan algılama verileri ve teknikleri birçok alanda kullanılmaktadır. Bu veriler, sağladıkları güncel mekansal bilgi nedeniyle kentsel çevrenin izlenmesinde karar vericiler ve yöneticiler için vazgeçilmez bir kaynak olmaktadır. Kentsel çevredeki değişimlerin izlenmesi, 'maximum likelihood' ve 'Isodata' tekniklerini kullanan piksel tabanlı sınıflandırma yöntemleriyle elde edilen arazi örtüsü ve arazi kullanımı haritalarıyla da sağlanabilmektedir. Fakat elde edilen bu tematik haritalar, özellikle de düşük mekansal çözününürlüklü uydu verilerinin kullanıldığı heterojen alanlarda hatalı sınıflandırma sonuçlarına yol açabilmektedir, çünkü bu yaklaşımlarda her bir piksel yalnızca bir sınıf değeriyle temsil edilmektedir. Bu yüzden alt piksel seviyesinde arazi örtüsü ve arazi kullanımı haritalamasının daha doğru sonuçlar ve analizler ortaya çıkaracağı benimsenmiştir.

Bu çalışmada kullanılan spektral karışım analizi (spectral mixture analysis) ile her bir piksel, kendisini oluşturan uç üyeler (endmember) tarafından temsil edilmektedir. Lineer karışım modeli üzerine kurgulu bu analiz ile yeryüzü, 'substrate', 'green vegetation' ve 'dark surfaces' spektral endmember yansıtımları cinsinden daha hassas bir biçimde temsil edilmektedir. Alternatif bir yöntem olarak benimsenen bu analiz ile elde edilen arazi örtüsü ve arazi kullanımı haritalarında her sınıf daha kapsamlı bilgi verecektir. Bu yöntem sayesinde özellikle de heterojen alanlara ait haritalarda, belirlenen sınıflara ait yoğunluk değerleri daha hassas bir biçimde belirlenecektir.

'Substrate' endmember yansıtımı yeryüzünde bulunan toprak, taş ve beton yüzeylere ait spektral yansıtımları kapsamaktadır. 'Green vegetation' endmember yansıtımları ise yeşil bitki örtüsünün hakim olduğu alanlara karşılık gelmektedir. 'Dark surfaces' endmember yansıtımı, diğer iki endmember yansıtımınına göre daha karmaşık bir yapıya sahiptir. Yeryüzünde su ile örtülü yüzeylerin tamamında veya büyük bir kısmında 'dark surfaces' endmember yansıtımı baskındır. Bu yansıtım değeri ayrıca doğal ve yapay objelerin gölgelerine karşılık gelen koyu yüzeylerin tanımlanmasında

da kullanılmaktadır. Harita üzerinde karmaşık piksellerin yoğun olduğu alanlar yeryüzünde heterojen yapının hakim olduğu alanlara karşılık gelmektedir. Böyle durumlarda spektral karışım analizi yöntemine ihtiyaç duyulmaktadır. Bu yöntem farklı tarihlere ait atmosferik kalibre edilmiş Landsat görüntülerine uygulanarak 'substrate-green vegetation-dark surfaces' haritalar elde edilmiştir. Farklı tarihlere ait bu haritaların birbirlerinden farkı alınarak endmember yansıtımında değişimleri gösteren fark haritaları elde edilmiştir.

Çalışmada elde edilecek temel sınıfları belirlemek amacıyla global endmember değerler kullanılmıştır. Bu değerler dünya üzerindeki farklı coğrafi bölgelere ait Landsat alt görüntülerinden elde edilmiştir. Genel anlamda arazi örtüsü ve arazi kullanımının belirlenmesi için birçok ülkede kullanılmış olan bu endmember değerleriyle Türkiye'de ilk kez kullanılmış olacaktır.

Bu çalışmada, kentsel gelişim alanlarının belirlenebilmesi amacıyla uydulardan elde edilen gece zamanlı görüntüler de kullanılmıştır. 'Defense Meteorological Satellites Program/Operational Linescan System' tarafından yeryüzünün büyük bir kısmı gece ışıklarını kaydetmektedir. 1992 yılından itibaren dijital olarak yıllık bazda mevcut olan bu veriler büyük kentlerin, kentsel gelişim süreci konusunda bilgi vermektedir. Spektral karışım analizi sonucunda 'substrate' alan olarak belirlenen her alan yeryüzünde kentsel alana karşılık gelmeyebilir. Böyle durumlarda uydulardan elde edilen gece zamanlı görüntüler değerlendirme aşamasında kullanılmaktadır. Ayrıca gece zamanlı düşük mekansal çözünürlüklü bu uydu verileri özellikle de büyük kentlere ait kentsel büyüme aksları ve yönleri hakkında bilgi vermektedir.

Türkiye'nin en çok gelişmiş ve gelişmekte olan kentleri; İstanbul, Ankara, İzmir, İzmit, Bursa, Kayseri ve Manisa çalışma alanı olarak seçilmiştir. Çalışmada spektral karışım analizi, 1984-1987, 1999-2000 ve 2009-2010 yıllarına ait Landsat görüntülerine uygulanmıştır. Ayrıca 1992, 1999 ve 2009 yıllarına ait 'Defense Meteorological Satellites Program/Operational Linescan System' verileri de kullanılmıştır. Elde edilen sonuçlara göre, arazi örtüsündeki ve arazi kullanımındaki değişimler ve özellikle de kentsel büyüme alanları spektral karışım analizi yöntemi kullanılarak saptanmıştır.

Spektal karışım analizi yönteminin uygulanması sonucunda elde edilen kentsel gelişim bölgelerinin doğruluğunu tespit etmek amacıyla yüksek mekansal çözünürlüklü uydu görüntüleri kullanmıştır. Bu çalışmada elde edilen sonuçların doğruluğunun karşılaştırılmasında kullanılan yüksek mekansal çözünürlüklü bu görüntüler sadece İstanbul çalışma alanı için kullanılmıştır. Genellikle 2002 ve 2011 yıllarına ait bu görüntüler, spektral karışım analizi sonucunda elde edilen kentsel büyüme alanlarının doğruluğunun test edilmesinde kullanılmıştır. Yüksek mekansal çözünürlüklü uydu verileri 2000'li yıllardan sonra yaygınlaşmaya başlamıştır. Bu nedenle çalışma alanını oluşturan çoğu şehir için 2000-2002 zaman dilimine ait yüksek çözünürlüklü veri bulunamamıştır. Fakat kentleşme, diğer arazi örtüsü ve arazi kullanımı açısından kompleks bir yapıya sahip olan İstanbul için yeterince doğrulama yapılmıştır. Aynı şekilde İstanbul için, 2000 yılı sonrasında oluşan kentsel alanları gösteren 'substrate' harita için doğruluk analizi yapılmıştır.

Çalışma sonucunda kentsel büyüme alanlarının yanı sıra spektral karışım analizi metotunun doğal afetlerin zararlarının belirlenmesi ve analizinde de kullanılabilirliği test edilmiştir. Bu amaç doğrultusunda 1999 yılında İzmit'te meydana gelen deprem öncesi ve sonrası analiz edilmiştir. Depremde zarar gören ve su altında kalan alanlar spektral karışım analizi yöntemi kullanılarak belirlenmiştir.

Özellikle de 'dark surfaces' değerinin değişimi doğal afet zararlarının tespitinde etkin rol oynadığı tespit edilmiştir. Arazi üzerinde spektral örnek alan toplamaksızın, sadece global endmember seti kullanılarak spektral karışım analizi metotu farklı çalışma alanlarına uygulanabilmektedir.

1. INTRODUCTION

Maintaining the urban growth is an essential feature for developing countries. However, this growth should be in a controlled and planned manner, or otherwise it may cause many environmental problems. In Turkey, population living in cities was 25% in 1950, and this ratio increased to 43% in 1980 and to 76% in 2010 (TurkStat, 2014). Therefore, Turkey is among the leading countries of the world with its urban population and urban population increase ratio. Turkey has big cities like primarily Istanbul, Ankara, Izmir, Adana, Bursa and Antalya which allow immigrants and where urban change is being experienced (Maktav and Erbek, 2005). Especially in Istanbul, the most crowded city of Turkey, the population increased by almost three times during the last 30 years. Compared to other cities, Istanbul has more population, and industrial and trade areas. Immigration to Istanbul continues because it provides better economic opportunities than most of the other cities in Turkey (Geymen and Baz, 2008).

This rapid increase in urbanization usually causes problems such as unplanned infrastructure and uncontrolled urban growth. This unplanned and uncontrolled urbanization may also lead the misusage of and damage to green areas, cultivated areas and natural resources like water sources (Al-Rawashdeh and Saleh, 2006). Therefore, the urban environment and especially natural resources should be constantly monitored and kept under control. Remote sensing data and techniques are indispensable resources for decision makers and rulers to monitor urban environment thanks to the current spatial information they provide (Maktav et al., 2005).

In obtaining the land cover and land use (LCLU) maps with these data and technologies, generally "iterative self-organizing data analysis technique algorithm (isodata)" and "maximum likelihood" classification techniques are used. However, each pixel is only represented by one class value in such techniques. This may result in low accuracy classification results for mixed pixels corresponding to some heterogeneous areas like urban areas, whereas it is accurate for pure pixels which are corresponding to homogeneous areas on earth (Jensen, 1996; Palanisamy et al., 2006). Because of the low spatial resolution of the remote sensing satellite data used to map

1

the LCLU in global scale, accuracy of these maps are also limited. Thus, there are various approaches for LCLU mapping at lower pixel level. Among these, the linear spectral unmixing (LSU) model is adopted as the most common and well performed approach (Adams et al., 1995; Quarmby et al., 1992; Settle and Drake, 1993). The spectral mixture analysis (SMA) method is built on linear spectral unmixing model and mixed pixels are represented as they are calculated in percentages in determined endmember projections (Adams et al., 1993; Gillespie et al., 1990). In this model, substrate (S) endmember represents a variety of soil, rock and impervious surfaces, vegetation (V) endmember represents green vegetation areas. Dark surface (D) endmember represents water covered, shadowing and nonreflective areas.

By applying radiometric calibration to Landsat Thematic Mapper (TM) and Enhanced Thematic Mapper (ETM) images, digital number (DN) values were first converted to radiance and then to reflectance values. The SMA method was applied to these images calibrated radiometrically using the global endmember reflectances. Substrate-vegetation-dark surfaces (SVD), difference SVD (DSVD) and tri-temporal substrate maps were prepared using Landsat data from 1984 or 1987, 1999 or 2000 and 2009 or 2010 and urban change areas were determined. To determine urban areas, night-time images have been acquired Defense Meteorological Satellites Program/Operational Linescan System (DMSP/OLS) were used for the study. Also, image pairs with high spatial resolution were used to test accuracy of DSVD maps generated.

1.1 Purpose of Thesis

The purpose of this study is to map and analyze the LCLU changes and urban growth areas in selected study areas using the multitemporal spectral mixture analysis method. Some cities like Izmit and Istanbul which have a strategical location, urbanization has been increasing, although they have been on seismic zone. Therefore, urbanization in these cities should be monitored and controlled using reliable data and methods. In this study, apart from the other usual methods SMA method was used first time for the study areas. This method was applied to the study areas and provided faster results not only urban growth but also the other LCLU changes. As an alternative method, SMA was also used for natural disaster applications in the study.

1.2 Literature Review

Although challenged by the spectral and spatial heterogeneity of urban regions (Jensen and Cowen 1999; Herold et al., 2004), remote sensing seems to be a suitable source of urban data to support studies which are related to analysis of urban growth and sprawl (Donnay et al., 2001). In terms of analyzing urban growth, Batty and Howes (2001) stated that remote sensing technology can provide a unique perspective on growth, land cover and land use change processes. Data acquired through remote sensing are consistent over large regions and over time, and can provide detailed information at a great variety of geographic scales. The information derived from this technology can help to model the urban environment, leading to developed understanding that benefits applied urban planning and management (Longley and Mesev 2000; Longley et al., 2001). In the recent years, remote sensing data and geographic information system (GIS) techniques are widely being used for mapping, monitoring, analysing and modeling the urban growth, land cover and land use change (Parker et al., 2003). Taragi and Pundir (1997) analyzed the urban growth and expansion of Lucknow city for the period between 1972 and 1992. They had nine major land cover and land use classes from four temporal remote sensing images via visual interpretation and manual mapping. Finally, they generated a built-up change map and computed built-up growth rate. Using these land cover and land use maps, they tried to determine the expansion intuitively. Nevertheless, their sprawl-map is really a built-up change map and this research did not quantify the urban sprawl so their characterization of sprawl was limited to rapid growth. Sudhira et al. (2004) carried out a research to identify the dynamics of urban sprawl and they wanted to model the future sprawl using remote sensing and other dataset. They considered a study area of 434.2 km^2 in Mangalore-Udupi region in Karnataka state between 1972 and 1999. They classified satellite images to detect built-up information for the year 1999. Also, built-up information of 1972 had been extracted from Survey of India topographical maps. They had analyzed the urban sprawl via built-up growth versus population growth, Shannon's entropy, population density, built-up density, annual population growth rate, distance from Mangalore and Udupi. In the study, metrics analysis had been performed using a 3x3 kernel window. Finally, they had estimated the built-up area for the years 2020 and 2050 by using regression analysis. Nevertheless, although the title claimed for the modeling of urban sprawl, ultimately it caused a sum increase of built-up area for

future. Actually it is difficult to map urban sprawl and growth accurately because urban areas are usually heterogenous areas and they cover mixed classess. There have been many examples in recent literature of procedures to overcome the misclassification issues. For instance, the VIS (vegetation-impervious surface-soil) index developed for urban classification in Salt Lake City (Ridd, 1995) and the use of the combination of multiple sensors like that of the ERS-1 SAR and Landsat TM described by Kuplich et al. (2000).

As the SMA is very popular and accurate sub-pixel classification technique, many researchers have used it to classify remote sensing data and estimate the class proportions for various applications. Linear SMA technique was first proposed by Adams and Smith (1986) to compare image spectra with laboratory spectra and they calculated the proportion of the classes in the image. Tompkins et al. (1997) stated that each pixel is a mixture of different endmembers and it is a linear combination of endmember spectra. According to Lunetta (1998), SMA was developed for interpreting high spectral resolution Advanced Visible/Infrared Image Spectrometer (AVIRIS) data and was later expanded to be used with Landsat data. Lelong et al. (1998) have studied a LSU model integrated with principal component analysis (PCA) for crop monitoring and they proved that a significant amount of information can be collected with a limited number of spectral bands by using LSU method. A research was done by Gong and Zhang (1999) on Linear SMA and it was related to address the validity and noise sensitivity of the LSU algorithm. They used two different algorithms of LSU: Unconstrained method based on singular value decomposition and the other method, constrained method, based on nonnegative least squares, to test their sensitivity to noise. According to the result, both methods were very sensitive to noise. Zhu and Tateishi (2001) investigated the possibility of using LSU to generate fraction images using normalized difference vegetation index (NDVI) time series data. They compared the result of a linear spectral unmixing method with usual methods like maximum likelihood and minimum distance on multitemporal Landsat TM data and National Oceanic and Atmospheric Administration-Advanced Very High Resolution Radiometer (NOAA-AVHRR) monthly composite NDVI data. They acquired that LSU method gives better results than the usual methods because SMA method based on LSU covers physical information as the fraction of each component within a pixel. Haertel and Shimabukuro (2005) used the Linear Spectral Mixture Model for low

spatial resolution data to evaluate the class proportion. They concluded the method is reliable for the low spatial resolution images and the method is appropriate for regional and global studies as well. There have been many researches using LSU method in different applications. Small (2001a) used Landsat TM images to estimate urban vegetation abundance in New York City and monitor changes over one year Small (2002) by using LSU and pseudoinvariant endmembers. A research done by Small (2004) showed that a SMA of global composite of 30 spectrally diverse LANDSAT ETM subscenes provides that a wide variety reflectance spectra can be accurately represented as linear combinations of S, V and D endmembers. Small and Milesi (2013) investigated global endmembers provided the basis for a standardized spectral model. They also compared LANDSAT and WorldView-2 endmember fractions and they concluded that endmember fractions shows strong linear scaling.

1.3 Hypothesis

Remote sensing technologies provide important analyses tools for urban applications. Accurate image analysis and interpretation are very important for urban areas, which are generally heterogeneous areas. However, traditional classification methods have some challenges like spectral mixing. Standardized multitemporal spectral mixture model has provided better image process and analysis for urban applications. Urban growth was analysed first time using SMA method with DMSP/OLS images. Moreover, global endmembers have been used and tested first time for Turkey. This alternative method apart from other usual analysis methods has provide faster, more detailed information about urban growth.

2. DIGITAL IMAGE PROCESSING

2.1 Digital Image

An image can be defined as two dimensional representation of objects from a three dimensional space. Digital image consists of picture elements called pixels which includes brightness value and address. For passive sensing, the obtained table of numbers in the rows and columns of a digital image are unique brightness or gray values. In active sensing, the traditional presentation of echo signals after processing results in an image are the intensity values, by which a measured radar cross section is generated as a gray tone (Buiten and Clevers, 1993).

For both sensing, a digital image is composed of a finite number of elements, each of which has a particular location and value. These elements are called picture elements, image, and pixels. Pixel is the term used most common to denote the elements of a digital image (Gonzalez and Woods, 2007). Each pixel is a number represented as 'digital number' (DN), which is about the average radiance of the pixel area and contains values between 0 and 255 for 8 bit optical images (Figure 2.1).
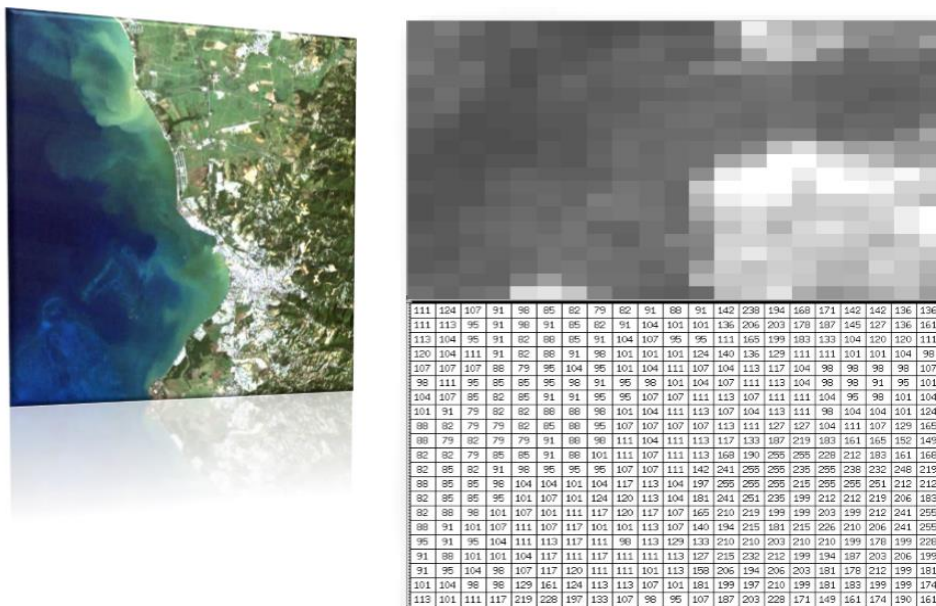
Figure 2.1 : Digital image (Campell, 2007).

2.2 Image Resolution

Image resolution can be explained as the ability of an imaging system to record and extract details in a distinguishable manner (NRC, 2014). There are four types of resolution categories in remote sensing. These are spatial, spectral, radiometric and temporal resolutions.

Spatial resolution is relevant to the size of the smallest object that can be resolved on the ground. In other words, it specifies the size of the pixel of the image acquired by remote sensing techniques. However, the resolution in a digital image is sometimes restricted by the pixel size. Spatial resolution is based on many factors, such as the field of view, altitude of the sensor, the number of detectors etc. Also, the spatial resolutions of the sensors can change with the viewing angle, and influenced by the terrain structure on the ground (Navulur, 2007). In target recognition and identification, spatial resolution has taken an important role. Especially after 2000's, commercial and private satellites have been increased and they have provided images with various spatial resolutions in a wide range. Spatial resolutions can be categorized as low resolution which is defined as pixels with ground sampling distance of 30 m or greater resolution, medium resolution which has a resolution between 4 and 30 m and high resolution which has pixel sizes 4 m or smaller pixel sizes.

Radiometric Resolution is the sensitivity to small differences in the radiation of the observed target or object (Campbell, 2007). In other words, it refers to the number of gray levels available for image analysis. The value range can be computed using equation below:

$N = 2^R$

where N is the range and R is the radiometric depth. For instance, when a sensor use 8 bits to record the data, there will be $2^8 = 256$ digital numbers which are ranging from 0 to 255.

Spectral resolution refers to the number of bands in the electromagnetic spectrum where the instrument can take measurements. In other words, it is an ability of a sensor regarding to the wavelength intervals. The narrower the wavelength range for a special channel or band, the finer the spectral resolution is. Moreover, the spectral resolution increases by the number of bands.

In remote sensing, related to the number of bands, there have been some basic terms such as multispectral and hyperspectral to categorize the sensors. While multispectral sensors usually have less than ten bands, hyperspectral sensors generally have bands in hundreds (Navulur, 2007). An illustration of a hyperspectral image cube has been shown in Figure 2.2. The hyperspectral image generally includes over a hundred contiguous spectral bands, forming a 3D image cube which covers one spectral dimension and two spatial dimensions. Every pixel is associated with a complete spectrum of of the imaged area. Hyperspectral images have provided detailed identificaiton of the land covers (CRISP, 2014).
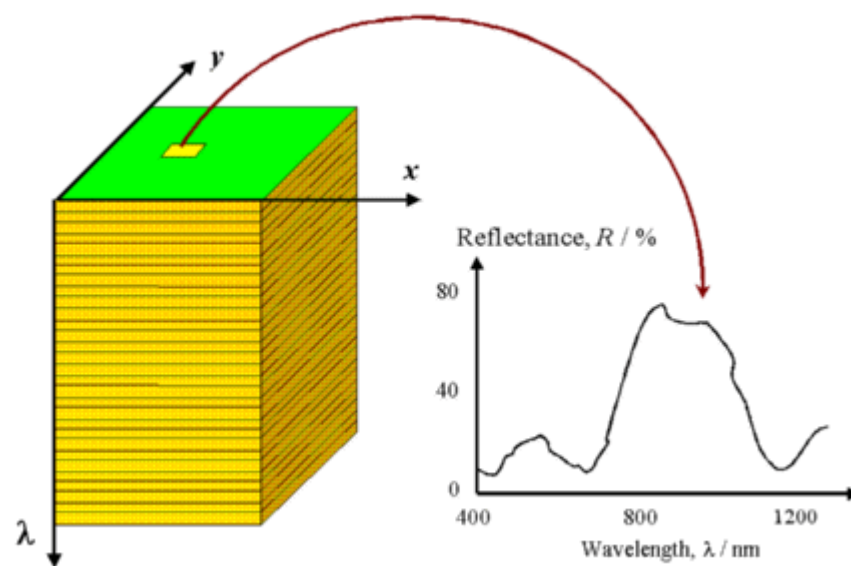
Figure 2.2 : Hyperspectral image cube (CRISP, 2014).

Especially hyperspectral sensors have detected hundreds of very narrow spectral bands around the visible, NIR and mid-IR regions of the electromagnetic spectrum. The images obtained by these sensors have been used for various target detection applications (Manolakis et al., 2003).

Temporal resolution refers to precision of a measurement related to time. Temporal resolution represents the time frequency with which the system can obtain an image of the same region of interest on the Earth. Also, the revisit capability depends on some parameters like the instrument's field of view, satellite orbit and the platform movement etc. (Campell, 2007). Different satellites have generally different revisit time. For instance, while Landsat TM has revisited same area in 16 days, IKONOS has

revisited between 3 and 5 days with off-nadir angle. Especially in disaster monitoring and management applications, temporal resolution has taken an important role.

2.3 Image Processing

Digital image processing is relevant to a detailed processing procedure of digital images by way of a digital computer (Gonzalez and Woods, 2007). There have been many digital image processing and analysis techniques to assist the interpretation of digital images and to extract as much information as possible from the images. The particular techniques can be chosen with respect to aim of individual project. The processing procedures can be classified in three broad categories: 'Image Preprocessing', 'Image Enhancement', and 'Information Extraction and Image Interpretation' (Bernstein and Ferneyhough, 1975).

2.3.1 Image preprocessing

Image preprocessing is also known image restoration and rectification. In this basic step, DN values are recalculated for the digital image. Preprocessing, which is initial processing on the raw data, is applied to correct for any distortion caused by the characteristics of the imaging system and conditions. These distortions could be data errors, noise, atmospheric effects, sun illumination geometry and geometric distortions introduced during the scanning, recording, and playback processes. Specific correction methods have been applied to minimize these problems in image restoration or preprocessing.

Radiometric and geometric corrections have been applied as most common preprocessing procedures in digital image processing. Radiometric correction is used to correct for uneven sensor response over the entire image and geometric correction is used to correct for geometric distortion caused by Earth's rotation and other imaging conditions like oblique viewing. Also, the image could also be transformed to conform to a suitable map projection system (Pons et al., 2014).

In order to have a better geometrically corrected image, image resampling procedures have been applied to digital images. Image resampling is a basic process by which new pixel values are interpolated from existing pixel values and this procedure has been applied whenever the raster's structure is changed such as during datum and

projection transformations, and cell resizing operations (Wade and Sommer, 2006). There are three main resampling algorithms: Nearest Neighbor, Bilinear Interpolation and Cubic Convolution which are all commonly used in image editing softwares (Studley and Weber, 2011). Each resampling method has strengths and weaknesses and they must be considered carefully with respect to aim of the application.

Nearest Neighbor (NN) resampling is very frequently used in remote sensing and it functions by matching a pixel from the original image to its corresponding position in the resized image. When there is no corresponding pixel is available, the pixel nearest is used instead (Figure 2.3). This method works well with horizontal or vertical lines (Goldsmith, 2014), however, it introduces outstanding error along other linear features in which pixel rearrangement into lines is obvious (eXtension, 2014) and for that reason is usually known the least accurate method. NN is widely used due to the speed of implementation and simplicity (Dodgson, 1992). Recently, computers have become more powerful and it is easy to decline a less computationally intensive process for one with more accurate results. However, some remotely sensed images computation time can still a concern if the images are very large (>1 GB). Also, it is noted that NN is a unique resampling process in that it is the only method that does not interpolate new values into the dataset, and is therefore the only method that should be used for categorical data (ESRI, 2009; Verbyla, 2002). In this method, there is only one value (orange dot) used to generate the new output value, which is derived from the cell nearest the target (Figure 2.3).

Bilinear interpolation has used the arithmetic mean of the four pixels nearest the concerning cell to calculate a new pixel value (Figure 2.3). This resampling method is an image smoothing method and when the image is displayed larger or smaller than it actually is (Goldsmith, 2014). Also, this method retains better positional accuracy than nearest neighbor resampling (Verbyla, 2002), however it could introduce new values never found in the original image with some blurred edges introduced as well (Goldsmith, 2014).

Cubic convolution (CC) is a method used to determine the gray levels in an image through a weighted average of the 16 closest pixels to the input coordinates (Figure 2.3). This method produces the smoothest and most continuous image compared to the other two methods (Huber, 2014). However, CC resampling takes longer time

longer (about 10 times) to process the computation than nearest neighbor (eXtension, 2014; Huber, 2014).
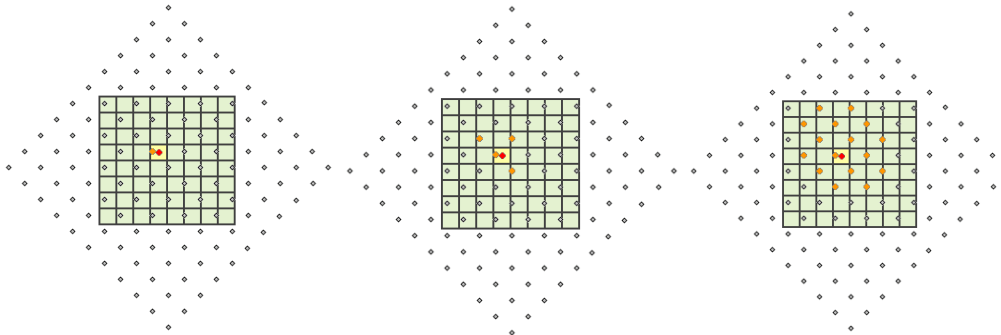
Figure 2.3 : Nearest Neighbor resampling (left), Bilinear interpolation (mid) and Cubic Convolution (right). The gray dots represent the centers of the input raster cells and the green grid represents the output raster. The target cell is yellow with the red dot showing the center. *Note: Figure obtained from ESRI.*

2.3.2 Image enhancement

Image enhancement is done to make it easier for visual interpretation and understanding of digital images. It also applied images to alter its impact on the viewer. After preprocessing procedures are completed on the raw data, image enhancement operations can be applied. There have been specific techniques such as grey level stretching to improve the contrast and spatial filtering for enhancing the edges. Moreover, contrast stretching, density slicing, principal components analysis and rationing are other basic tools that provide better scene quality and can be categorized as an image enhancement methods for digital images (Balaselvakumar and Saravanan, 2006).

2.3.3 Information extraction and image interpretation

Image preprocessing and enhancement procedures generally utilize computers to provide corrected and improved images for applications by human interpreters. In these two steps, the computer systems can not make decisions about the images. Nevertheless, processes which identify and extract information do utilize the computer's decision-making capability to identify and extract specific parts of information. In this procedure, a human operator must manage the computer and must evaluate the significance of the extracted information (Sabins, 1987).

The aim of feature extraction is to obtain the most relevant information from the original data. There are various methods used as information extraction methods. One of them is image transformations like principal components analysis, which are mathematical techniques that use statistical methods to decorrelate data and reduce redundancy. Also, some arithmetic operations such as rationing are image manipulation techniques, to highlight certain features. Moreover, there have been other methods such as change detection, pattern recognition and classification which are used commonly as image extraction methods in remote sensing (Berni et al., 2009). Classification is the most used traditional method to generate LCLU maps in remote sensing applications. Digital classification is the process of sorting pixels into a finite number of individual classes, or categories, of data based on their brightness values (Al-Bakri et al., 2013). There are two types image classification techniques: Unsupervised and supervised classification.

In unsupervised classification, the processing program automatically groups the pixels in the image into separate clusters, depending on their spectral features. Each cluster will then be assigned a land cover type by the analyst. In other words, unsupervised classification is the process of grouping multispectral images and assigning colors which represent either clusters of statistically different sets in correlation with separable classes. The unsupervised classification image classification technique is commonly used when no sample sites exist. In this technique, after the user determines the number of clusters to generate and which bands to use, the image classification software generates clusters. There have been different image clustering algorithms such as K-means and ISODATA (Iterative Self-Organizing Data Analysis Technique). ISODATA algorithm has provided grouping of pixels with similar spectral characteristics by deriving statistics (mean and standard deviation) of groups and assigning a class to each pixel according to its distance from mean (Al-Tamimi and Al-Bakri, 2005). The ISODATA algorithm is similar to the K-means algorithm with the distinct difference that the ISODATA algorithm enables for different number of clusters while the k-means assumes that the number of clusters is known a priori. (Yale, 2014).

Supervised classification is based on that a user can select and decide sample pixels in an image which are representative of decided classes and then direct the image processing software to use these training sites as references for the classification of all

other pixels in the image (Figure 2.4). Training sites, which are selected based on the knowledge of the user, have been recorded as a spectral signature file. Each pixel was then assigned to the most likely class based on the maximum likelihood algorithm, the most commonly used classification algorithm. Maximum likelihood algorithm has uses the statistics of the training sets and the pixels are assigned to the class with the highest probability. In this classification method, the user also determines the number of classes that the image is classified into. Although this algorithm is slower than the the other classifiers, it theoretically offers the best classification technique (Jensen, 1996; Schowengerdt, 1997).
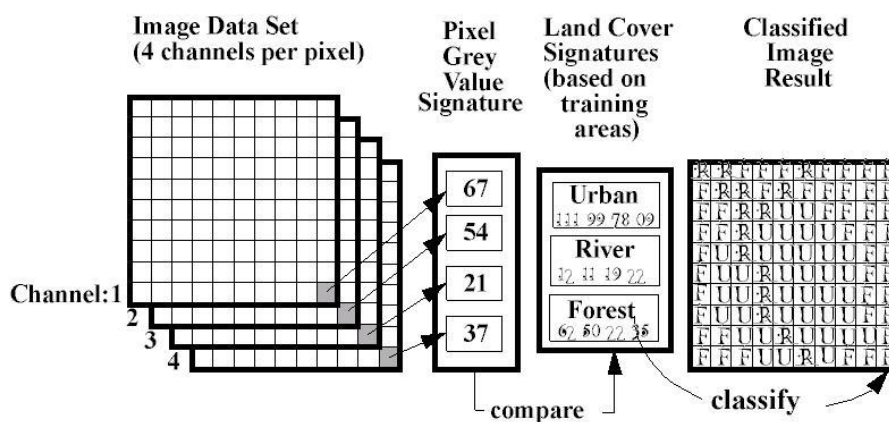
Figure 2.4 : Steps in supervised classification (Url-1).

After information has been extracted from previous procedures, it can be used as an input to other information systems. Remote sensing products are used with generally integrated into a Geographical Information System. GIS is known that a data-handling technology, while remote sensing is a data retrieval and analysis technology. GIS integrates data for capturing, managing, analyzing, and displaying all forms of geographical. GIS allows to view, understand, interpret, and visualize data in many ways that reveal relationships in the form of maps and reports. In this respect, remote sensing provides a very important source of spatial data for GIS. Integration of remote sensing and GIS technologies significantly promote the ability to handle geo-information (Balaselvakumar and Saravanan, 2006 ; Weng, 2009).

3. REMOTE SENSING SATELLITE SYSTEMS

In spaceborne remote sensing, sensors are mounted on-board a space shuttle or satellite orbiting the earth. There have been many remote sensing satellites which provide images for research and operational applications. The satellite technology was initially used for military purposes and then it has improved rapidly in various fields. As spaceborne remote sensing provides synoptic view, wide area coverage is possible. Spaceborne remote sensing also provides frequent and repetitive coverage ability of a region of interest. In general, satellite image has a lower spatial resolution compared to aerial photography. However, very high resolution images (up to 30 cm resolution from WorldView-3) are now commercially available to civilian users and they have been used in many applications (CRISP, 2014).

3.1 Satellite Orbits

Satellites move in a path around the Earth named an orbit. All satellites must have an orbital path and the kind of path it takes is determined by the physics included. A satellite's orbit works due to a balance between two main forces. The orbit is a combination of the satellite's speed and the force of the Earth's gravitational pull on the satellite. That gravitational pull is the related to the mass of the Earth and satellite. It is known that gravity keeps the satellite's velocity from sending the satellite flying out in a straight line away from the Earth, and the satellite's speed keeps the force of gravity from pulling the satellite back to Earth.

Most satellites follow a generally elliptical orbit around the earth. The time taken to complete one revolution of the orbit is named the orbital period. Generally, Remote sensing satellites are launched into special orbits such that the satellite repeats its path after a fixed time interval. This time interval is named the repeat cycle of the satellite. There have been three types of orbits which are geostationary, near polar and sun synchronous (Rutgers, 2015).

The satellites which have used geostationary orbits stay right over the same spot all the time and this stationary has been above a specific point on the Earth (Figure 3.1). Geostationary orbits allow the satellites to observe almost a full hemisphere of the Earth and these satellites generally are used to study large scale phenomenon. These orbits are ideal for weather satellites and communications satellites. These orbits are commonly used for weather monitoring since satellites in this orbit provide a constant view of the same area. Geostationary satellites such as the Geostationary Operational Environmental Satellite (GOES) satellites send information about clouds, water vapor, and wind. After, this near constant stream of information serves as the basis for most weather monitoring and forecasting (NASA, 2015). However, there have been some disadvantages of this type of orbit. As these satellites are very far away, they have low spatial resolution. The other disadvantage is that these satellites sometimes have trouble monitoring activities near the poles (Rutgers, 2015).
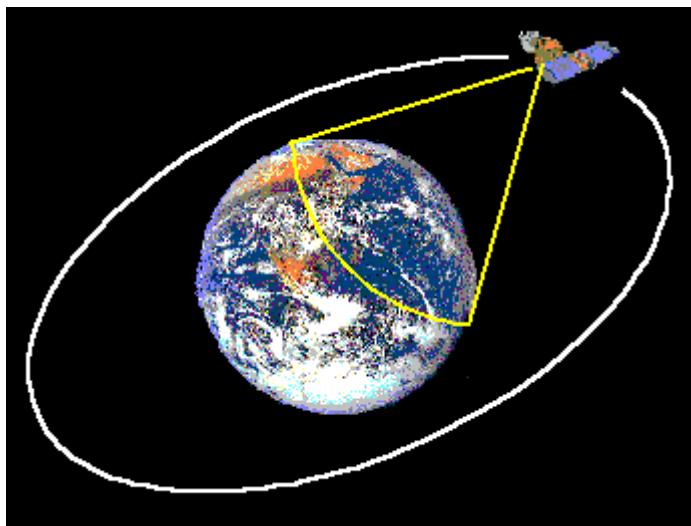
Figure 3.1 : Geostationary orbit (CRISP, 2014).

A near polar orbit is one with the orbital plane inclined at a small angle in respect of the earth's rotation axis (Figure 3.2). A satellite using near polar orbit passes close to the poles and is able to include almost the whole earth surface in a repeat cycle. It takes about 90 minutes for the satellite to complete one orbit. These satellites have many uses like measuring ozone concentrations in the stratosphere and also measuring temperatures in the atmosphere.
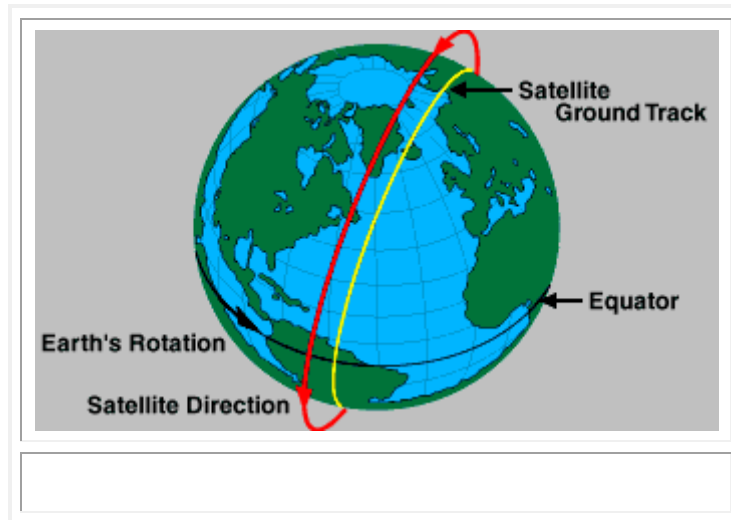
Figure 3.2 : Near polar orbit (CRISP, 2014)

Sun synchronous orbits allow a satellite to pass over a location at a given latitude at the same local solar time (Figure 3.3). The satellites which use sun synchronous orbits have to shift their orbits about one degree per day and they orbit at an altitude between 700 to 800 km. These orbits are generally used for satellites that need a constant amount of sunlight. Earth observation satellites usually follow the sun synchronous orbits (Rutgers, 2015).

Figure 3.3 : Sun synchronous orbits (Rutgers, 2015).

3.2 Earth Observation Satellite System

Earth mapping is one of the basic use of Earth-orbiting satellites. Generally, civilian satellites in the Landsat and SPOT series have provided Earth images which have been applied for a wide spectrum of applications in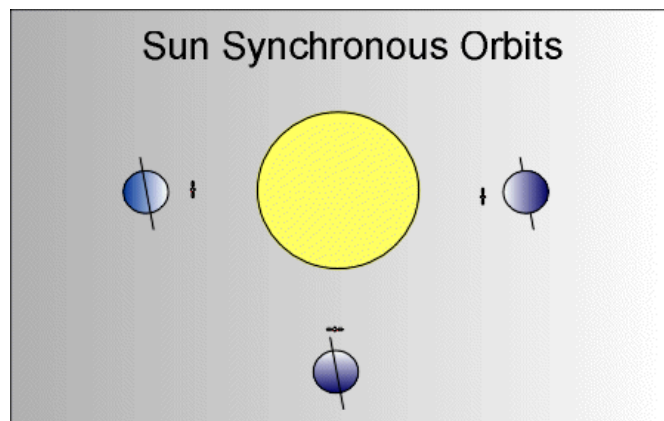 forestry, agriculture, hydrology, urban planning and geology. Satellite remote sensing systems are also a critical key in strategic and tactical planning for the countries in the defence sector. Military missions have required some important characteristics such as very high spatial resolution and orbital agility (Fouquet and Ward, 1998). Normally, all satellite-sensor platforms are characterised by the wavelength bands employed in image obtainment, spatial resolution of the sensor, the coverage area and the temporal resolution. In relation to the spatial resolution, the satellite imaging systems usually can be classified into:

- Low resolution systems (about 1 km or more)

- Medium resolution systems (about 100 m to 1 km)

- High resolution systems (about 5 m to 100 m)

- Very high resolution systems (about. 5 m or less)

Concerning the spectral regions used in data acquisition, the satellite imaging systems can be classified as:

- Optical imaging systems (cover visible, NIR, and SWIR systems)
- Thermal imaging systems
- Synthetic aperture radar (SAR) imaging systems

Optical/thermal imaging systems can be categorized according to the number of spectral bands used: Monospectral or panchromatic systems, multispectral systems, superspectral (tens of spectral bands) systems and hyperspectral systems which consist of hundreds of spectral bands. SAR imaging systems can be classified related to the combination of frequency bands and polarization modes used in data obtainment, e.g.: (CRISP, 2014).

- Single frequency (L-band, or C-band, or X-band)
- Multiple frequency (Combination of two or more frequency bands)
- Single polarization (VV, or HH, or HV)
- Multiple polarization (Combination of two or more polarization modes)

3.2.1 LANDSAT Earth observation satellites

3.2.1.1 History

Landsat satellites have collected images of the Earth's surface for more than thirty years. Instruments onboard the satellites have obtained millions of images of the Earth. These images have provided a valid resource for researchers who work in forestry, urban and regional planning, agriculture, geology, and global change research. The program was first started by The National Aeronautics and Space Administration (NASA) in 1972, then turned over to the National Oceanic and Atmospheric Administration (NOAA) after it became operational (CRISP, 2014). The first three Landsat satellites were launched in 1972, 1975 and 1978 respectively (Figure 3.4). These satellites were primarily designed to acquire detailed information about the Earth's natural resources, covering the condition of forests and farming areas. Also, they were supplied to monitor atmospheric and oceanic conditions and to disclose variations in pollution degree and other ecological changes. These three satellites had different types of cameras, involving those with infrared sensors. Landsat cameras provided images of interest areas (184 km) square; each such area could be acquired at 18-day intervals (USGS, 2014).

The fourth and fifth Landsat satellites were launched in 1982 in 1984 respectively. In 1985, Landsat was transferred to a private commercial company, the Earth Observation Satellite Company (EOSAT) and in 1992 the U.S. government again took control of the program. In these newer models, there were two sensors like a multispectral scanner and a thematic mapper, which provides 30 m spatial resolution in its spectral bands. Landsat 6 failed to achieve orbit after its launch in 1993. In 1999, Landsat 7 was launched successfully. As Landsat 5 and 7 were nearing the end of their operational lifetimes, a new satellite, the Landsat Data Continuity Mission, was planned for launch in 2012. The most recent, Landsat 8, was eventually launched on February 11, 2013 (USGS, 2015).
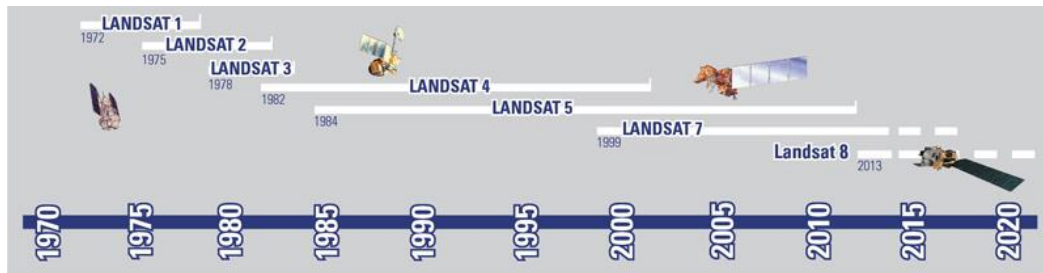
Figure 3.4 : LANDSAT missions timeline.

3.2.1.2 Orbit and scanning system

The Landsat 7 and Landsat 8 satellites, which have still been used, have a near-polar, sun-synchronous orbit, following the World Reference System (WRS-2). They obtain images between 81^0 N and 81^0 S. They make an orbit in approximately 99 minutes, complete over 14 orbits per day, and enable complete coverage of the Earth every 16 days. However, there have been 8 days offset between the two satellites. The descending node from north to south passses the equator between 10:00 am and 10:15 am as local time (USGS, 2014).

There have been used different scanning systems in Landsat satellite series. Multispectral scanner (MSS) was used on Landsat-1 to 5. It had 4 spectral bands which change between 0.5 and 1.1 microns. Although it was one of the older generation sensors, data obtainment for MSS was completed in late 1992. The resolution of this sensor was about 80 m with radiometric coverage in four spectral bands. Table 3.1 shows some spectral and spatial characteristics of MSS sensor (NASA, 2015).

Table 3.1 : Landsat MSS characteristics.

Landsat 1-2-3 Bands	Landsat 4-5 Bands	Spectral Range (Microns)	Electromagnetic Region	Swath width
4	1	0.5 - 0.6	Green (Visible)	185x185 km
5	2	0.6 - 0.7	Red (Visible)	185x185 km
6	3	0.7 - 0.8	NIR	185x185 km
7	4	0.8 - 1.1	NIR	185x185 km

The Thematic Mapper (TM) is a developed sensor designed to obtain higher image resolution, sharper spectral separation, improved geometric fidelity and better

radiometric accuracy and resolution than the MSS sensor. They was first introduced with Landsat-4 in 1982. They have seven spectral bands simultaneously. As band 6 senses thermal infrared radiation (TIR), Landsat can obtain night scenes using band 6. TM scenes have 30m spatial resolution in bands 1-5 and 7 while band 6 has an 120 m spatial resolution (Table 3.2). When they are compared to MSS, bands of TM are more sensitive to observe spectral variations (NASA, 2015).

Table 3.2 : Landsat TM characteristics.

Band	Band Name	Spectral Range (Microns)	Spatial Resolution(m)	Swath width	Temporal Resolution
1	Blue (Visible)	0.45 - 0.52	30	185x185 km	16 days
2	Green (Visible)	0.52 - 0.60	30	185x185 km	16 days
3	Red (Visible)	0.63 - 0.69	30	185x185 km	16 days
4	NIR	0.76 - 0.90	30	185x185 km	16 days
5	SWIR-1	1.55 - 1.75	30	185x185 km	16 days
6	TIR	10.04 - 12.5	120	185x185 km	16 days
7	SWIR-2	2.08 - 2.35	30	185x185 km	16 days

ETM+ (Enhanced Thematic Mapper Plus) scanning system was made for Landsat-7 in 1999. The ETM+ instrument has an eight band multispectral scanning radiometer which is capable of providing high resolution image information about target surface. Spectral bands are similar to those of TM, except that the thermal band (band 6) has a higher resolution of 60 m (120 m in TM). There has been also an additional panchromatic band at 15 m spatial resolution (Table 3.3), (USGS, 2014).

Table 3.3 : Landsat ETM characteristics.

Band	Band Name	Spectral Range (Microns)	Spatial Resolution(m)	Swath (km)	Temporal Resolution
1	Blue (Visible)	0.45 - 0.515	30	183	16 days
2	Green (Visible)	0.525 - 0.605	30	183	16 days
3	Red (Visible)	0.63 - 0.69	30	183	16 days
4	NIR	0.75 - 0.90	30	183	16 days
5	SWIR-1	1.55 - 1.75	30	183	16 days
6	TIR	10.04 - 12.5	60	183	16 days
7	SWIR-2	2.09 - 2.35	30	183	16 days
8	PAN	0.52 - 0.90	15	183	16 days

The Operational Land Imager (OLI), which is a scanning system used in Landsat 8, measures in the visible, nir, and swir portions of the spectrum. It provides images which have 15 m panchromatic and 30 m multispectral spatial resolutions along a 185 km wide swath. OLI has used long detector arrays, with more than 7,000 detectors per spectral band, aligned across its focal plane to view along the swath. This is known as 'push-broom' design cause to a more sensitive instrument having improved land cover information with less moving parts. With the improved signal-to-noise ratio compared to previous Landsat instruments, it has been expected from this new OLI design to be more reliable and to provide better performance. Apart from the other scanning systems, it has coastal/aerosol band for water quality applications and cirrus band for cloud detection (NASA, 2015). TIR sensor which has been as second sensor in Landsat 8 has also two bands with respect to quantum physics applications (NASA, 2015). Both OLI and TIR system specifications have been given in Table 3.4.

Table 3.4 : Landsat 8 characteristics.

Band	Band Name	Spectral Range (Microns)	Spatial Resolution(m)	Swath (km)	Temporal Resolution
1	Coastal/Aerosol	0.433 - 0.453	30	185	16 days
2	Blue (Visible)	0.450 - 0.515	30	185	16 days
3	Green (Visible)	0.525 - 0.600	30	185	16 days
4	Red (Visible)	0.630 - 0.680	30	185	16 days
5	NIR	0.845 - 0.885	30	185	16 days
6	SWIR-1	1.560 - 1.660	30	185	16 days
7	SWIR-2	2.100 - 2.300	30	185	16 days
8	PAN	0.500 - 0.680	15	185	16 days
9	Cirrus	1.360 - 1.390	30	185	16 days
10	TIR-1	10.60 - 11.20	100	185	16 days
11	TIR-2	11.50 - 12.50	100	185	16 days

3.2.2 Defense meteorological satellite program

The Defense Meteorological Satellite Program (DMSP) satellites have observed environmental features like clouds, bodies of water, snow, fire and pollution, and they have recorded information (Kramer, 1994). DMSP is also used in planning and managing U.S. military operations worldwide. NOAA, the Navy and the Air Force have shared responsibility for processing the data from NOAA and DMSP satellites (U.S. Congress, 1994). Moreover, some of DMSP satellites have night visual sensors with a valid capability to measure low levels of visible and NIR radiance at night (Figure 3.5). Therefore, it is possible to detect and measure clouds illuminated by moonlight, lights from cities and motorway, fires and gas flares. The data acquired from these satellites has been used in many scientific and military applications.
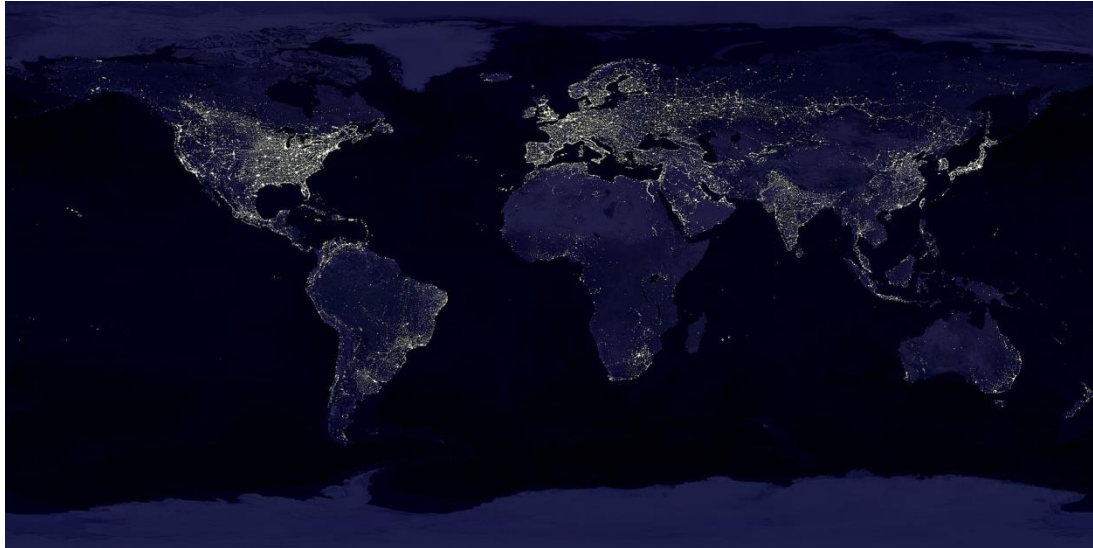
Figure 3.5 : DMSP-OLS image (Url-2).

3.2.2.1 History of DMSP

The Department of Defense started the DMSP in the mid-1960s. This program has low earth-orbiting satellites and they have provided important military and environmental information. The ground systems development and operation of the satellites has been managed by NOAA. The Defense Satellite Application Program Block-1 satellites series, also known as P-35, was the first series of military meteorological satellites of the USA. There have been many block satellite series since 1962 and the latest launch of a DMSP satellite, which is DMSP-F19, occurred on April 3, 2014, from Vandenberg aboard an Atlas V rocket (Hall, 2001).

3.2.2.2 Orbit system of DMSP

The DMSP satellites have a 101 minute, sun-synchronous near-polar orbit at an altitude of 830 km above the surface of the Earth. The visible and infrared sensors obtain images through a 3000 km swath and they also have enabled global coverage twice per day. It is possible to obtain global information such as clouds every 6 hours with combination of day-night and dawn-dusk satellites. These satellites generally involve polar regions at least twice and the equatorial region once per day (NOAA, 2014). DMSP specifications has been given Table 3.5.

Table 3.5 : DMSP technical specifications.

Orbit	Sun synchronous near polar orbit
Altitude	830 km
Revisit	101 minutes
Sensors	OLS (Operational Linescan System) SSM/I (Microwave Imager) SSM/T (Atmospheric Temperature Profiler) SSMT/2 (Atmospheric Water Vapor Profiler) SSJ/4 (Precipitating Electron & Ion Spectrometer) SSIES (Ion Scintillation Monitor)

3.2.2.3 DMSP operational linescan system

The DMSP has operated since 1970s the Operational Linescan System (OLS). The DMSP programme has been upgraded over time since declassification, and the latest series (Block-5D) include the OLS which is an oscillating scan radiometer capable of measuring the visible and thermal-infrared emissions. The DMSP satellite (Figure 3.6) has been in a sun synchronous low earth orbit, which is about 833km altitude, and makes a nighttime pass usually between 20.30 and 21.30 each night (Elvidge et al., 2001). OLS has a nominal resolution of 2.7 km and about 3000 km swath width. It has also 1 km spatial resolution data, which is resampled from the fine mode resolution which has 0.55 km resolution. This data has been distributed by National Geophysical Data Center (NGDC) of NOAA. The OLS sensor's main mission was the detection of nighttime moonlit cloud cover for regional and global meteorological forecasting for the Air Force. For this purpose, the visible spectral band (VIS) signal, which covers the visible near infrared region of the spectrum (VNIR), is intensified at night with a photomultiplier tube. This has made the sensor four orders of magnitude more sensitive and it provides to detect faint VNIR emission sources (Elvidge et al., 1997). When sunlight is eliminated, the light intensification cause to a valid data set where city lights, lightning illuminated clouds and fires can be observed. The OLS specifications has been given Table 3.6 (Yagi et al., 2010).

Table 3.6 : OLS technical specifications.

Band Name	Spectral Range (Microns)	Spatial Resolution(km) (fine - smooth)	Swath width	Radiometric Resolution
Visible (day)	0.40 - 1.10	0.55 - 2.7	3000 km	6 bit
VNIR (night)	0.47 - 0.95	0.55 - 2.7	3000 km	6 bit
Thermal-IR	10.0 - 13.4	0.55 - 2.7	3000 km	8 bit

Figure 3.6 : Conception of the DMSP Block 5-2 satellites, which covers DSMP-8, DSMP-9, DSMP-10, DSMP-11, DSMP-12, DSMP-13, and DSMP-14 (NASA, 2015).

A   pixel value is represented digital number denoting the average light intensity measured over the year ranging from 1-63. The OLS data has been projected to UTM/WGS84 projection system. Moreover, the pixels are resampled from the fine mode to 1 km spatial resolution (Doll, 2008).

Table 3.7 : Version 4 DMSP-OLS nighttime lights time series (Url-3).

Average Visible, Stable Lights, & Cloud Free Coverages
Year\Sat.	F10	F12	F14	F15	F16	F18
1992	F101992	-------	-------	-------	-------	-------
1993	F101993	-------	-------	-------	-------	-------
1994	F101994	F121994	-------	-------	-------	-------
1995	-------	F121995	-------	-------	-------	-------
1996	-------	F121996	-------	-------	-------	-------
1997	-------	F121997	F141997	-------	-------	-------
1998	-------	F121998	F141998	-------	-------	-------
1999	-------	F121999	F141999	-------	-------	-------
2000	-------	-------	F142000	F152000	-------	-------
2001	-------	-------	F142001	F152001	-------	-------
2002	-------	-------	F142002	F152002	-------	-------
2003	-------	-------	F142003	F152003	-------	-------
2004	-------	-------	-------	F152004	F162004	-------
2005	-------	-------	-------	F152005	F162005	-------
2006	-------	-------	-------	F152006	F162006	-------
2007	-------	-------	-------	F152007	F162007	-------
2008	-------	-------	-------	-------	F162008	-------
2009	-------	-------	-------	-------	F162009	-------
2010	-------	-------	-------	-------	-------	F182010
2011	-------	-------	-------	-------	-------	F182011
2012	-------	-------	-------	-------	-------	F182012
2013	-------	-------	-------	-------	-------	F182013

4. SPECTRAL MIXTURE ANALYSIS

Especially low resolution images involve mixed pixels which are covered with more than one land use classes. This restriction can be overcome using subpixel classification procedures (Tompkins et al., 1997). Spectral unmixing approaches are the most widely used methods for extracting information from mixed pixels (Lu et al., 2003). These approaches have been used for providing information to monitor different natural resources such as agricultural, forest, geological and environmental problems like rapid urbanization, deforestation, plagues and disease, forest fires (Quintano et al., 2012). Spectral mixture analysis (SMA) was first developed to analyse High Spectral Resolution Advanced Visible/Infrared Image Spectrometer (HSR AVIRIS) data. It was later applied to be used with Landsat and other data (Lunetta, 1998). Before the spectral mixture model is applied, the calibration process must be applied to the satellite images.

4.1 Radiometric Calibration

In this part, the calibration procedure has been explained over Landsat data, which have been used widespread in remote sensing applications. It is known that the spectral radiance sensed by each Landsat detector is stored as an 8 bit digital number. These DN values should be converted to radiance (units: $\text{W m}^{-2} \text{ sr}^{-1} \text{ μm}^{-1}$), to reduce changes in the instrument radiometric calibration, and then converted to top of atmosphere (ToA) reflectance to decrease remote sensing variations caused by changes in the sun–earth distance, the solar geometry, and exoatmospheric solar irradiance arising from spectral band differences (Figure 4.1). In other words, the aim of ToA reflectance, which is also called as exoatmospheric reflectance, is to find surface reflactance at the satellite (SERDP, 2012). Also, the radiometric parameters and sun angle values are required to calibrate radiometrically for satellite differences (Singh, 1985; Teillet, 1986; Moran et al., 1992). This is especially important for applications that use Landsat data acquired over large areas and long time periods. The conversion of the radiance values sensed at the Landsat reflective and thermal wavelengths to reflectance, which is unitless, and brightness temperature as kelvin respectively enables data that has

physical meaning. For instance, It can be also compared with laboratory and fieldwork measurements, model results, data acquired by other satellite sensors , and importantly enables data that can be used to obtain geophysical and biophysical products (Masek et al., 2006; Justice et al., 2002).
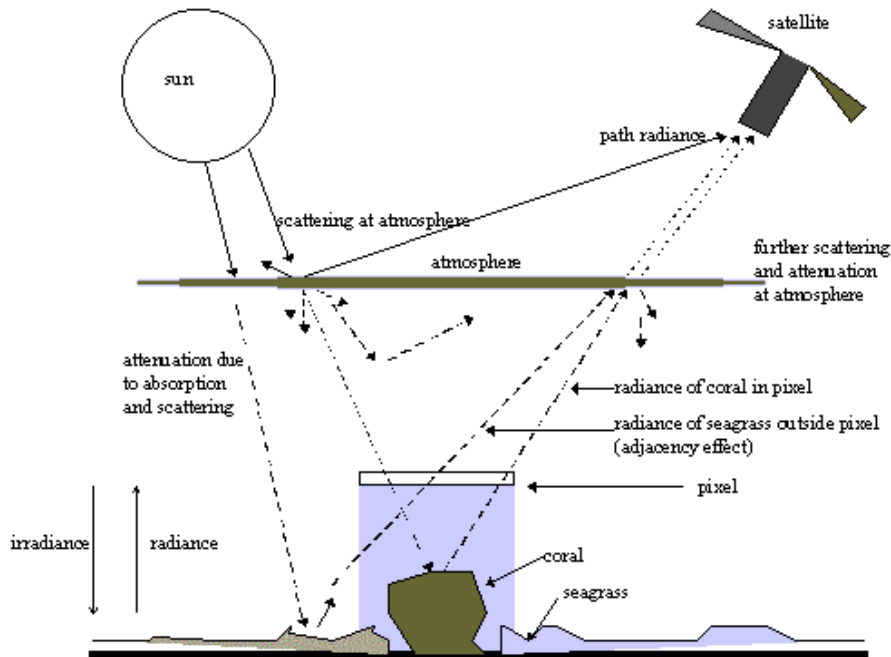
Figure 4.1 : Atmospheric interference (Url-4).

For all bands of the satellite image, 8 bit digital numbers are converted to spectral radiance using sensor calibration gain and bias coefficients obtained from the Landsat file metadata. The radiance sensed in the Landsat reflective wavelength bands the blue, green, red, near-infrared, and the two mid-infrared bands, are converted to ToA reflectance using the standard formula as:

$$\rho = \frac{\pi . L . d^2}{ESUN . cos(SZ)}$$

ρ= top of atmosphere (TOA) reflectance (unitless), (0-1)

π= 3.141593

L = the TOA spectral radiance (W m− 2 sr− 1 μm− 1)

d = the Earth–Sun distance in astronomical units

ESUN = the mean TOA solar spectral irradiance (W m− 2 μm− 1)

SZ = solar zenith angle

The quantities *ESUN* and *d* are tabulated and *sz* is calculated from the solar elevation angle stored in the Landsat L1T file metadata (Table 4.1), (NASA, 2015). The TOA reflectance computed as 1 is the TOA bi-directional reflectance factor and can be greater than 1, for example, because of specular reflectance over snow or water under certain solar and viewing geometries (YCEO, 2010).

Table 4.1 : Earth-Sun distance in astronomical units.

Day of Year	Distance	Day of Year	Distance	Day of Year	Distance	Day of Year	Distance	Day of Year	Distance
1	.98331	74	.99446	152	1.01403	227	1.01281	305	.99253
15	.98365	91	.99926	166	1.01577	242	1.00969	319	.98916
32	.98536	106	1.00353	182	1.01667	258	1.00566	335	.98608
46	.98774	121	1.00756	196	1.01646	274	1.00119	349	.98426
60	.99084	135	1.01087	213	1.01497	288	.99718	365	.98333

Recently, some of digital image processing softwares convert DN values of an image to ToA reflectance values easily using its parameters in formula 4.1 Figure 4.2 shows that Envi software has calibrated images using 'MTL' metadata files of Landsat.
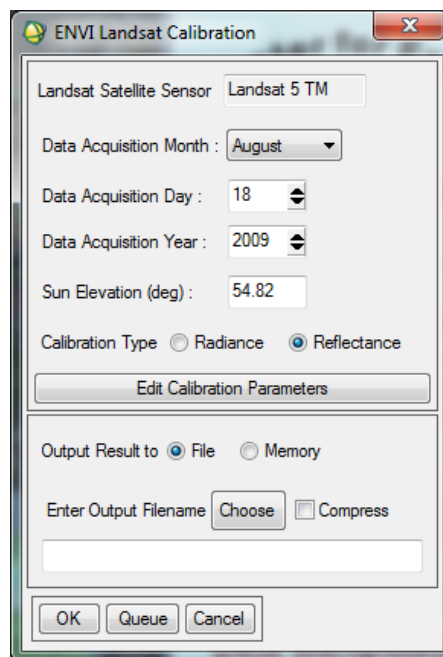
Figure 4.2 : Landsat calibration dialog.

4.2 Spectral Unmixing

After the calibration procedure has been applied to the satellite images, spectral unmixing process can be applied to the images. There have been many spectral linear and nonlinear unmixing methods which have been described recently.

4.2.1 Non-linear spectral unmixing

Non-linear mixing processes are quite difficult to perform and physical models usually do not easily provide themselves to simple mathematical solutions. The most difficult part is how to model these non-linearities when much of the required information is not available. Despite such difficulties, there have been some noticeable approaches. Hapke (1981) proposed a two-stream method which includes multiple scattering into the expression for the bidirectional reflectance technique. A multilayer perceptron (MLP) is one of the most common non-linear unmixing model which is based on neural network models for mixed pixel classification (Foody, 1996; Atkinson et al., 1997).

Non-linear methods have not been widely applied to remote sensing data because they are quite difficult to carry out. Also, the linear methods have been demonstrated in many applications to be a useful approach to analyse the variability in the data. They have provided powerful means for converting spectral information into data products with physical meaning like abundance of materials on the ground surface (Keshava and Mustard 2002).

4.2.2 Linear spectral unmixing

The spectral mixture analysis has been widely used to divide mixed pixels into its components. In other words, linear SMA is described that the spectral response of a pixel is a linear combination of all the endmembers present in the pixel. Endmembers, which can be defined as spectrally pure features, can be obtained from the image itself (called image endmembers), or measured in field conditions (Lunetta, 1998). The linear SMA has so far been the most popular technique among the SMA family (Wu and Murray, 2002).

It is known that the dimensionality of the mixing space, which is based on principal component transformations, plays a significant role when selecting accurate endmembers. A spectral mixing space can be described as a coordinate system so that

a pixel at any location can be described as a mixture of spectral endmembers. The location within the mixing space is determined by the relative abundance of spectral endmembers contributing to the mixed pixel reflectance. Linear combinations of spectral endmembers can thus be used to describe spectra that occur within a convex hull prescribed by the distribution of mixed pixels and endmembers (Boardman, 1993). To understand the topology of the mixing space, proper selection of endmembers is essential, because it determines how accurately the mixture model can represent the reflectances. The endmember collection must accommodate the dimensionality of the mixing space. The true dimensionality of the mixing space is determined by the number of spectrally different endmembers present in the target. The apparent dimensionality of the mixing space is defined by the number of spectral endmembers which can be distinguished by the sensor. The apparent dimensionality is therefore limited by the number of spectral bands available, as well as the wavelengths spanned by the bands. The limited spatial and spectral resolution of the sensor results in a projection of the true high dimensional mixing space onto a lower dimensional representation that is constrained by the ability of the sensor to discriminate different surface reflectances at GIFOV scales (Small, 2001b).

Principal component (PC) transformations have been used to quantify the dimensionality and topology of the spectral mixing space. This rotation reduces the correlations among dimensions so that the resulting PC bands (PCs) represent orthogonal components of diminishing variance. The accompanying eigenvalue distribution enables a quantitative estimate of the variance partition between the signal and noise-dominated PCs of the image. The mixing space may be represented with scatter plots of the unrotated bands. However, using scatter plots of the PCs has provided an ideal projection of the mixing space since the PC rotation orders the projections related to the variance they contribute to the scene. This explains that two or three PCs can usually provide a first order representation of the mixing space that covers the majority of image variance (Small, 2004; Price, 1997). The dimensionality of a image has determined the diversity of spectra that it involves and it is ultimately restricted by the number of spectral bands. However, noise and redundancies in the bands' information content may lead to an apparent dimensionality which is less than the full potential dimensionality implied by the number of bands. For multispectral images, eigenvalues are used as indicators of the apparent dimensionality of the image.

The eigenvalues compute how much variance is related to each rotated dimension (PC). However, they do not necessarily provide an obvious threshold to differentiate between noise and spectral information. When noise is accepted to be uncorrelated and of lower variance than the signal, the higher order PCs are expected to represent the difference between inherent dimensionality of the image and the potential dimensionality. Although higher order PCs can have low variance, they still represent spatially coherent information which is not represented by the lower order PCs. The Landsat ETM+ has enough low noise that the inherent dimensionality of spectrally diverse images is usually equal to the full six dimensions. The eigenvectors and eigenvalues of the PC transformation have given the contribution of each ETM+ band to each PC and the variance with respect to it (Small, 2004).

Figure 4.3 shows eigenvectors and eigenvalues for the PCs of the global composite dataset. Eigenvalues (left) have indicated that >90% of the variance of the global composite (circles) is related to the two primary PCs and that >98% can be defined with three low order PCs. Eigenvectors (right) have indicated that the first PC is most strongly influenced by the two SWIR bands (5,7), while the second component corresponds to VNIR band 4 with some contribution from visible red band 3. The third component has significant contributions from all six bands.

Small (2004) applied PCs to 30 subscenes of Landsat images. In Figure 4.4, gray shading has indicated scatterplot pixel density. The side view shows the two primary dimensions accounting for >90% of the variance with a triangular mixing space bounded by vegetation (V), substrate (S) and dark (D) spectral endmembers. The prominent spur extending from the low albedo endmember corresponds to reefs (R) and shallow seafloor. Figure 4.5 shows exoatmospheric or ToA reflectance vectors for the three basic endmembers related to the apexes of the primary 2D mixing space of the global composite and the corresponding local endmembers from the mixing spaces of the different subscenes. The dark surface and vegetation endmembers of the distinct subscenes are quite consistent. The high albedo substrate endmember is variable in amplitude, however, it is usually convex upward with a peak at SWIR wavelengths. The variability is related to the diversity of rock and soil reflectances represented by the substrate endmember.
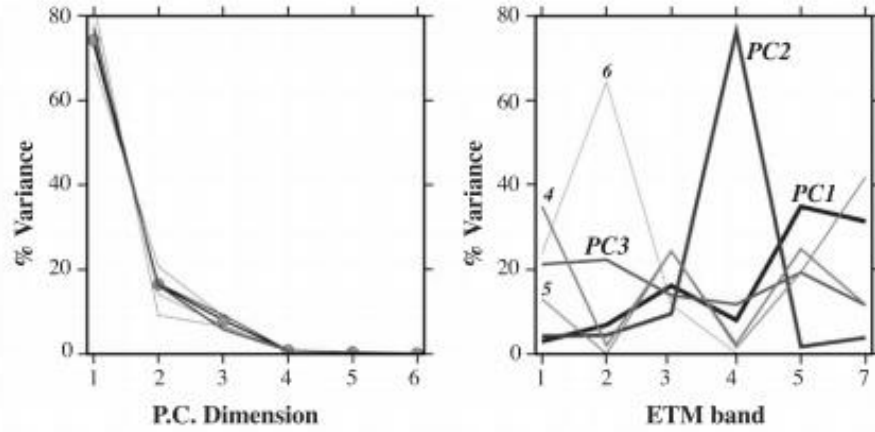
Figure 4.3 : Eigenvectors and eigenvalues for the PCs of the global composite dataset (Small, 2004).
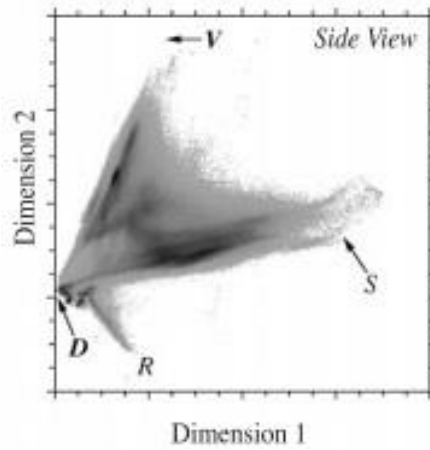
Figure 4.4 : SVD spectral endmembers (Small, 2004).
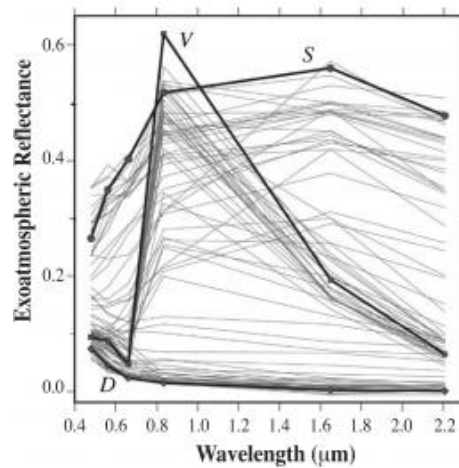
Figure 4.5 : Endmember spectra boundingthe composite and 2D mixing spaces (Small, 2004).

After endmembers are collected from scatter plots, a linear mixture model is applied to images. The consistency of the spectral mixing space for a variety of environments

suggests that a simple three component linear mixture model may provide a consistent, general characterization of land surface reflectance. The three component linear mixture model is based on SVD endmembers. Once the dimensionality of the mixing space is determined and endmembers are selected, it is straightforward to invert the linear mixture model for endmember fraction estimates. Inversion of the linear mixing model for each image pixel yields fraction estimates for each endmember. The linear three-component mixing model is given in continuous form by:

$$R(\lambda) = f_S E_S(\lambda) + f_V E_V(\lambda) + f_D E_D(\lambda)$$

where $R(\lambda)$ is the observed reflectance profile, a continuous function of wavelength λ, $E(\lambda)$ are the spectra corresponding to the (S), (V) and (D) endmembers, and the corresponding endmember fraction estimates we seek are f_S, f_V, and f_D. The discrete implementation of the model, applicable to Landsat ETM+ reflectance is given by

$$f_S e_{11} + f_V e_{12} + f_D e_{13} = r_1$$
$$f_S e_{21} + f_V e_{22} + f_D e_{23} = r_2$$
$$f_S e_{31} + f_V e_{32} + f_D e_{33} = r_3$$
$$f_S e_{41} + f_V e_{42} + f_D e_{43} = r_4$$
$$f_S e_{51} + f_V e_{52} + f_D e_{53} = r_5$$
$$f_S e_{61} + f_V e_{62} + f_D e_{63} = r_6$$

where r_i is the observed reflectance vector obtained from discrete estimates of integrated radiance within the six ETM+ bands, e_{ij} are the endmember reflectance vectors corresponding to SVD endmembers, and indices i and j indicate the spectral band and endmember of each element respectively. An additional unity sum constraint equation can be incorporated to urge the fractions to sum to 1. With six or less endmembers, the system has more equations than unknowns and can be inverted for an optimal set of endmember fraction estimates chosen to minimize misfit to the observed reflectance vector. The overdetermined linear mixing problem, incorporating measurement error, can be written in matrix notation as:

$$r = Ef + \varepsilon$$

where ε is an error vector which must be reduced to have the fraction vector f which gives the best fit to the observed reflectance vector r (Small, 2004; Settle and Drake, 1993).

5. APPLICATION

The aim of this thesis is to determine urban growth using both spectrally unmixing data and nighttime satellite data in cities selected as study area. First, potential Landsat images cover study areas have been selected and listed. These images have covered most of developed and developing cities of Turkey. Then, calendar plots were generated using Landsat filenames for main six path and row. Moreover, the calibration procedure has been applied to all Landsat data and ToA reflectance values have been obtained. After calibration process had been completed, SMA method has been applied to calibrated images. This process has been applied for three different dates which were usually selected as 1987, 1999 and 2010. SVD maps and substrate fraction maps have been generated and analysed for these years. Urban growth areas for the cities have been determined using both SMA method and nighttime satellite images.

5.1 Study Area

The study area was selected the cities developed and developing in Turkey. These cities are Istanbul, Ankara, Izmir, Bursa, Kayseri, Izmit and Manisa (Figure 5.1). As each Landsat scene is about 185 km long and 185 km wide, sometimes one scene may cover more cities and districts. For instance, Landsat scene covers Izmir covers also Manisa province in this study and these cities have been investigated together. Path and row of these cities for Landsat were determined as 180_31, 180_32, 180_33, 179_32, 177_32 and 175_33. Table 5.1 shows that population and area information for the cities (TurkStat, 2014).
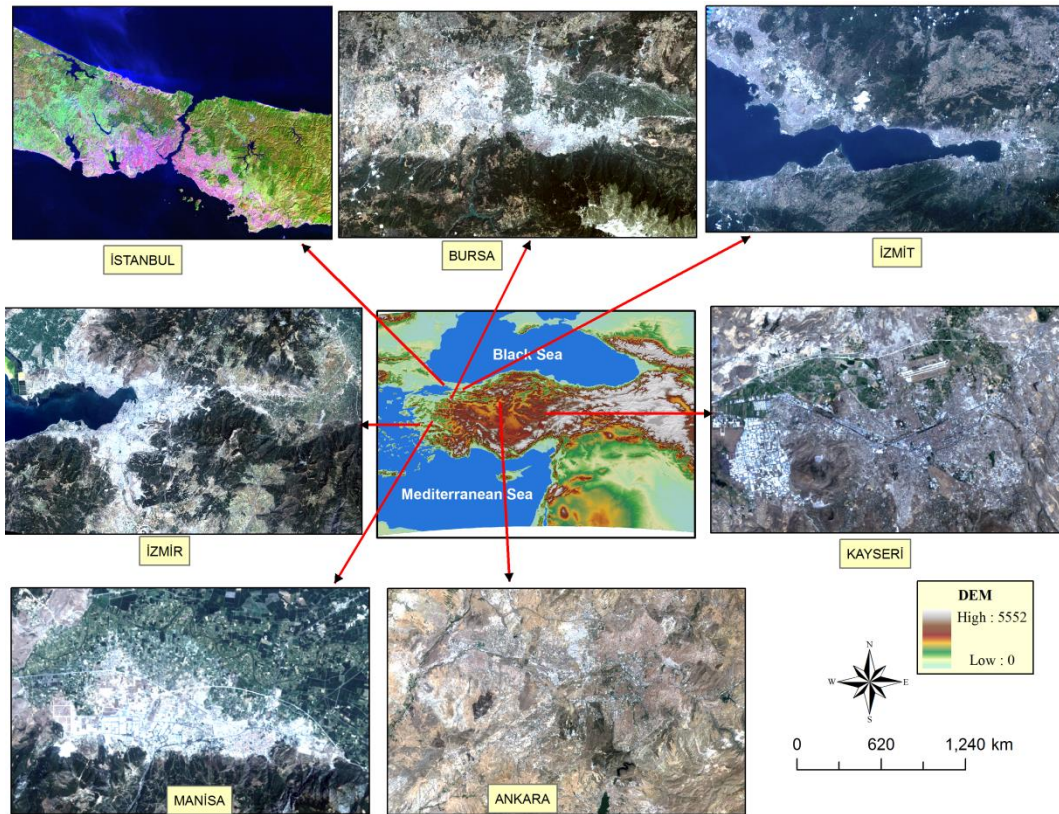
Figure 5.1 : The study area.

Table 5.1 : The census data and surface areas.

Province	Population			Surface area (km²) (2013)
	1985	2000	2010	
Ankara	3306327	4007860	4771716	25437
Bursa	1324015	2125140	2605495	10882
Istanbul	5842985	10018735	13255685	5313
Izmir	2317829	3370866	3948848	12007
Kayseri	864060	1060432	1234651	17170
Kocaeli (Izmit)	742245	1206085	1560138	3623
Manisa	1050130	1260169	1379484	13269

5.2 Datasets

After potantial study areas were determined, Landsat data archieve has been investigated using website of 'http://glovisusgs.gov/ which is managed by the United States Geological Survey (USGS, 2012). Most of Landsat data are available from 1984 to now but some of them have clouds. For this study, data have high quality without cloud have been selected. At the first step, 165 Landsat 5 (TM) and Landsat 7 (ETM) data have 180_31, 180_32, 180_33, 179_32, 177_32 and 175_33 Landsat paths and rows have been downloaded in geotiff format (Figure 5.2).
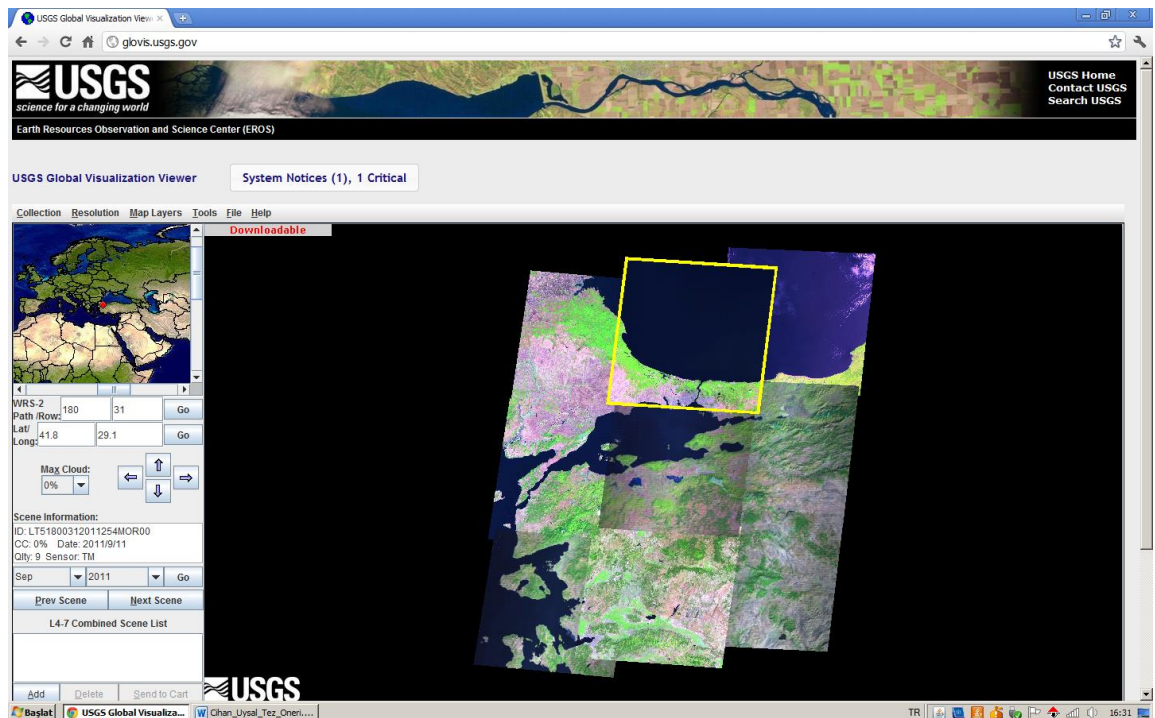
Figure 5.2 : Landsat data download.

5.2.1 Generation of calendar plots

Calendar plots were generated using Landsat filenames in unix media for six paths&rows. These plots have been used to select available and most suitable data for applications. They provide distribution of data visually and give information about acquired dates of data. Also, sensor type of Landsat data is seen apparently on these plots. The figures below, with respect to six paths and rows, demonstrate available data distribution for both Landsat 5 (TM) and 7 (ETM) images (Figures 5.3, 5.4, 5.5, 5.6, 5.7 and 5.8). While Landsat 5 (TM) images were represented with a point (•), Landsat 7 (ETM) images were represented with a star (*).

Path/Row & Cities
180_31: Istanbul
180_32: Istanbul - Bursa
179_32: Kocaeli (Izmit)
175_33: Kayseri
177_32: Ankara
180_33: Izmir-Manisa
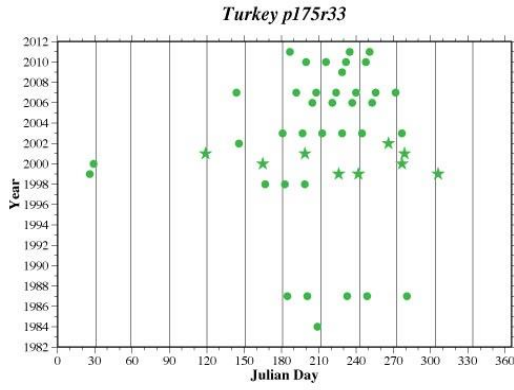
Figure 5.3 : Calendar plot of 175_33.
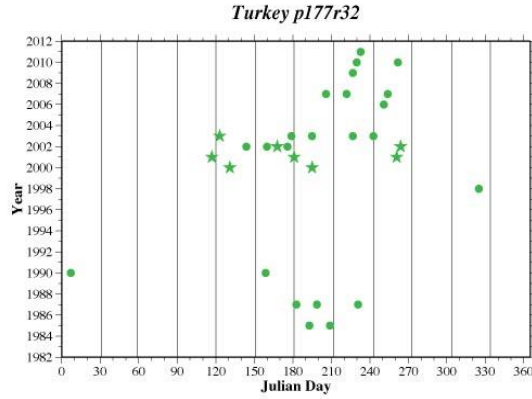
Figure 5.4 : Calendar plot of177_32.
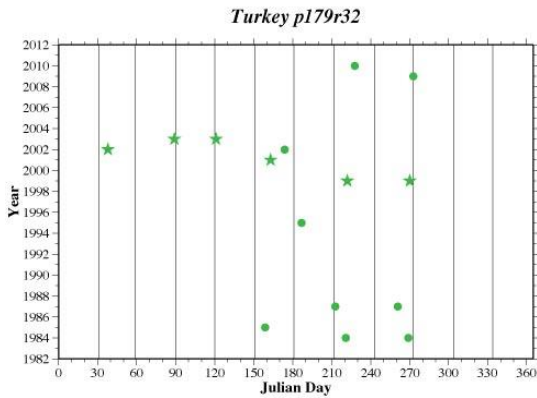
Figure 5.5 : Calendar plot of 179_32.
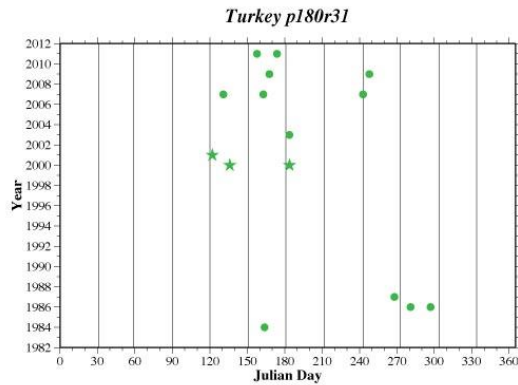
Figure 5.6 : Calendar plot of 180_31.
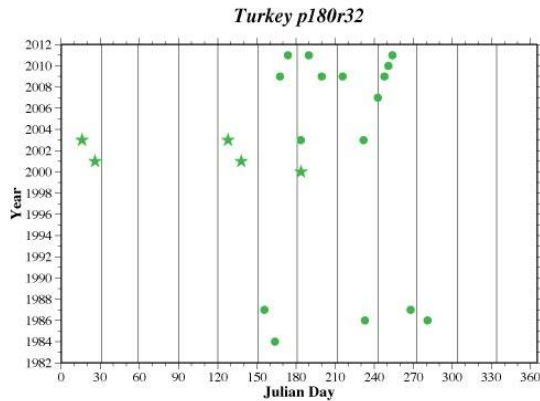
Figure 5.7 : Calendar plot of 180_32.
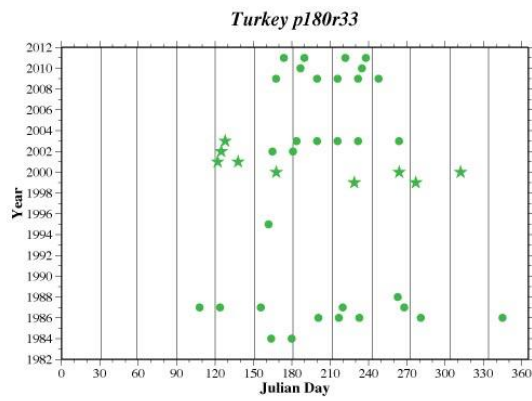
Figure 5.8 : Calendar plot of 180_33.

5.3 Preprocessing

5.3.1 Image resampling tests

Image resampling is a process used to interpolate the new cell values of a raster image during a resizing operation. There are many resampling methods available and each resampling method has strengths and weaknesses. In this study, all Landsat images have been obtained using Cubic convolution (CC). It is a method used to determine the gray levels in an image through a weighted average of the 16 closest pixels to the input coordinates.

Nearest neighbor (NN) is also a resampling method used in remote sensing. The approach assigns a value to each corrected pixel from the nearest uncorrected pixel. The advantages of nearest neighbor include simplicity and the ability to preserve original values in the unaltered scene.

To test effects of both resampling methods, a reference Landsat image, "LT51800332009618MOR" has been selected and SVD model applied to the image. When statistics of them was investigated, they had quite close results (Figure 5.9). Also, there have not been any significant differences for images used the both methods (Figures 5.10 and 5.11).
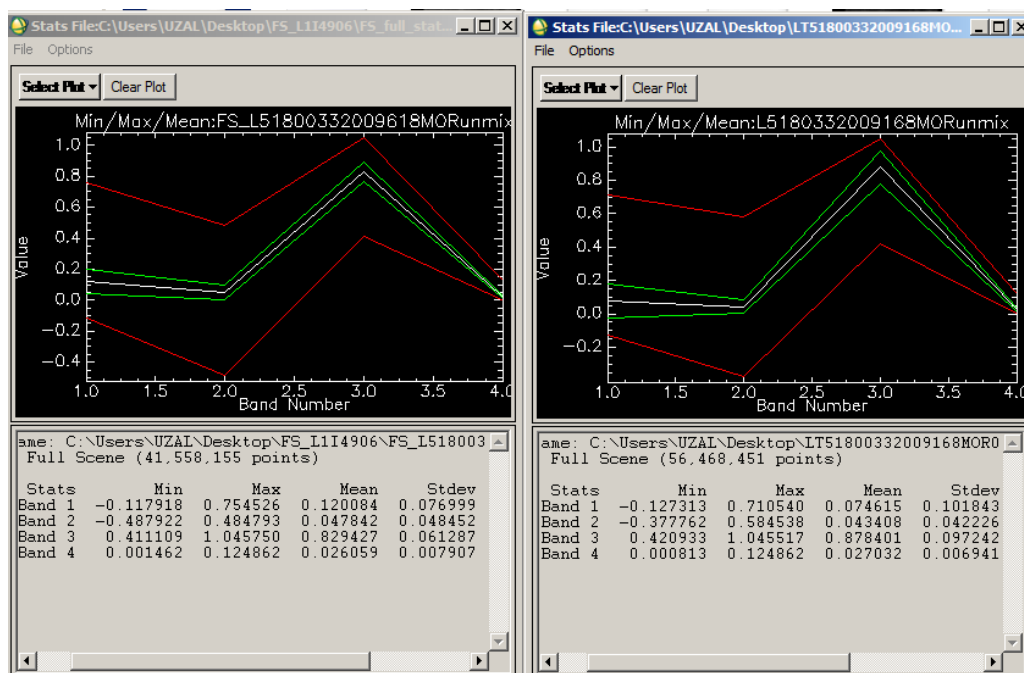
Figure 5.9 : Effects of resampling methods on full image (left image: NearestNeighbor, right image: Cubic Convolution).

41
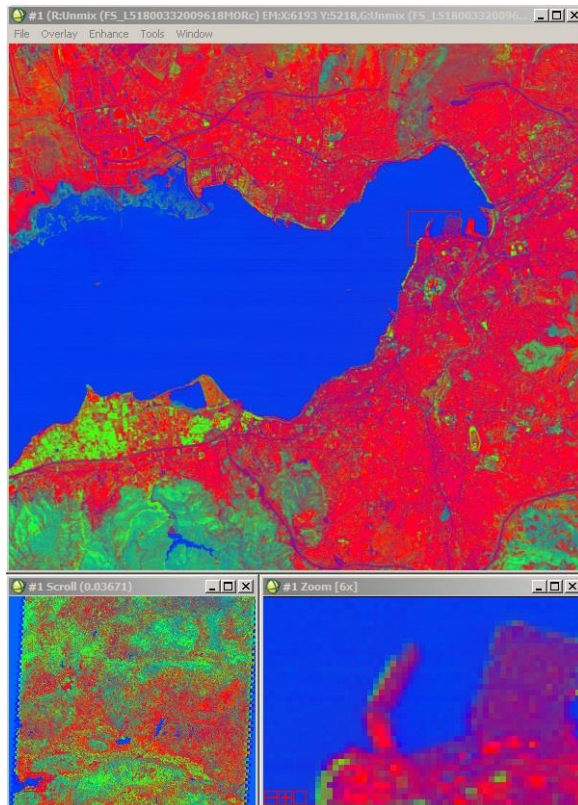
Figure 5.10 : NN method.
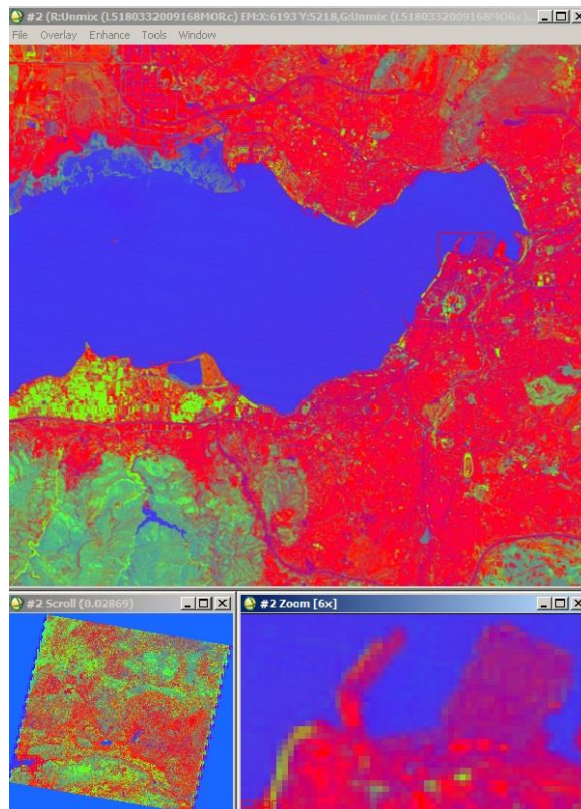
Figure 5.11 : CC method.

The test has been applied to the substrate area generated by both 'NN' and 'CC' resampling methods. Statistic value belong to first band, substrate, for both images had close results (Figures 5.12 and 5.13). Therore, resampling methods effects are negligible for this application so Landsat images downloaded as 'CC' has been used and analysed in the study.
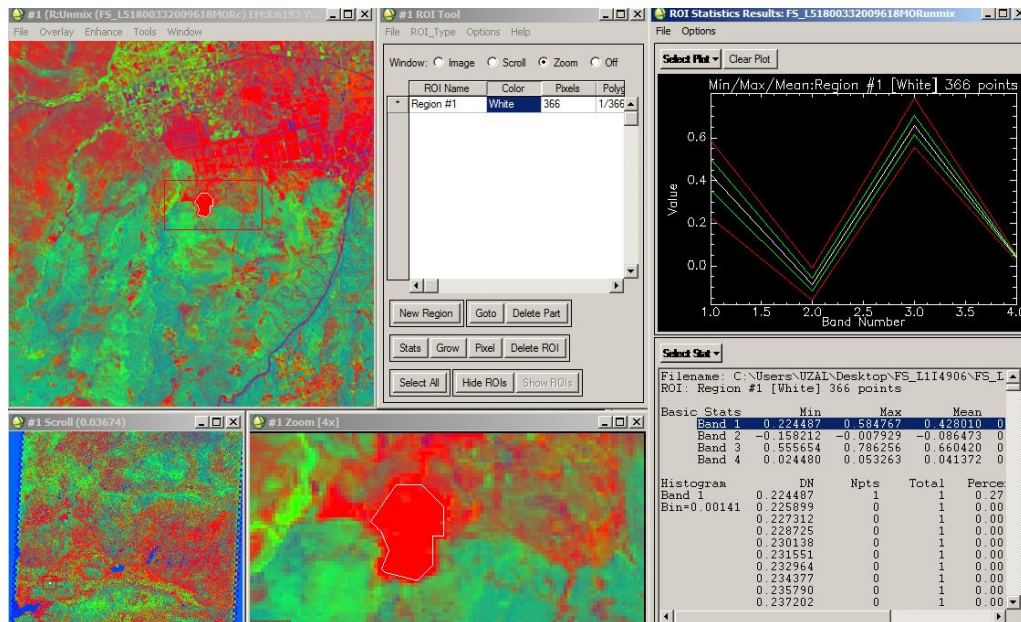
Figure 5.12 : Effects of NN method for substrate area.
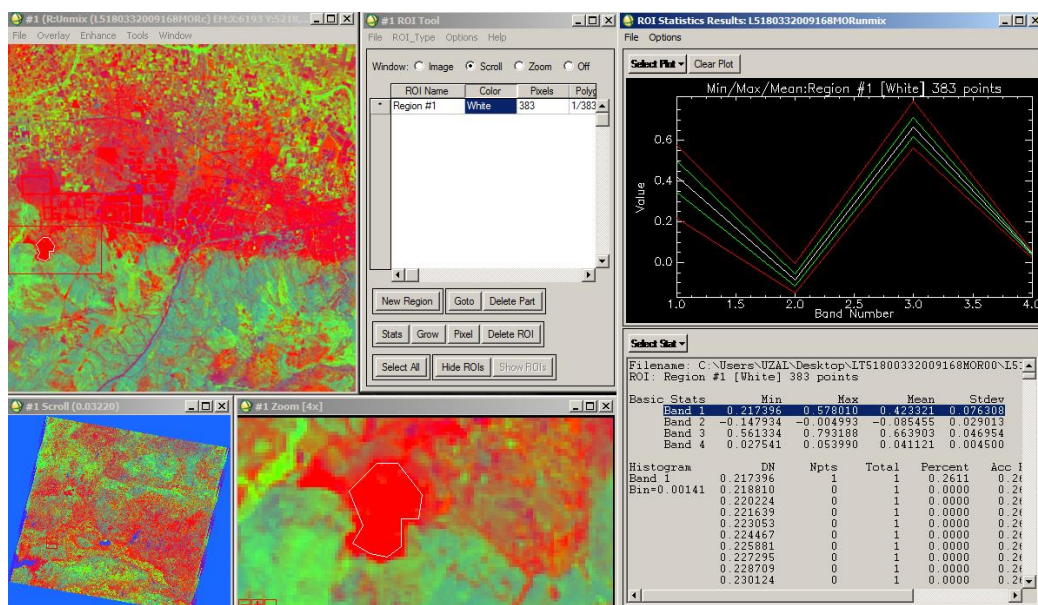
Figure 5.13 : Effects of CC method for substrate area.

The test has also been applied to the vegetation area generated by both 'NN' and 'CC' resampling methods. Statistic value belong to second band, which is related to vegetation, for both images had quite close results (Figures 5.14 and 5.15). Figure 5.16 shows that how to select pure vegetation area over the screen using scatter plot.
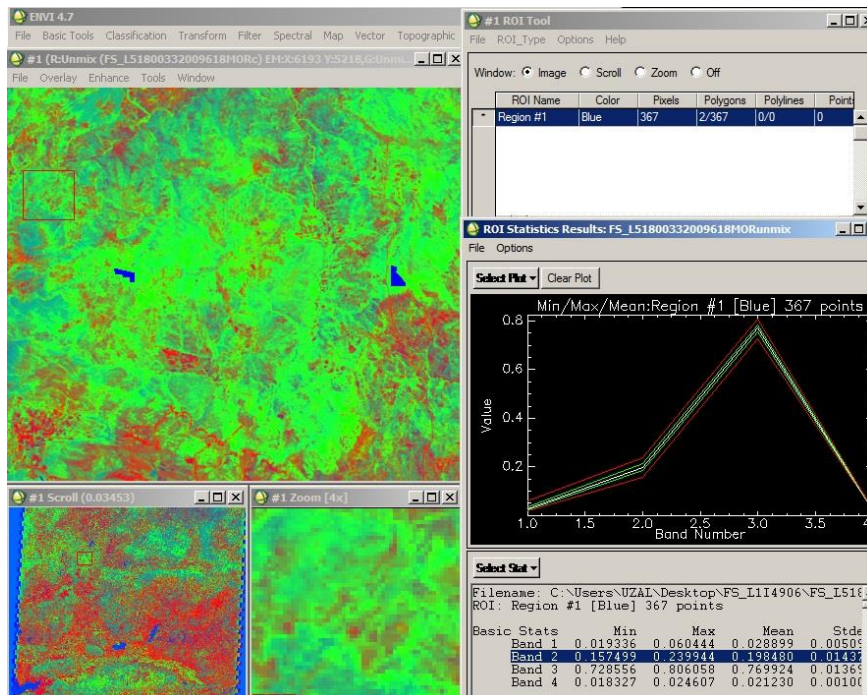
Figure 5.14 : Effects of NN method for vegetation area.
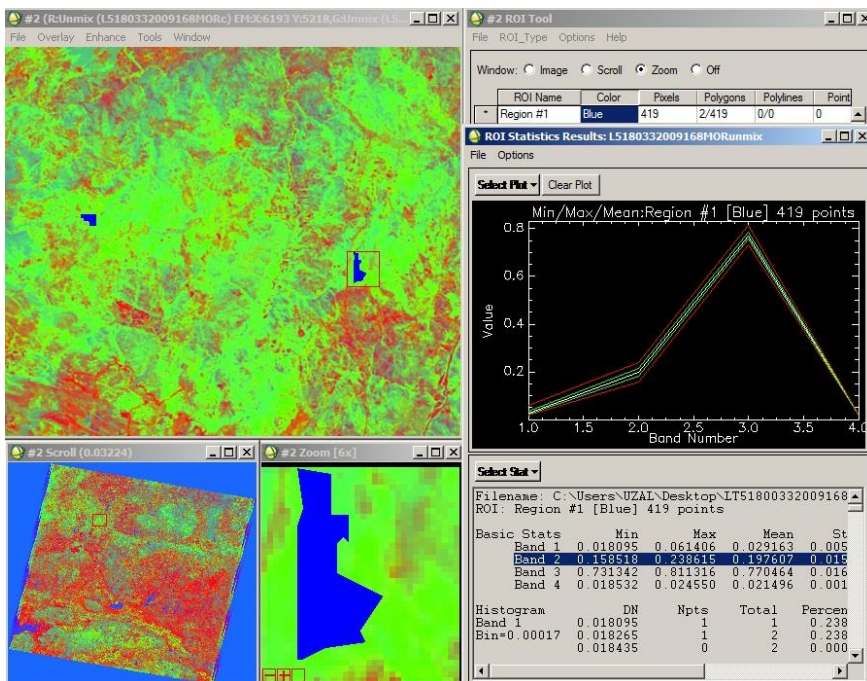
Figure 5.15 : Effects of CC method for vegetation area.
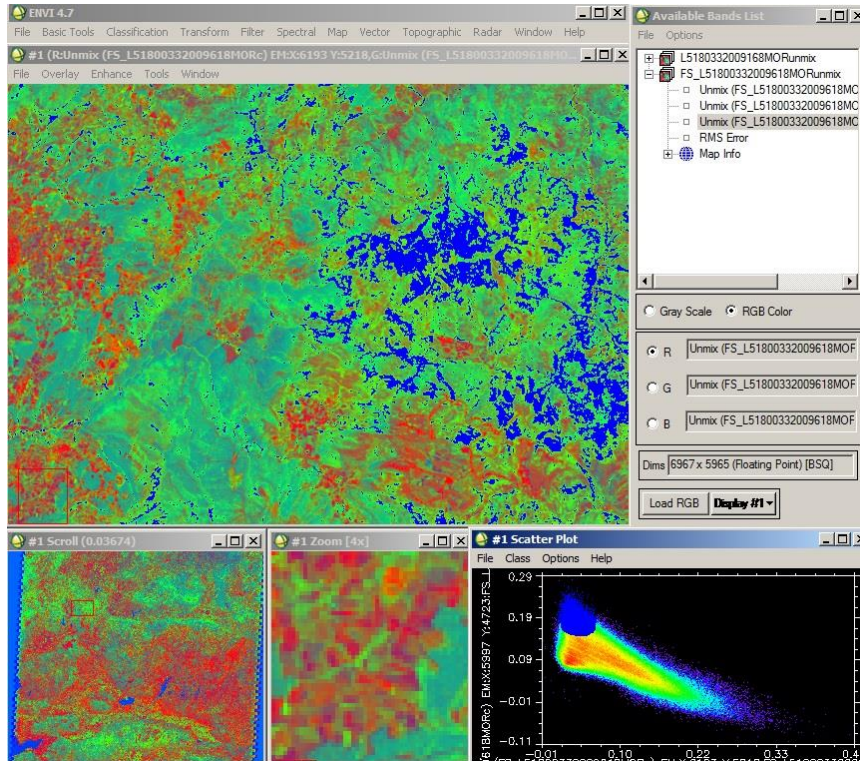
Figure 5.16 : Pure vegetation area selection.

In addition, the test has been applied to dark surface generated by both 'NN' and 'CC' resampling methods. Statistic value with respect to third band, which is related to water covered surface, for both images had almost same results (Figures 5.17 and 5.18).
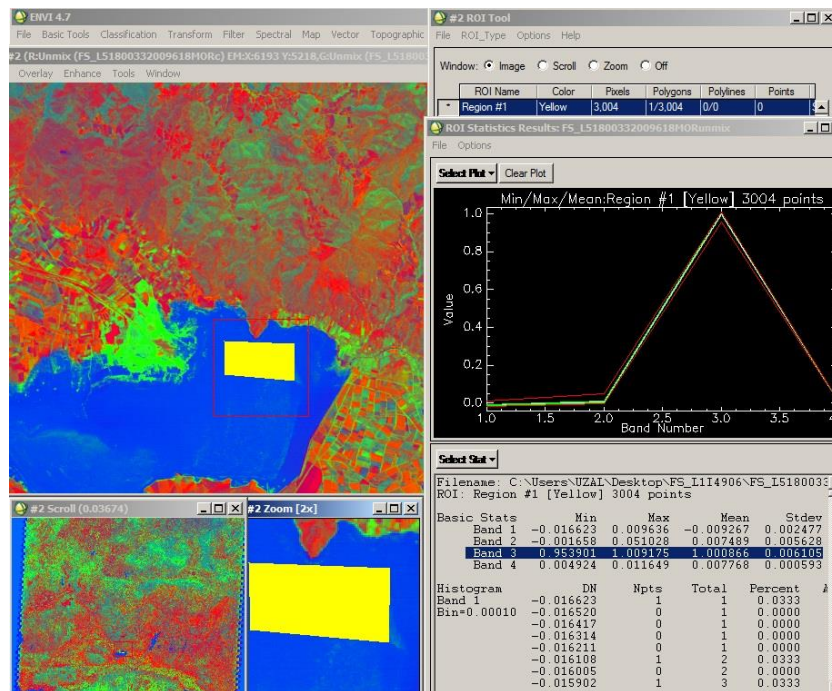
Figure 5.17 : Effects of NN method for dark surface.
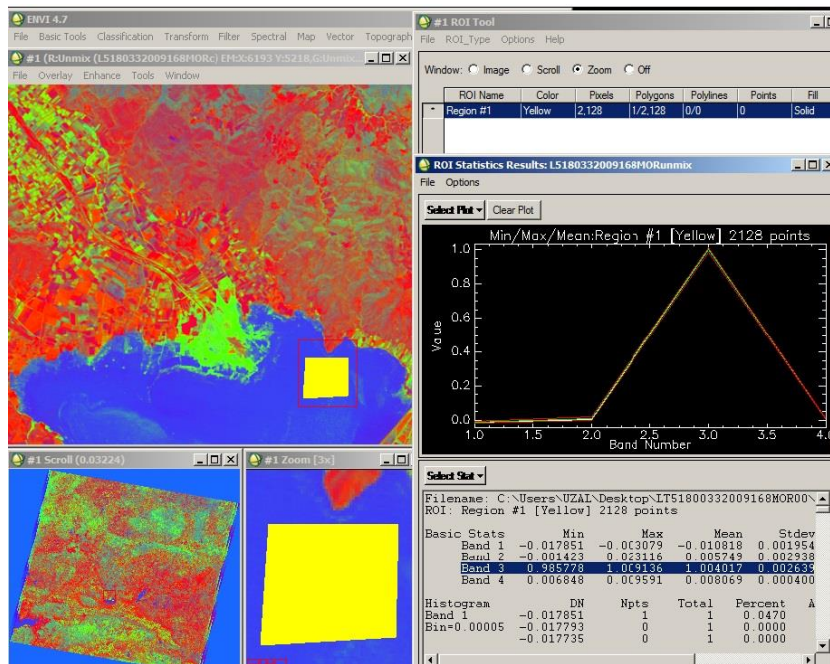
Figure 5.18 : Effects of CC method for dark surface.

5.3.2 Calibration of Landsat data

Most of Landsat data are processed as Level 1 terrain corrected (L1T) data. The L1T data are available in GeoTIFF format in the Universal Transverse Mercator (UTM) map projection with World Geodetic System 84 (WGS84) datum. The Level 1T processing involves radiometric correction, systematic geometric correction, precision correction using ground control points, and the use of a digital elevation model to correct parallax error due to local topographic relief.

In this study all the Landsat bands were used, except the panchromatic band, the bands used were the 30 m blue (0.45–0.52 μm), green (0.53–0.61 μm), red (0.63–0.69 μm), NIR (0.78–0.90 μm), and the two mid-infrared (1.55–1.75 μm and 2.09–2.35 μm) bands, and the 60 m thermal (10.40–12.50 μm) low and high gain bands. The L1T 8 bit digital numbers were converted to spectral radiance using sensor calibration gain and bias coefficients derived from the Landsat file metadata. The radiance sensed in the Landsat reflective wavelength bands the blue, green, red, near-infrared, and the two mid-infrared bands, were converted to top of atmosphere reflectance using the standard formula in chapter 4.

5.4 Method

Firstly, potential Landsat data were selected and downloaded from USGS-Glovis in this study. Images from 1984, 2000 and 2011 were chosen among the Landsat data to monitor and analyze the urban change areas within the study area. Special attention was paid for cloudlessness or cloudy ratio to be less than 10% while choosing these data. Radiometric calibration process was applied before applying the SMA method to selected images. Under normal conditions, spectral radiance sensed by Landsat sensors is stored as 8 byte DN. But these values should be converted to radiance and then to ToA reflectance values to minimize the changes arising from the sun - earth distance, solar geometry and spectral band differences. This process is important for Landsat data which are used for long time periods or wide areas. As in this study the changes during a period of approximately 30 years will be monitored, ToA reflectance values were calculated.

SMA method was applied to these atmospherically calibrated images. At this stage, the principle is to place the mixed space appropriately into a coordinate system. PC conversions are used to determine the size and topology of the mixed space quantitatively. These transformations have minimized the correlation between axes. In this study, PC band of the first two lowest order with the highest variance was used in creating the mixed space. This mixed space topology can be represented accurately only through the spectral endmembers to be selected (Small, 2001 and 2004). The endmembers used in this study consists of global SVD endmembers acquired by the assessment of images which may be applied for the worldwide study area and which are selected from different geographical regions (Small and Milesi, 2013). These SVD endmembers which are being used in global scale and mixed pixels are represented in percentages and linear spectral mixed model was obtained. DSVD maps were also prepared by taking the differences of SVD layers obtained for different dates. These difference maps obtained are important in terms of determining the changes occurring on LCLU in long time periods. Finally, analyses were conducted using the 'S' layers from the three different years selected especially for the assessment of changes in urbanization. The general flowchart which shows the method used has been seen in Figure 5.19. Also, to detect new urban areas derived from substrate maps, DMSP-OLS data has been used. In addition, images from Google Earth with high spatial resolution were used to validate the SMA results.
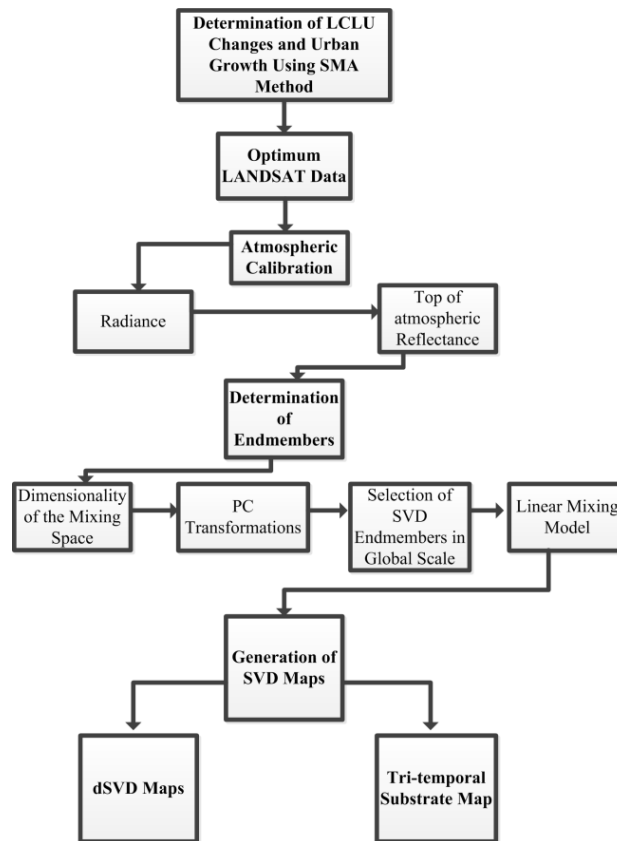
Figure 5.19 : Flowchart of the method.

5.5 Results

Analyses and results especially in Istanbul have been carried out detailed due to rapid urbanization and complexity of the city. LCLU changes in both sides of Istanbul were mapped and analysed and generating SVD and tri-temporal substrate map were explained detailed for the city. Moreover, color composites of fraction maps were generated only for Istanbul. For the other cities, only substrate fraction maps were used to analyse urban expansion. Also, some analyses were done with respect to seismic hazard in Istanbul and Izmit study areas. For the other cities, general urban LCLU changes were determined.

Istanbul

Figures 5.20, 5.21 and 5.22 have shown Landsat false color images using 7-4-2 band combination. Substrate, vegetation and dark surface fraction images was generated using SMA method for 1984, 2000 and 2011. Figures 5.23, 5.24 and 5.25 have shown substrate fraction since 1984. Fraction values range from 0 to 1 and 0 value corresponds to 0% substrate cover, while 1 value corresponds to 100% substrate cover.

According to these substrate fraction maps, substrate fraction has increased dramatically from 1984 to 2000. Especially new urban area needs have resulted in to increase of substrate in the city. Also, there has been slightly increase in substrate fraction from 2000 to 2011 and this increase has been detected towads out of the city.

Figures 5.26, 5.27 and 5.28 have shown vegetation fraction since 1984. The fraction of vegetation cover corresponds to the fraction of ground covered by green vegetation and it quantifies the spatial extent of the vegetation. Because it is independent from the illumination direction and it is sensitive to the vegetation amount. According to these maps, there has not been significantly changes in vegetation fraction except seasonal changes. In addition, these vegetation fraction maps have revealed considerable information about urban areas. In these maps, dark regions without surface covered by water have correspond to urban areas and their fraction values are very close to 0. Urban expansion in the city has been seen using these fraction maps.

Figures 5.29, 5.30 and 5.31 have shown dark surface fraction from 1984 to 2011. Changes in water covered surfaces have been detected from 1984 to 2000 using these fraction maps. Observing the changes in dark surface projection, changes on Buyukcekmece Lake and Sazlidere Dam were detected. Water covered surfaces show high values (very close to 1) in dark surface fraction maps. These fraction maps also give information about mixed pixels, which correspond to built-up areas such as urban areas. These figures have verified that urban areas have increased in the city since 1984.

Also, color composites of the fraction maps have been generated (Figures 5.32, 5.33 and 5.34). These maps have shown changes in substrate, vegetation and dark surface fraction for the selected years. Similarly, these maps have verified that urban expansion have increased in the city since 1984.

SVD linear mixture model was applied and SVD maps were generated using the global endmembers (Figures 5.35, 5.36 and 5.37). DSVD fraction maps were obtained by taking the differences of SVD values from selected different years. These maps have shown the changes in -S-, -V- and -D- values (Figures 5.38, 5.39 and 5.40).
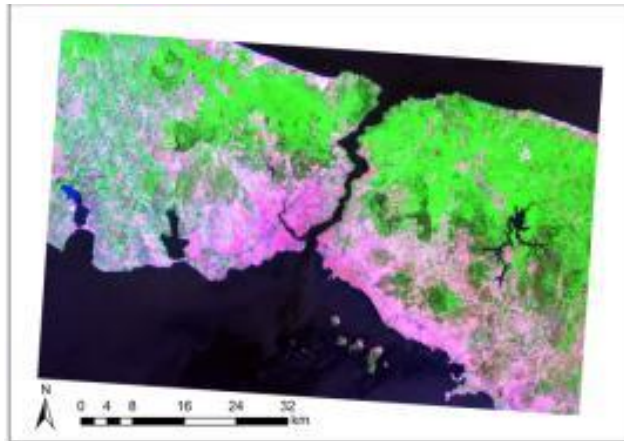
Figure 5.20 : Calibrated Landsat TM (12.06.1984).
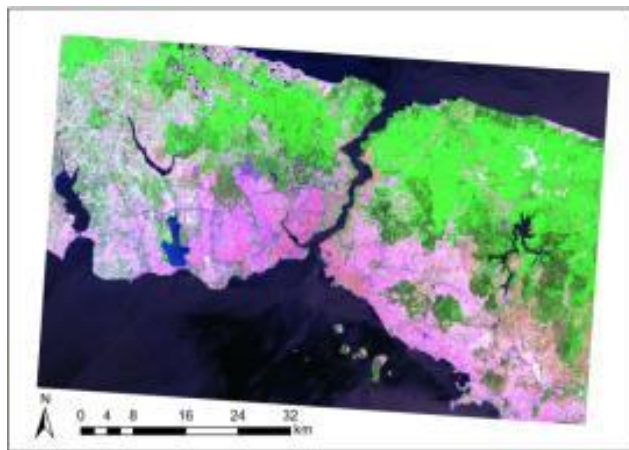
Figure 5.21 : Calibrated Landsat ETM (02.07.2000).
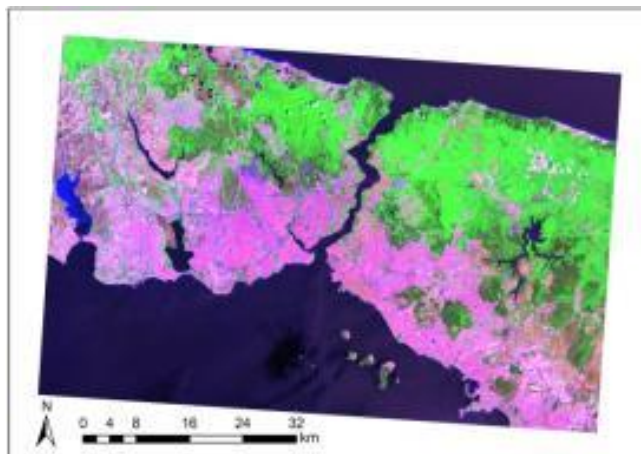
Figure 5.22 : Calibrated Landsat ETM (23.06.2011).
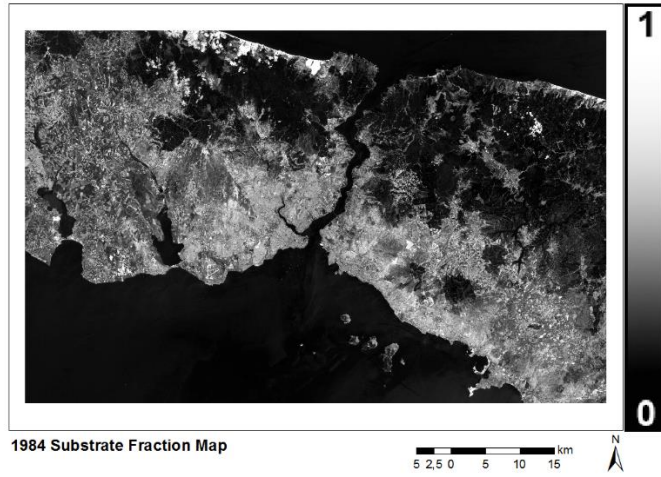
Figure 5.23 : Substrate fraction map of Istanbul (1984).
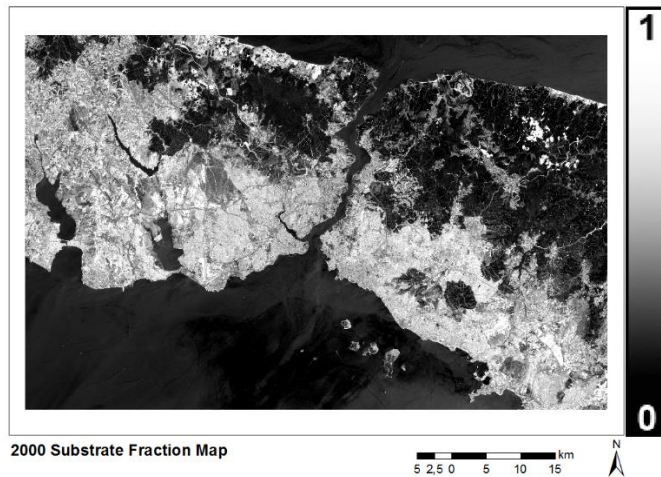
Figure 5.24 : Substrate fraction map of Istanbul (2000).
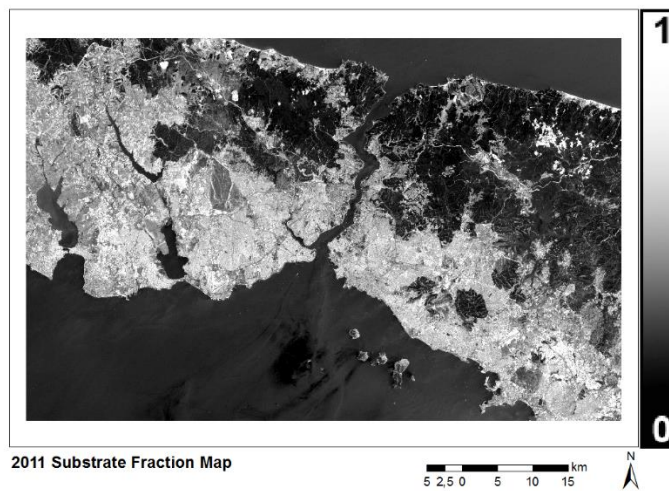
Figure 5.25 : Substrate fraction map of Istanbul (2011).
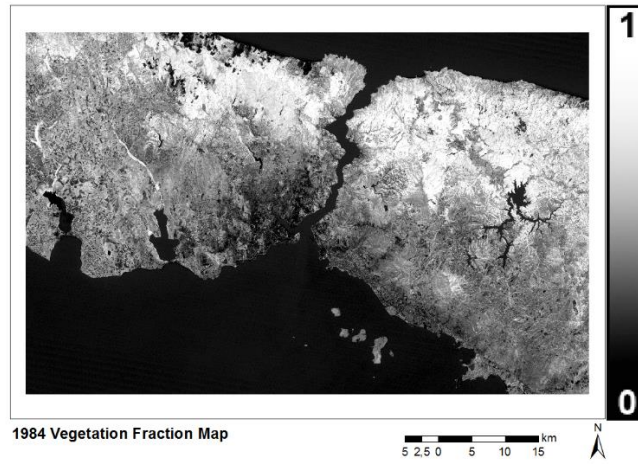
Figure 5.26 : Vegetation fraction map of Istanbul (1984).
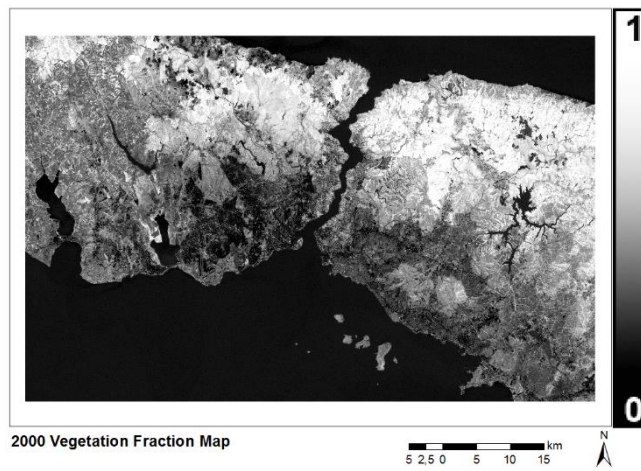
Figure 5.27 : Vegetation fraction map of Istanbul (2000).
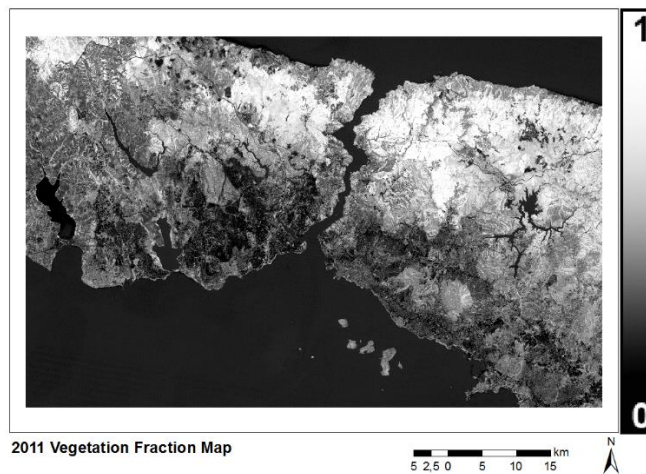
Figure 5.28 : Vegetation fraction map of Istanbul (2011).
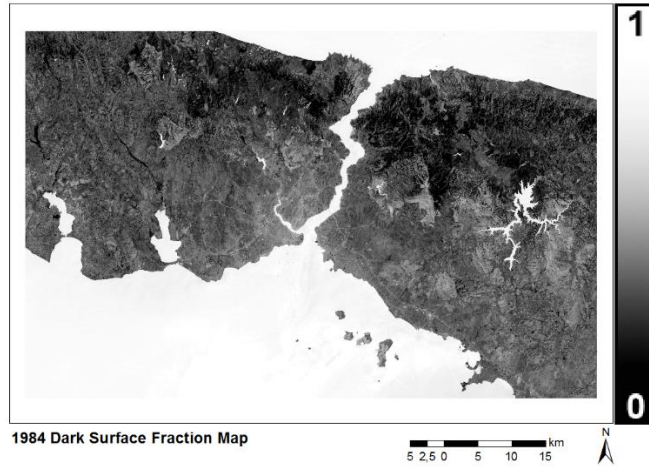
Figure 5.29 : Dark surface fraction map of Istanbul (1984).
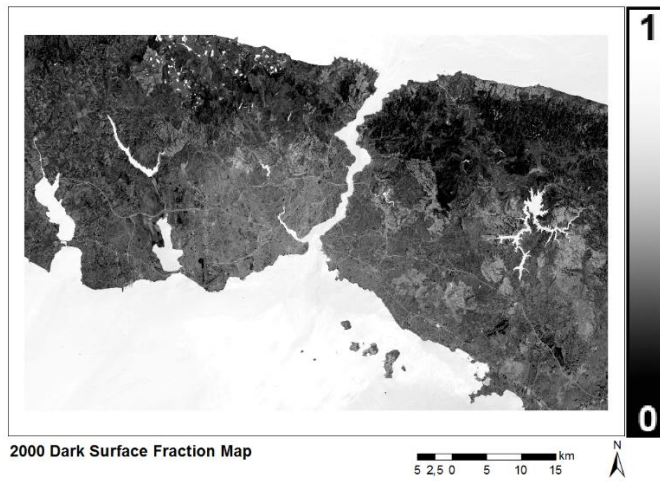
Figure 5.30 : Dark surface fraction map of Istanbul (2000).
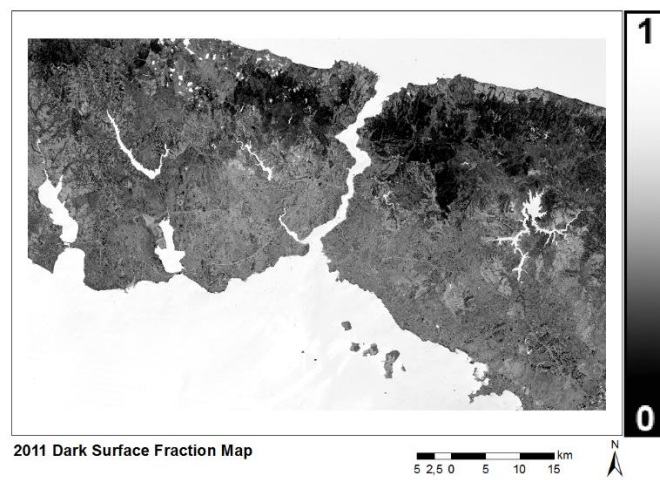
Figure 5.31 : Dark surface fraction map of Istanbul (2011).
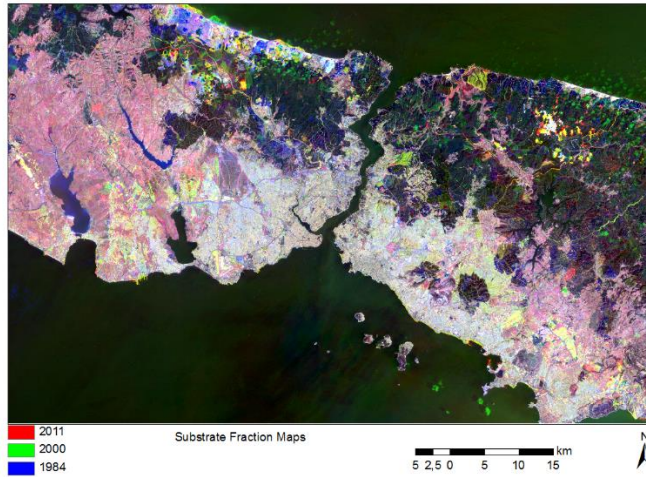
Figure 5.32 : Color composite of substrate fractions.
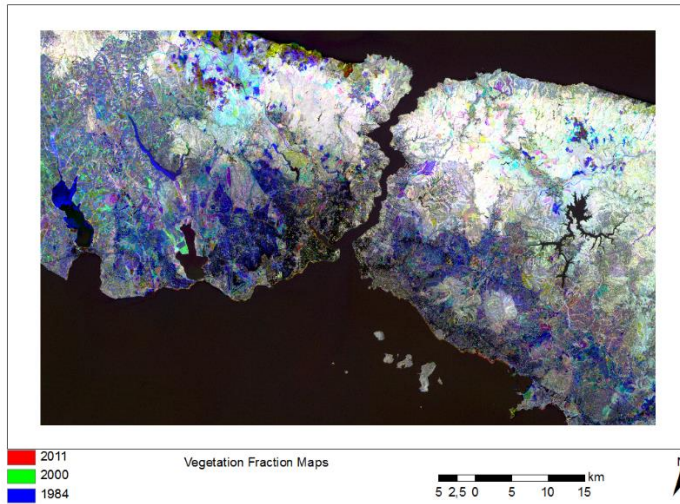
Figure 5.33 : Color composite of vegetation fractions.
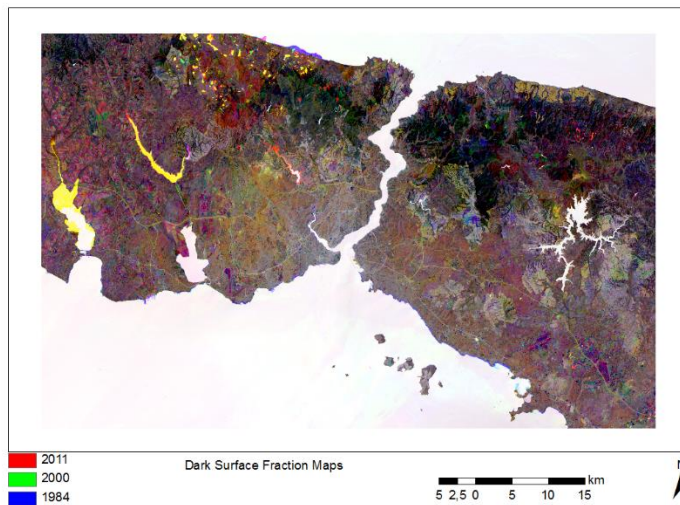
Figure 5.34 : Color composite of dark surface fractions.
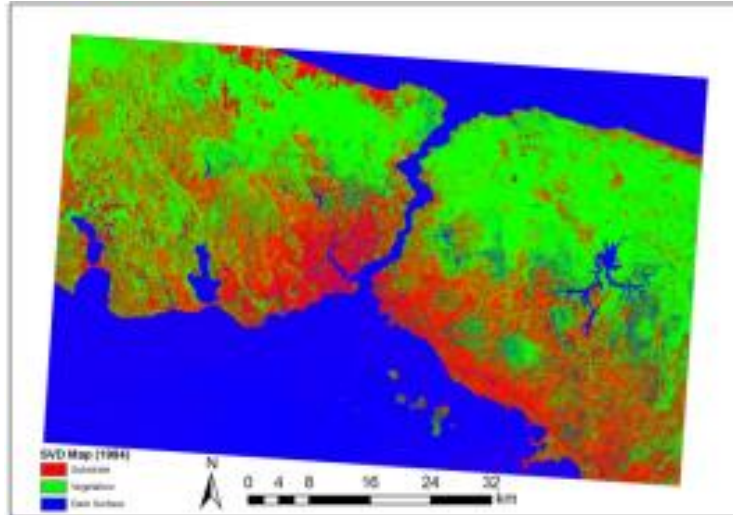
Figure 5.35 : SVD map of Istanbul (1984).
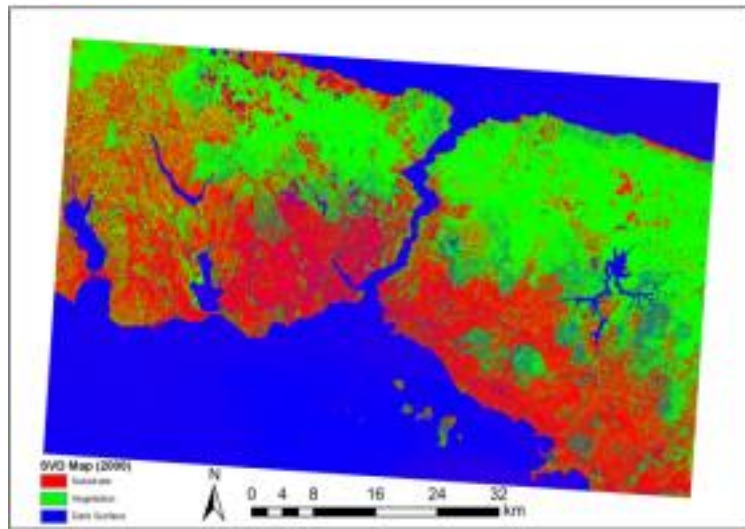
Figure 5.36 : SVD map of Istanbul (2000).
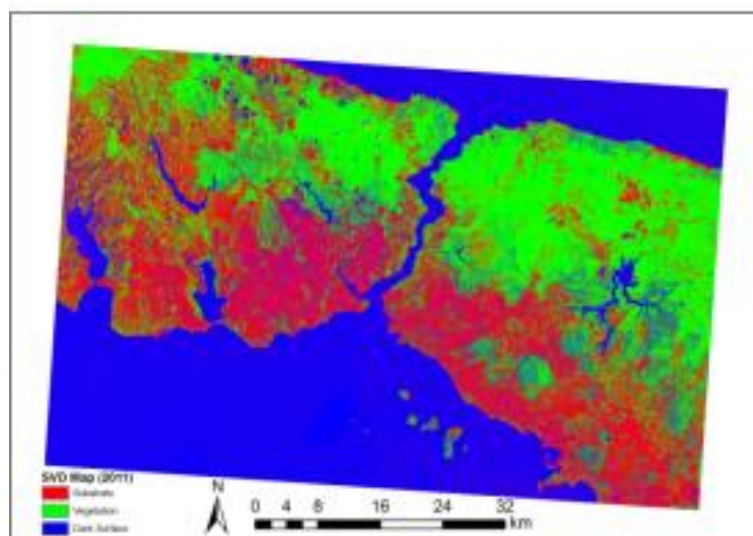
Figure 5.37 : SVD map of Istanbul (2011).

According to Figures 5.35, 5.36 and 5.37, it can be stated that S areas have increased from 1984 to 2011. This expansion has shown that the urban areas in the city spread along the north coasts of the Sea of Marmara and suburban regions towards outside of the city. Moreover, it is detected that the urban growth was more on the European side. Also, population of the European side is more than the Asian side. As the European side has more trade regions, immigrations have gained momentum especially in 1990s (Kaya and Curran, 2006). Figures 5.38 and 5.40 show the LCLU changes between 1984-2000 and 1984-2011, respectively. Particularly the increase in S values which refers to the recently built urban regions towards the west of the city is clearly seen. Figure 5.39 has shown that the rapid increase in S values from 1984 to 2000 has slowed down during the period between 2000 and 2011. The main cause of this is the reduce in the immigration rate from rural areas during that period (TurkStat, 2015). Again in Figures 5.35 and 5.36, S-D mixture is dominant especially in inner parts of the city and it has been observed that the D values increased much more between 2000 and 2011. In this situation, S values a little decreased and D values increased in the built-up areas of the city, it is consistent with an increase of shadow fraction from increasing urban growth. D values have increased due to shadow effect of the changeable height of buildings. High buildings have increased after 2000 especially in built-up areas and suburban regions of the city.
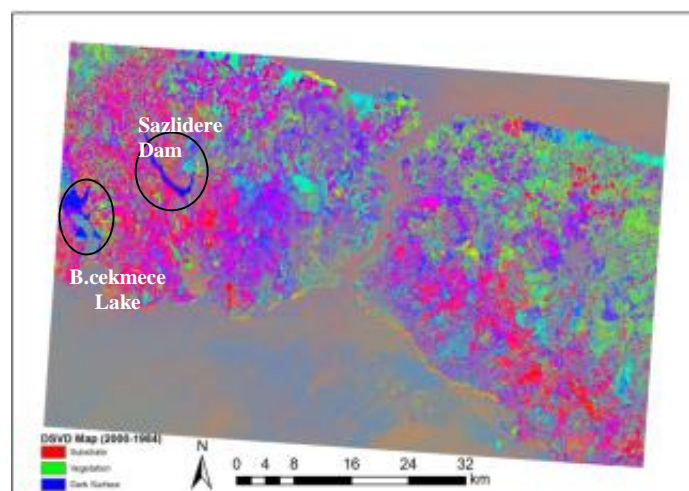
Figure 5.38 : DSVD map (shows the changes in S, V and D values between 1984 and 2000).
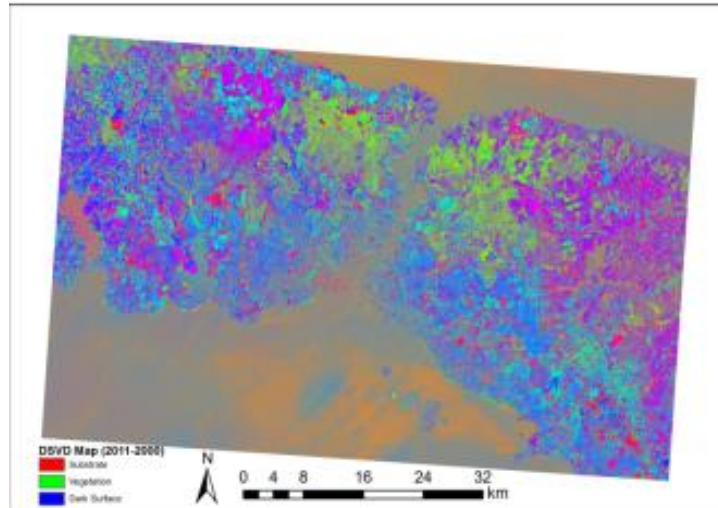
Figure 5.39 : DSVD map (shows the changes in S, V and D values between 2000 and 2011).
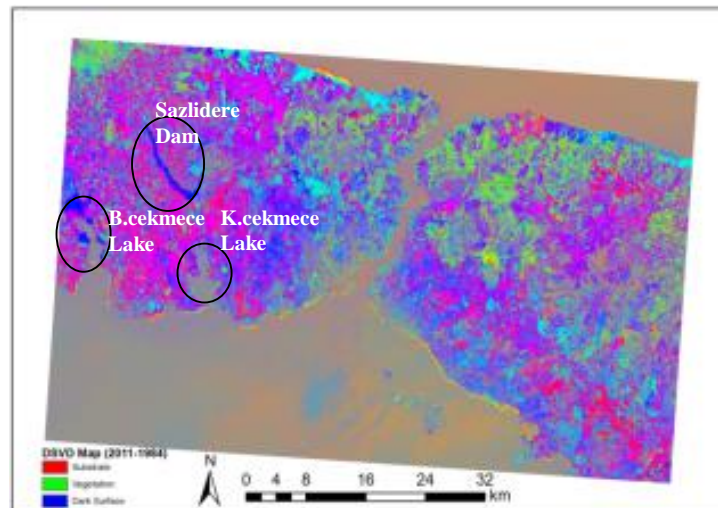
Figure 5.40 : DSVD map (shows the changes in S, V and D values between 1984 and 2011).

Apart from the SVD maps, tri-temporal (color composite of substrate fractions) substrate maps that shows substrate changes using only the S layers were also generated (Figure 5.41). According to this map, regions in which urbanization increased after 1984 have spread towards west and east of the city across the coasts of Marmara Sea. This zone is also known as risky seismic activity zone and it has been potential risk for densely populated areas (Fichtner et al., 2013).
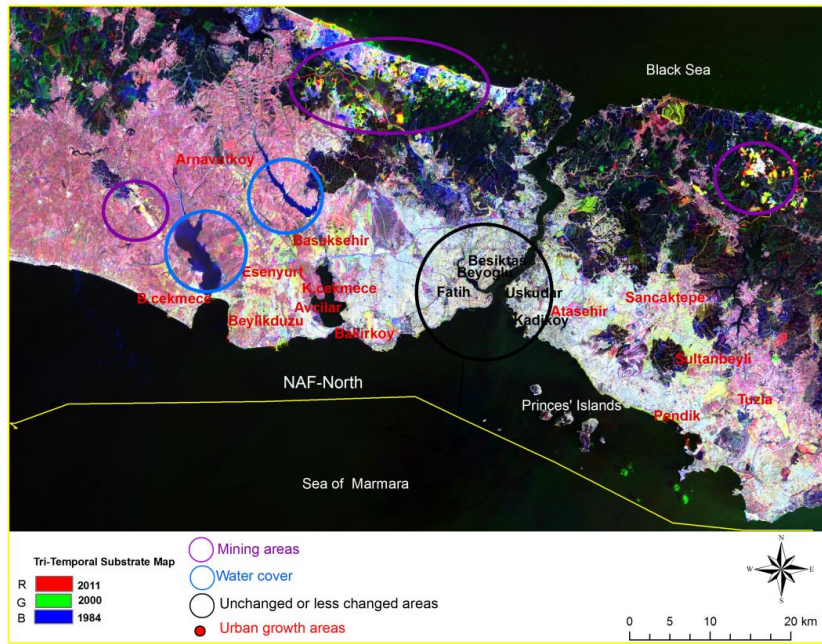
Figure 5.41 : Tri-temporal substrate map (Regions changed and remained unchanged according to the substrate values in 1984, 2000 and 2011).

The tri-temporal substrate map has shown that the increase in S values are observed in the region between Kucukcekmece and Buyukcekmece Lakes. It is determined that the new urban areas in Kucukcekmece, Buyukcekmece, Beylikduzu, Esenyurt, Basaksehir and Avcilar districts located in this region have expanded (Figure 5.41). The region between two lakes and Ikitelli Industrial zone in Basaksehir district to the northeast of Kucukcekmece Lake and areas around which were opened to settlement played a major role in the increase of S values (Sunar, 1998; Maktav et al., 2000). On the European side, new urban growth areas about 190 km^2.

On the tri-temporal substrate map, Sabiha Gokcen Airport and the region developed near it can be seen. The airport which was opened in 2001, industry zones and settlement areas are the regions in which the S increase is the most on the Asian side. There have been more than 110 km^2 urban growth areas on the Asian side in Sancaktepe, Sultanbeyli, Atasehir, Pendik and Tuzla districts (Figure 5.41).

Moreover, core areas in which were not subjected to any significant changes were detected. On the tri-temporal substrate map which shows the changes in the substrate values on 1984, 2000 and 2011, the change in S values and SVD values on LCLU determined in previous figures on the European side (Historical Peninsula) is very

small. However, there have been various historical buildings in this area which remain unchanged and in 1995, the area was declared as a first degree archaeological and urban-historical protected area (Dincer et al., 2011). Existence of dense settlement and refusing new settlements for the protection of the historic fabric prevented the product of new urban areas here. Also, many areas which do not show a significant change in years in S value are within the borders of core districts of Beyoglu, Fatih and Besiktas on the European side and Kadikoy and Uskudar on the Asian side (Figure 5.41). In addition, population densities in these districts did not change significantly and the did reduce even in some historical districts, such as Fatih and Beyoglu.

Also, water covered surfaces have been analysed from 1984 to 2000 in the study. Observing the changes in dark surface projection, changes on Buyukcekmece Lake and Sazlidere Dam, which have provided drinking and utility water to the city, were detected. Sazlidere Dam, which is not visible in the 1984 SVD and Landsat images, was constructed in 1996. Therefore, while being represented mainly by S and V values on the SVD map of 1984, this area is represented mainly by D value on the maps from 2000 and 2011. In 1984-2000 and 1984-2011 DSVD maps, this dam area with 10 km^2 surface area can be clearly seen as the change area (Figures 5.38 and 5.39). As a result of a dam constructed on the Buyukcekmece Lake in 1988, the lake area was enlarged and caused an increase in the D value in this area (Figures 5.38 and 5.39).

On the tri-temporal substrate map (Figure 5.41), another LCLU change is observed. On the Asian side, the increase in S values in the mining area located between the Omerli Dam and the Black Sea started in 1984 continues after 2000. Likewise, the change in mining areas lying along the coast of Black Sea on the European side is seen on SVD maps. These areas which are mainly represented by S value on Figure 5a are represented with S and D values between 2000 and 2011. This is caused by the water filled in gaps on the ground which occurred due to the mine searches. The decrease in S value around most mining areas in this region is replaced by the increase in D values. In the areas to the north and northeast of Arnavutkoy which are used as mining areas and quarry, and in the areas in Durusu, Yenikoy, Akpinar, Ciftalan and Kumkoy which lie parallel to the coast of Black Sea; some artificial ponds of varying sizes are located. New mining fields on these areas are the locations where S projection increases (Figure 5.41). Figure 5.41 shows quarries opened to the northwest of Buyukcekmece as

substrate area. This substrate area is not related to urban area because interannual changes in agricultural and mining phenology resulted in increase in substrate values.

All the results above derived from the tri-temporal substrate maps are not satisfactory enough. They mostly show substrate areas very well between 1984 and 2000. If there has been any constructions on these substrate areas after 2000, it would be difficult to determine them using usual methods and even tri-temporal substrate maps particular in small spaces of the city. Therefore, in this study DSVD maps were used to map vertical urban growth in the inner side of the city. In these small inner parts of the city, the areas were mostly involving S values in 2000, then the areas had mixture of S and mostly D values in 2011 so these increasing urban growth areas were determined using DSVD maps. According to DSVD maps, new urban growth areas after 2000 Basaksehir, Avcilar, Esenyurt, Beylikduzu and Arnavutkoy were determined on the European side of the city. Districts of Pendik, Umraniye, Cekmekoy, Atasehir, Sancaktepe and Tuzla were determined as urban growth areas on the Asian side of the city.

Figure 5.42 shows that the nighttime lights acquired by DMSP/OLS in 1992, 1999, 2012. The figure shows that the night lights have expanded since 1992 and it verifies the results acquired by SMA method.

Figure 5.42 : Nighttime DMSP image for Istanbul (1992(B), 1999(G), 2009(R)).

Izmit

Three Landsat data sets which cover Izmit were selected for 1984, 1999 and 2009 , and Landsat images were then calibrated using their parameters in their filenames. After these processes, SVD models were generated using a linear mixture model. In the study area, both settlement and industrial areas have been developed for these years. Figures 5.43, 5.44 and 5.45 show the original Landsat images with 30 m spatial resolution for the selected years, with RGB layers matched to 7-4-2 bands respectively. Figures 5.46, 5.47 and 5.48 show substrate fraction maps with respect to the selected years. Urban areas have shown high substrate fraction values. According to these maps, urban areas have grown towards east and south of the city.

Figures 5.49, 5.50 and 5.51 show SVD models for the same years. After SVD models for the years 1984, 1999 and 2009 were generated, SVD layers were subtracted from each other, generating DSVD models. Figures 5.52, 5.53 and 5.54 show differences in SVD models for the three years. Figure 5.52 represents DSVD between 1999 and 1984, Figure 5.53 shows differences between 2009 and 1999. In this duration, dark surface increased more than the others, and this result can be analyzed as an increase of the city's density. Figure 5.54 represents differences for SVD models between 2009 and 1984. SVD models acquired from linear mixture models and generated difference models both give more information about growth and density of urban areas. These results provide information not only for urban areas but also potentially for other LCLU changes. Substrate values increased from 1984 to 1999 and after 2009 dark surface values have increased. Dark surfaces (excluding water) represent density value for built up areas in cities. Vegetation has decreased from 1984 to 2011 in that duration, while substrate areas have increased.
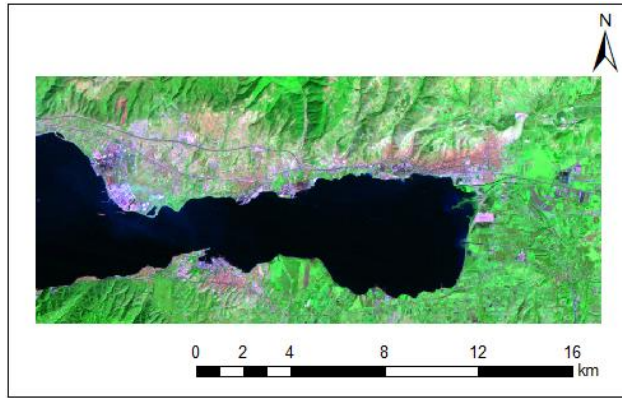
Figure 5.43 : Landsat TM (25.09.1984).
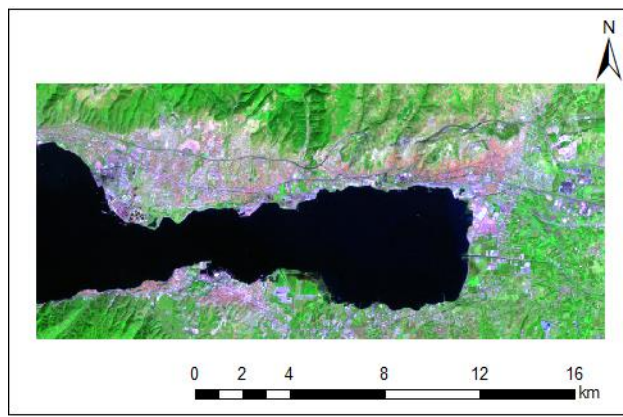
Figure 5.44 : Landsat ETM (27.09.1999).
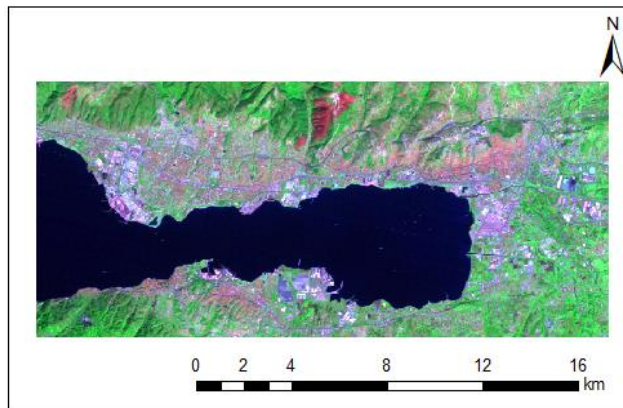
Figure 5.45 : Landsat ETM (30.09.2009).
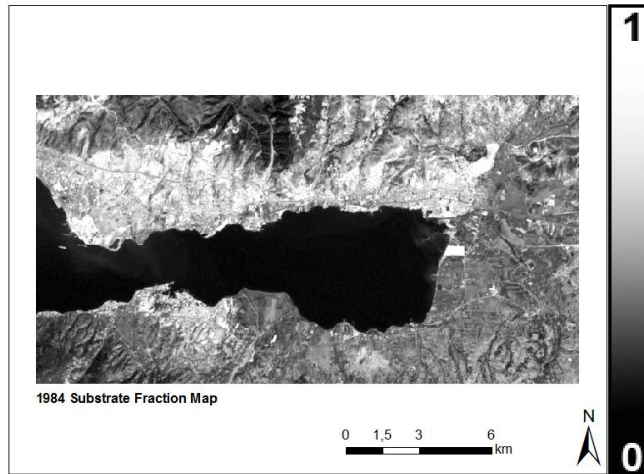
Figure 5.46 : Substrate fraction map of Izmit (1984).
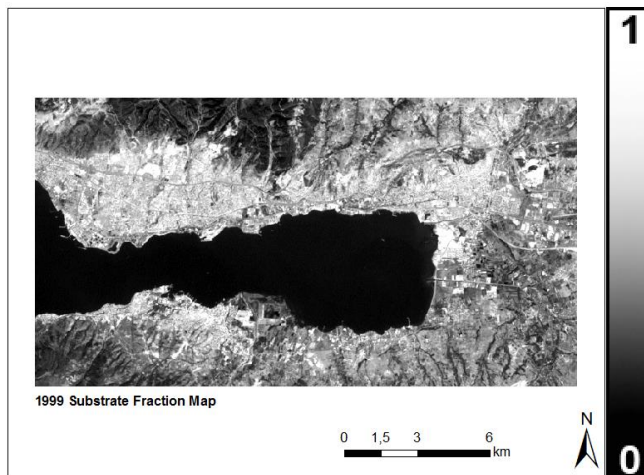
Figure 5.47 : Substrate fraction map of Izmit (1999).
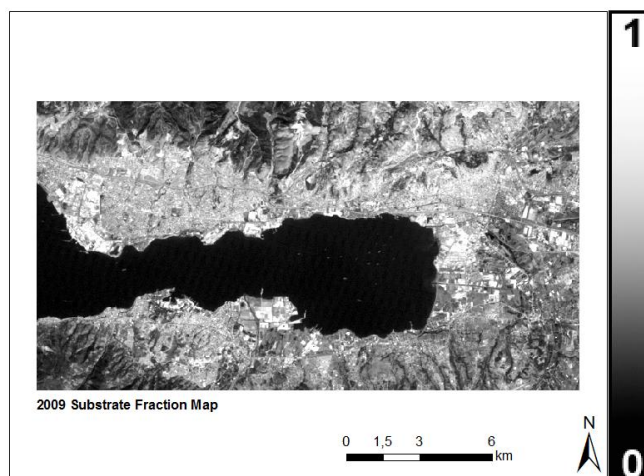
Figure 5.48 : Substrate fraction map of Izmit (2009).
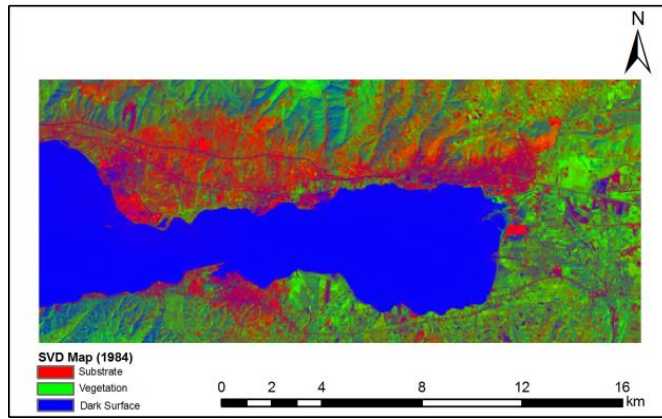
Figure 5.49 : SVD map of Izmit (1984).
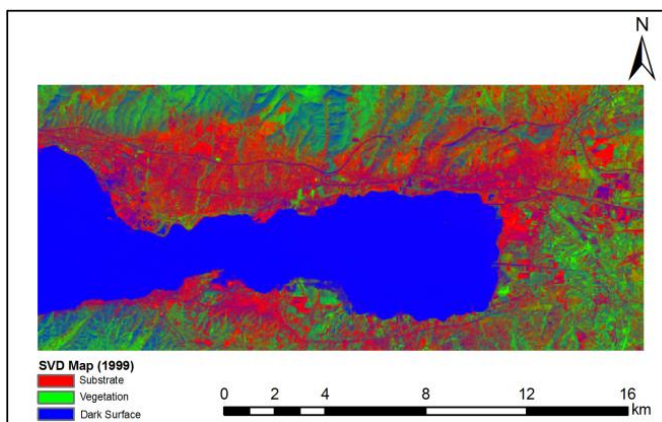
Figure 5.50 : SVD map of Izmit (1999).
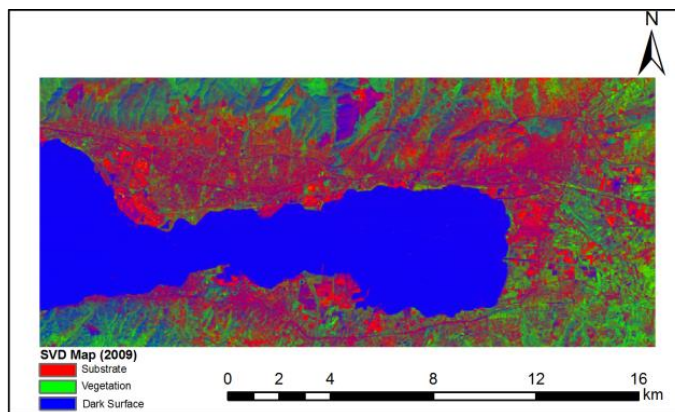
Figure 5.51 : SVD map of Izmit (2009).

DSVD maps may also be helpful to determine damages from natural disasters, like earthquakes. Both the Izmit and Golcuk were damaged by a magnitude 7.4 earthquake on August 17, 1999, that resulted in over 17,000 fatalities. The earthquake occurred along the North Anatolian strike slip fault that extends roughly east-west beneath the Gulf of Izmit (Aydoner, 2005).

Figure 5.52 shows the SVD differences between 1999 and 1984. The south shoreline of the Gulf appears dark blue, indicating that the dark surface value has increased dramatically from 1984 to 1999. The 1999 Landsat image was acquired 10 days after the Marmara Earthquake. Golcuk on the southern shoreline of the Gulf is the location of a Turkish naval facility and another automobile factory. Both areas were severely damaged by the earthquake, and the majority of the area was under water. Therefore, while dark surface reflectance value has increased, substrate and vegetation values have also decreased. A similar situation occurred for the Tupras petroleum refineries northwest of the Gulf of Izmit. The earthquake sparked a disastrous fire at the Tupras petroleum refinery. Breakage in water pipelines, resulting from the quake, nullified attempts at extinguishing the fire. Aircraft were called in to douse the flames with foam. The fire spread over the next few days, warranting the evacuation of the area within three miles of the refinery. The fire was declared under control five days later, after claiming at least seventeen tanks and untold amounts of complex piping (Scawthorn et al., 2005). The refinery area in Figure 5.52 appears dark because the area was under water and some chemical liquids were used to put out the fire, so dark surface reflectance is much higher than substrate reflectance. Figure 5.53 shows that substrate values have increased in both areas (Golcuk shoreline and Tupras refinery) because these areas have been built and repaired after the earthquake (Uysal and Maktav, 2015).
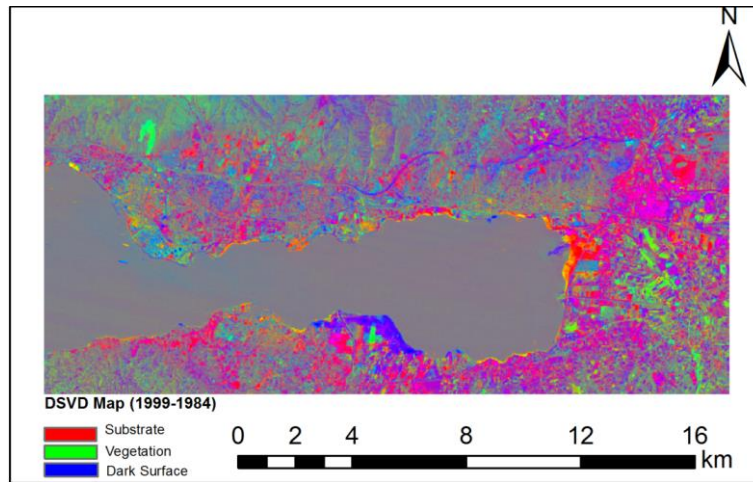
Figure 5.52 : DSVD map (between 1999 and 1984).
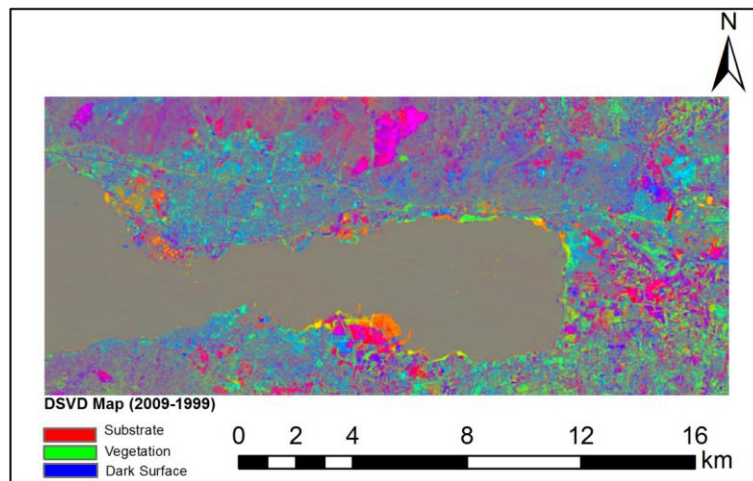
Figure 5.53 : DSVD map (between 2009 and 1999).
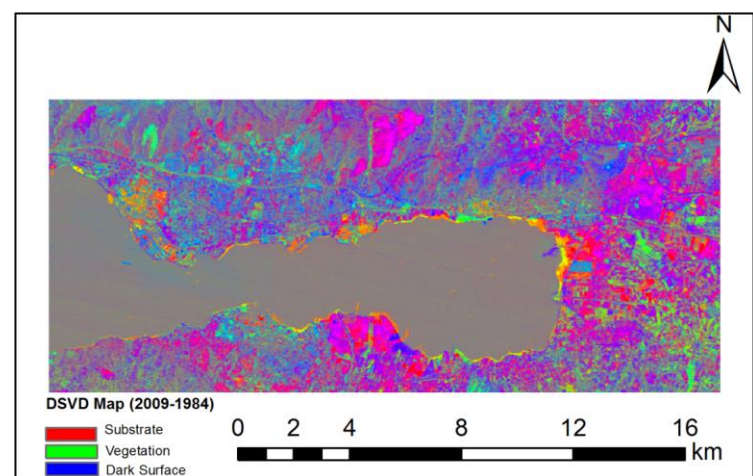
Figure 5.54 : DSVD map (between 2009 and 1984).

However, the main focus in this research was urban development. Therefore, S layers were more important than the others. All substrate images for three different years (1984, 1999, 2009) have been generated for the study area. These substrate images have been matched with RGB layers; red represented 2009 substrate image, green represented 1999 substrate image and blue represented 1984 substrate image. Therefore, new substrate areas (soil and settlement areas) after 2009 appear in red and similar tones. Substrate areas that have expanded after 1999 appear yellow or similar tones. Figure 5.55 shows a tri-temporal substrate map of the vicinity of the Gulf of Izmit. However, there are some large red areas towards the northern-central side of the study area, which is a forest region (cut forest area). Although they are not new urban areas, they have substrate reflection. DMSP data has been used to determine the forest region is not urban area (Figure 5.56).
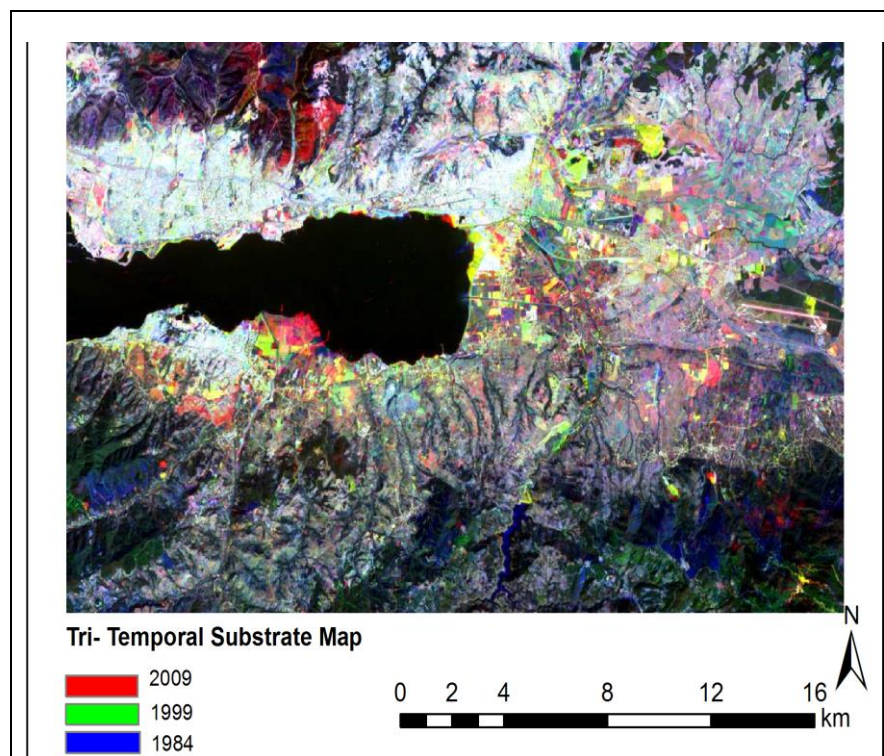
Figure 5.55 : Tri-temporal substrate map of Izmit.
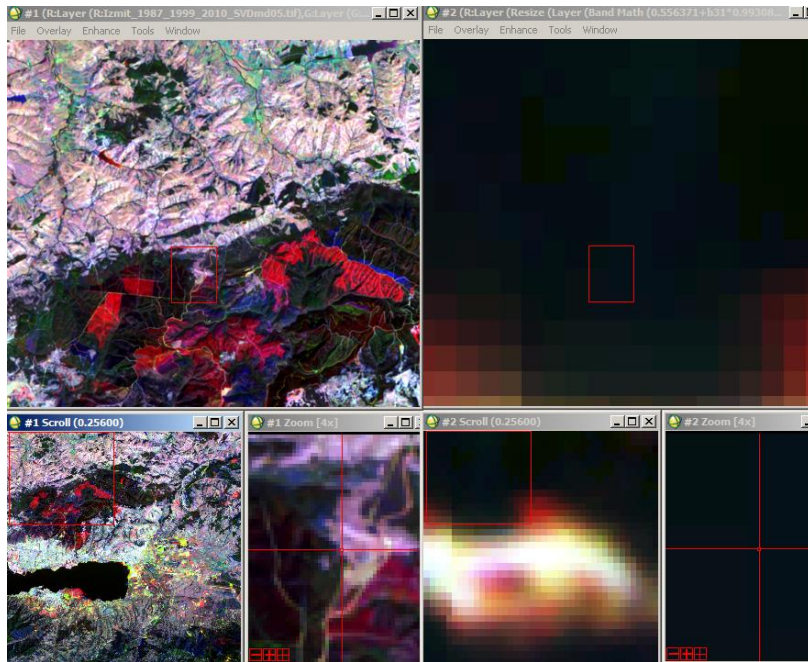
Figure 5.56 : Tri-temporal substrate map (left) and DMSP image.

Ankara

Figures 5.57, 5.58 and 5.59 show orginal Landsat images with 30 m spatial resolution for 1987, 2003, 2010 and RGB layers were matched 7-4-2 bands respectively.
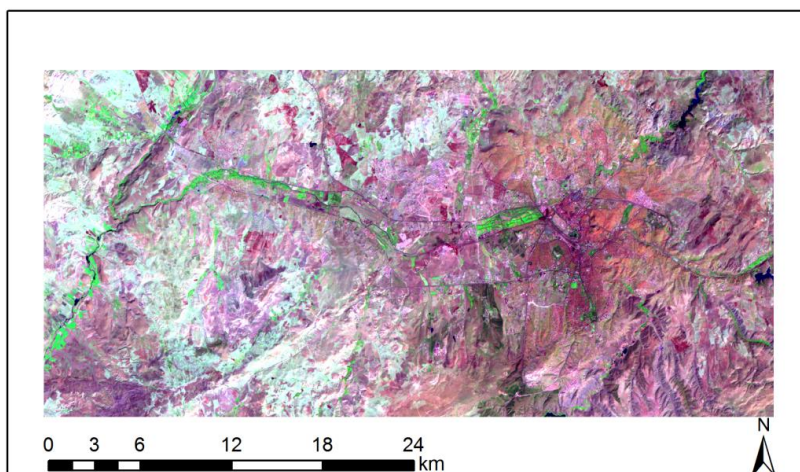
Figure 5.57 : Landsat TM image (20.08.1987).
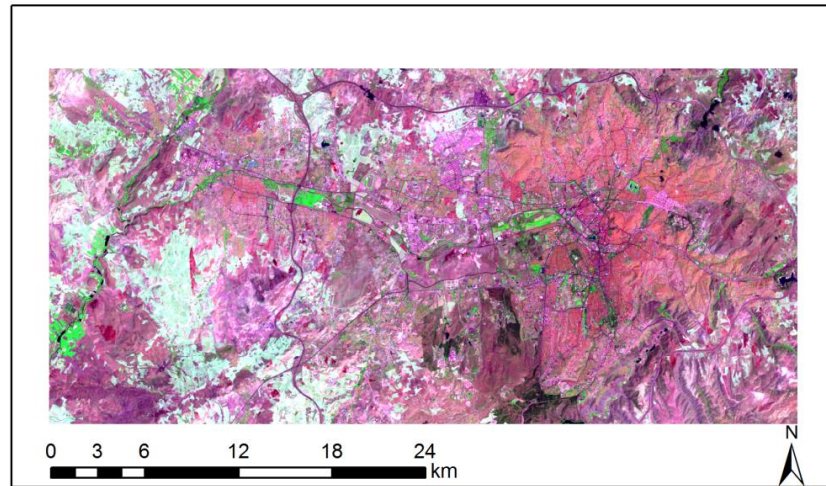
Figure 5.58 : Landsat TM image (15.08.2003).
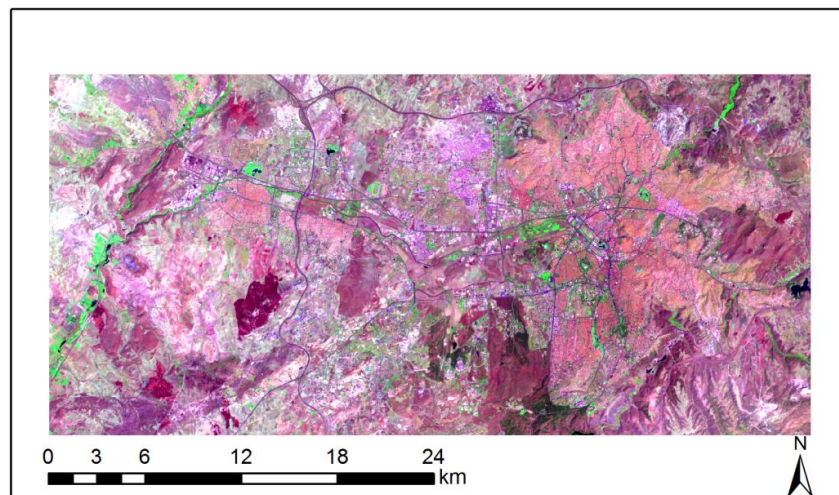
Figure 5.59 : Landsat TM image (18.08.2010).

Figures 5.60, 5.61 and 5.62 show substrate fractions for 1987, 2003 and 2010 respectively. Figures 5.63, 5.64 and 5.65 show SVD models for the selected years. In this study area, SVD maps have shown that there have been large areas with respect to substrate areas. The intensive substrate content, which shows high albedo, has not given meaningful results for the urban growth using only SVD maps. Also, green vegetation has rarely been seen in the study area. Therefore, especially the other DSVD and Tri-temporal substrate maps have been used for the analysis.
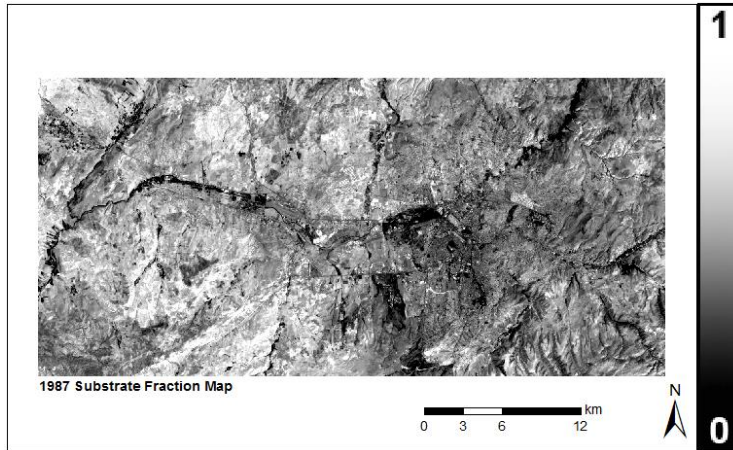
Figure 5.60 : Substrate fraction map of Ankara (1987).
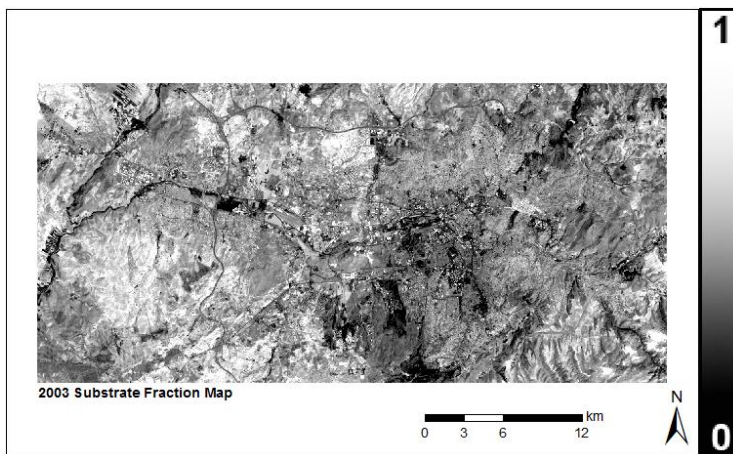
Figure 5.61 : Substrate fraction map of Ankara (2003).
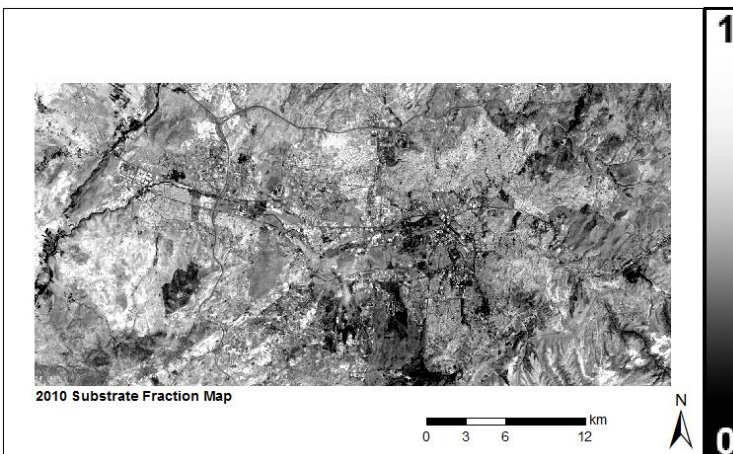
Figure 5.62 : Substrate fraction map of Ankara (2010).
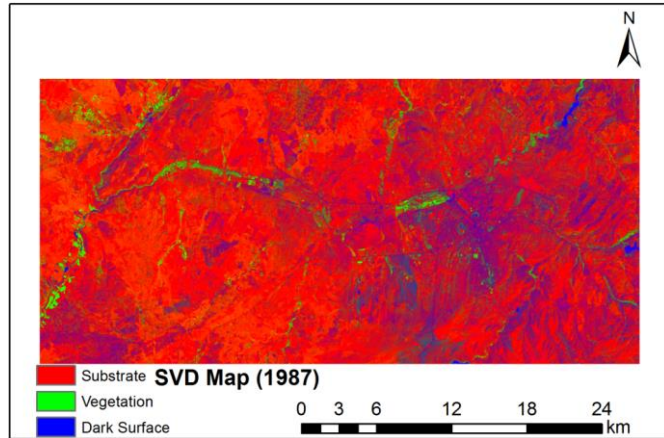
Figure 5.63 : SVD map of Ankara (1987).
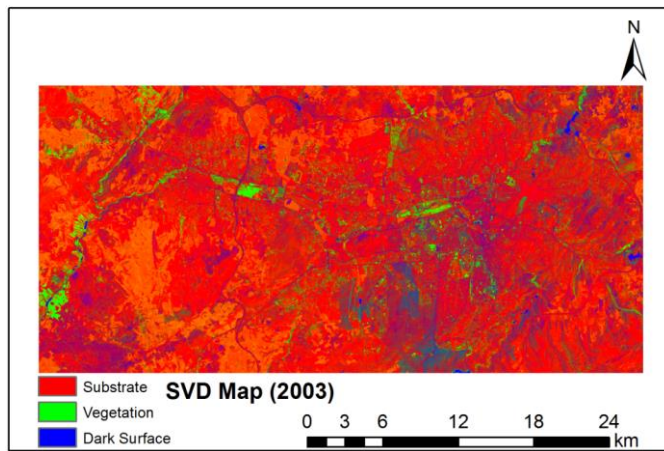
Figure 5.64 : SVD map of Ankara (2003).
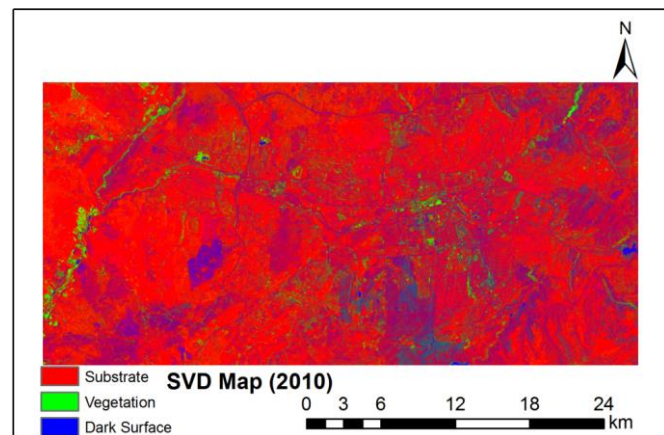
Figure 5.65 : SVD map of Ankara (2010).

When SVD layers were subtracted from each other, DSVD maps were generated (Figures 5.66, 5.67, 5.68).
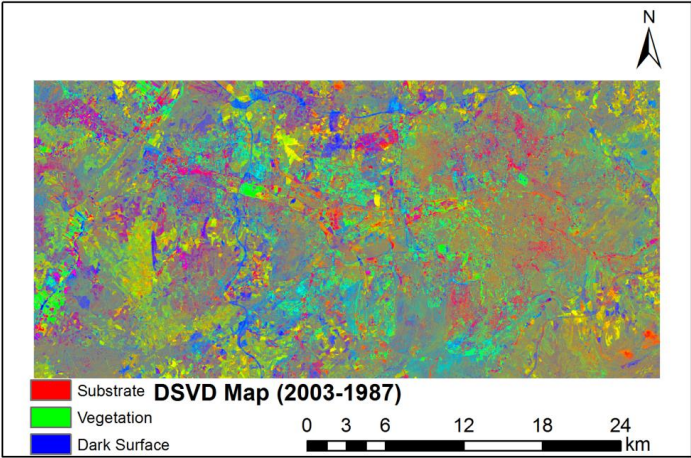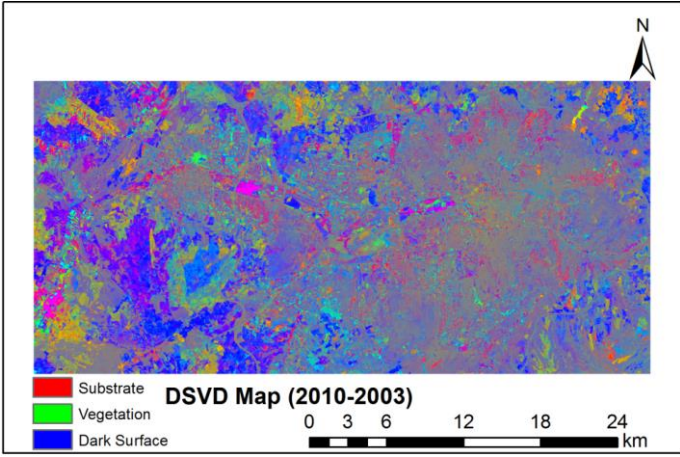

Figure 5.66 : DSVD map (2003-1987).

Figure 5.67 : DSVD map (2010-2003).
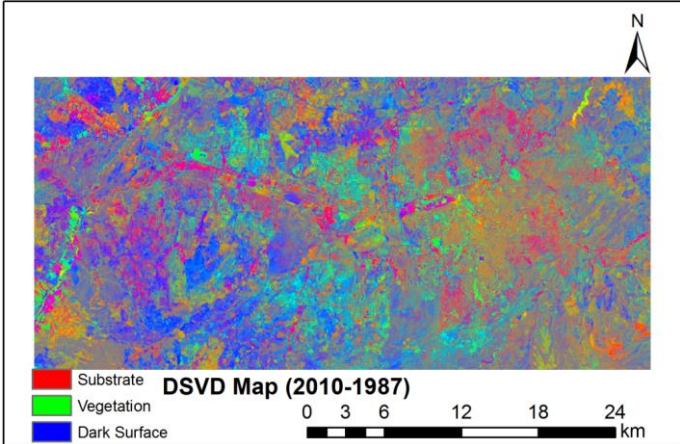
Figure 5.68 : DSVD map (2010-1987).

Figures 5.69 and 5.70 have shown urban growth in Ankara, especially north and west of the city has been growing in both maps. Although there has been very high substrate reflectance in the study area, tri-temporal substrate map has provided useful analyses related to urban growth. According to these analyses, the city has expanded towards to outside of the city. Especially new urban areas have increased out of the city especially in districts such as Etimegut,Sincan and Yenimahalle which have been in the west side of the city. Moreover, there have been another urban growth region in the north and this region has covered many districts like Kecioren, Altindag and Pursaklar.
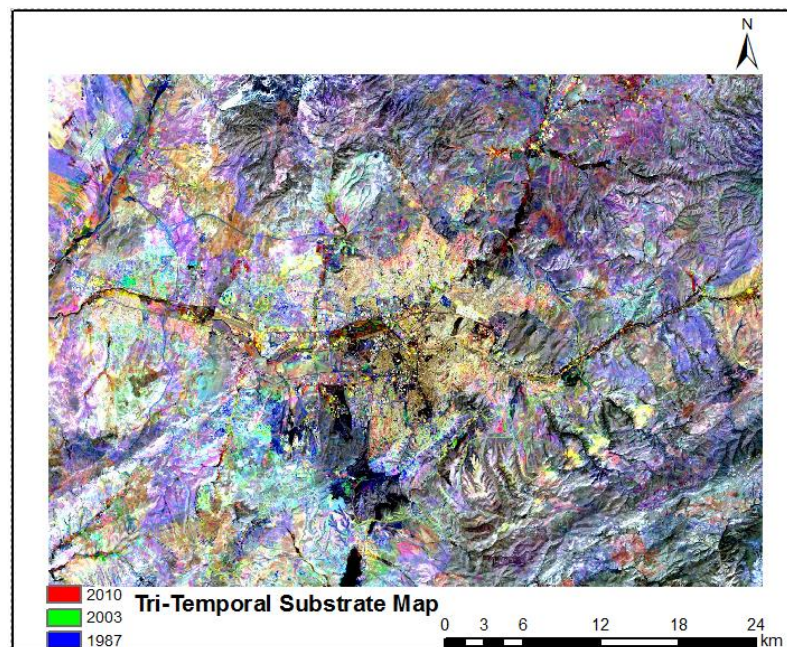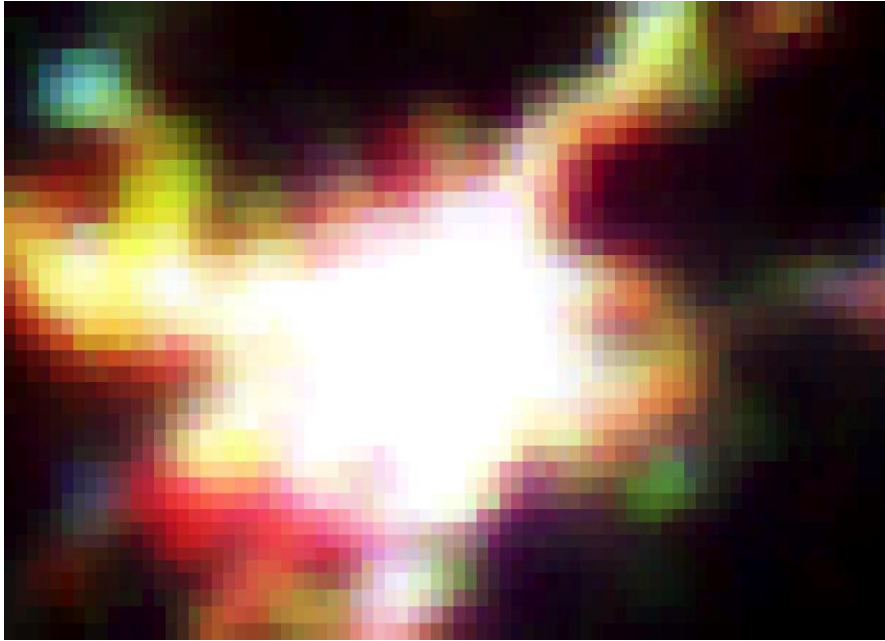

Figure 5.69 : Tri-temporal substrate map of Ankara.

Figure 5.70 : Nighttime DMSP image for Ankara (1992(B), 1999(G), 2009(R)).

Bursa

Similarly, SMA method have been applied to Bursa and urban growth areas have been acquired clearly. Years were selected as 1984, 2000 and 2011 from the calendar plots related to Bursa. Figures 5.71, 5.72 and 5.73 have shown Landsat false color images using 7-4-2 band combination. Figure 5.74, 5.75 and 5.76 show substrate fractions for 1984, 2000 and 2011 respectively. According to these substrate fraction images, the city has grown and expanded towards west and north of the city since 1984. SVD linear mixture model was applied and SVD maps were generated using the global endmembers (Figures 5.77, 5.78 and 5.79). DSVD fraction maps were obtained by taking the differences of SVD values from the selected years. These maps have shown the changes in -S-, -V- and -D- values (Figures 5.80, 5.81 and 5.82).
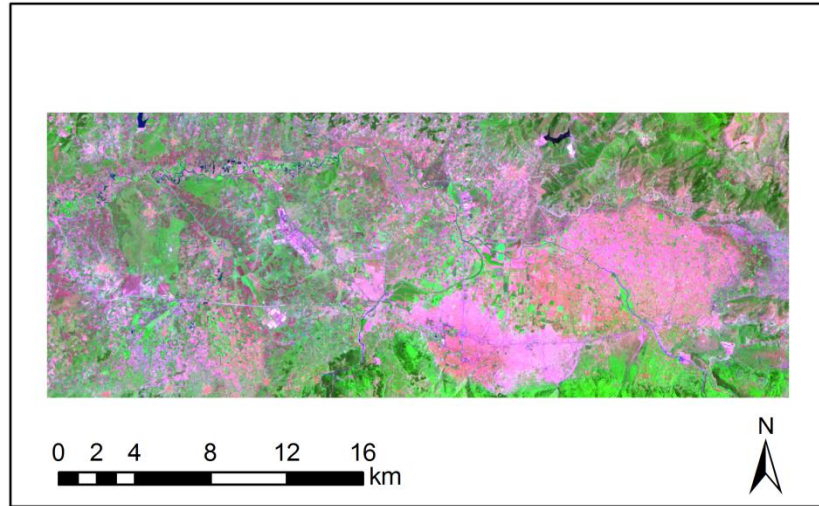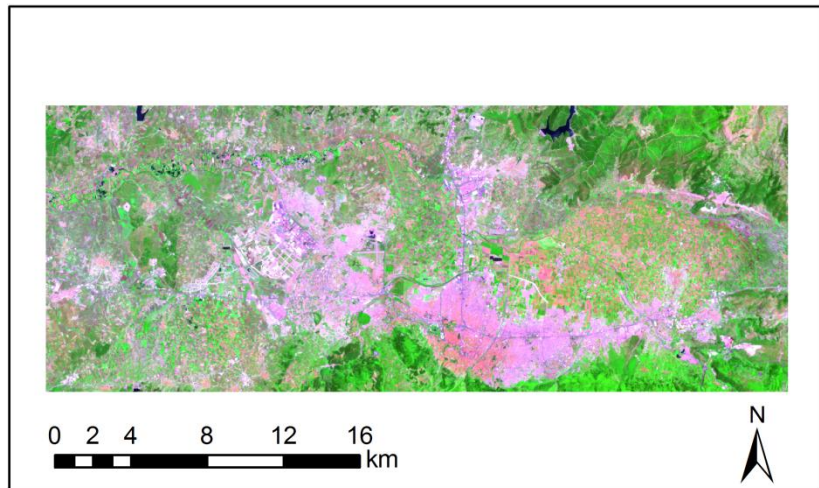
Figure 5.71 : Landsat TM image (12.06.1984).
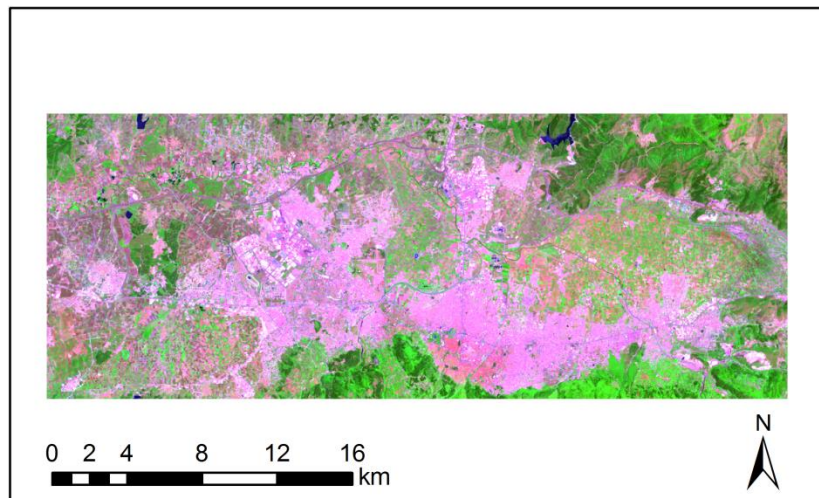

Figure 5.72 : Landsat ETM image (02.07.2000).

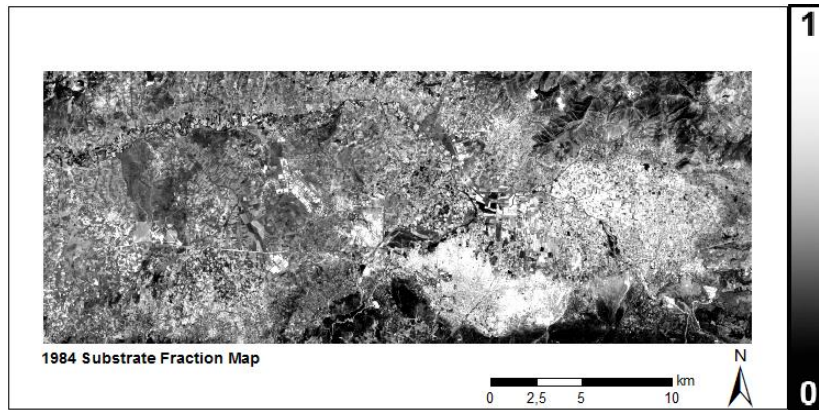**Figure 5.73 :** Landsat TM image (23.06.2011).

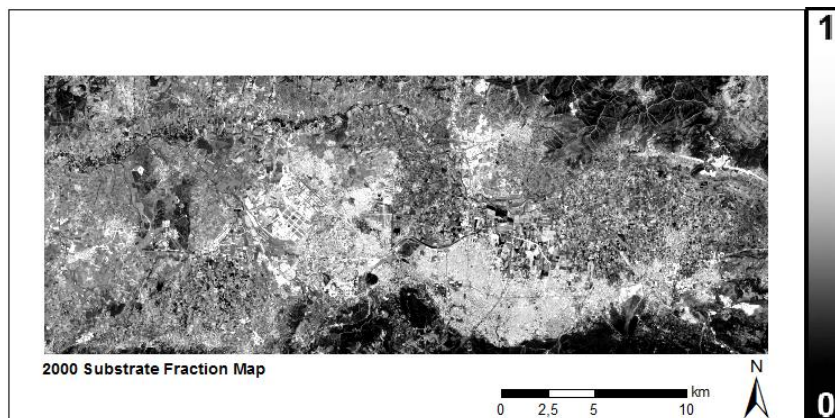**Figure 5.74 :** Substrate fraction map of Bursa (1984).

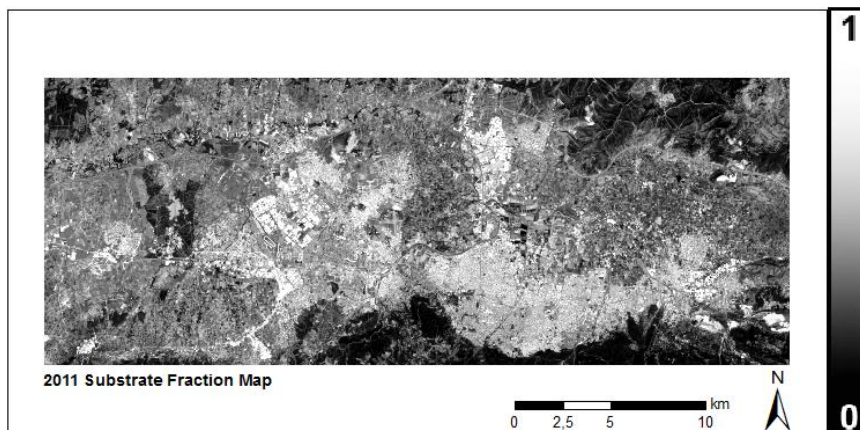**Figure 5.75 :** Substrate fraction map of Bursa (2000).

Figure 5.76 : Substrate fraction map of Bursa (2011).

In Figure 5.77 , the image has more substrate areas than the other two SVD maps (Figures 5.78 and 5.79) because this image has included agricultural area on the northeastern side of the it. Some seasonal varibility or harvest type or time may result in to this effect. But DSVD fraction maps have provided to solve this problem.
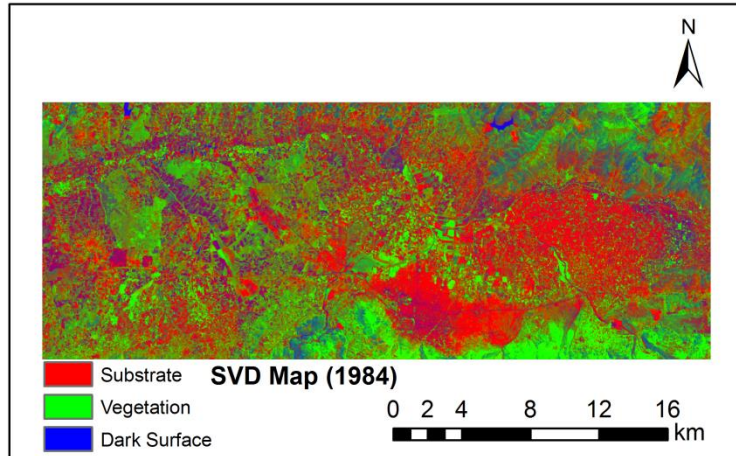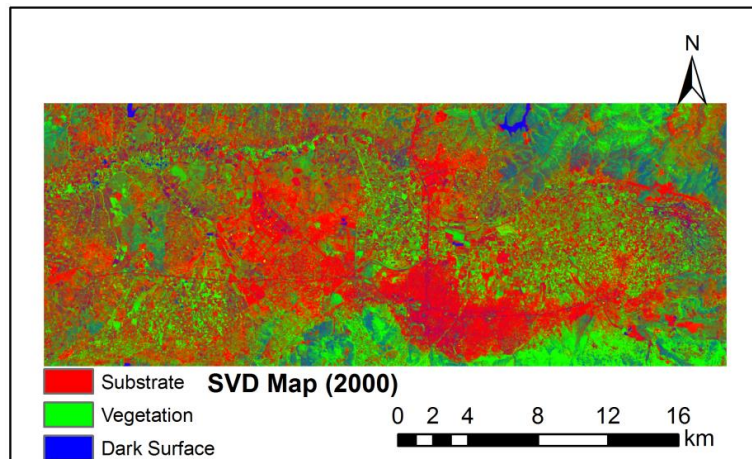
Figure 5.77 : SVD map of Bursa (1984).

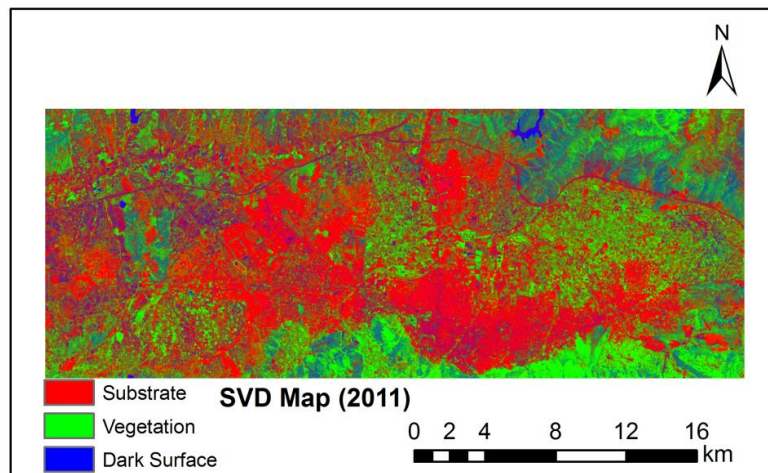**Figure 5.78 :** SVD map of Bursa (2000).

Figure 5.79 : SVD map of Bursa (2011).

The DSVD maps show that most new urban areas have increased towards to the west side due to industrial activities in this region. However, there have been densely

populated areas in the east of the city in which Osmangazi, Yildirim and Gursu districts have been. In the east side, there have been slightly growth towards to out of the city.
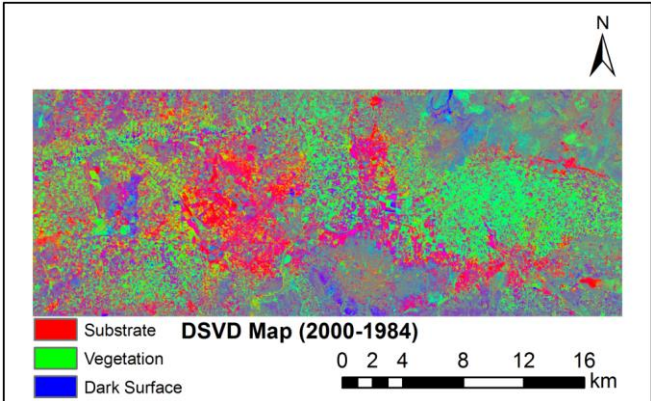

Figure 5.80 : DSVD map (2000-1984).
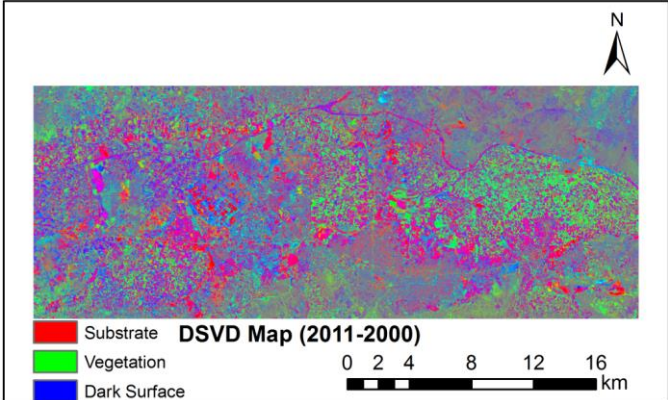
Figure 5.81 : DSVD map (2011-2000).
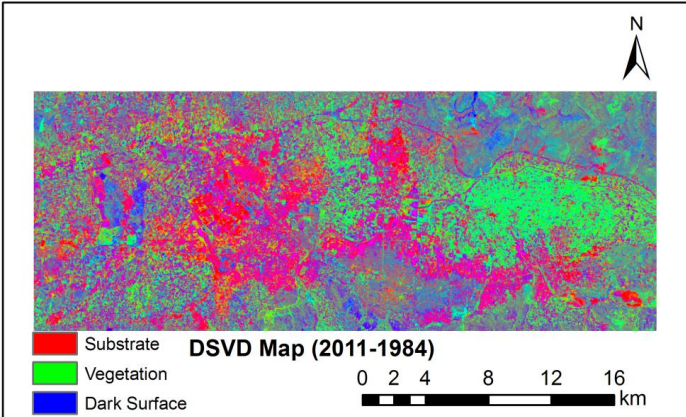
Figure 5.82 : DSVD map (2011-1984).

Not only DSVD maps but also tri-temporal substrate map have shown that the city has expanded to the west side of Bursa (Figure 5.83). Also Figure 5.84 which shows night lights since 1992 has almost provided same results. Increasing industrial region in the west have caused to densely urban areas especially in Nilufer district of the city.

Figure 5.83 : Tri-temporal substrate map of Bursa.

Figure 5.84 : Nighttime DMSP image for Bursa (1992(B), 1999(G), 2009(R)).

Kayseri

The Landsat data sets which include Kayseri were selected for 1987, 1998 and 2010 , and these images were then calibrated using their parameters in their filenames. After this procedure, 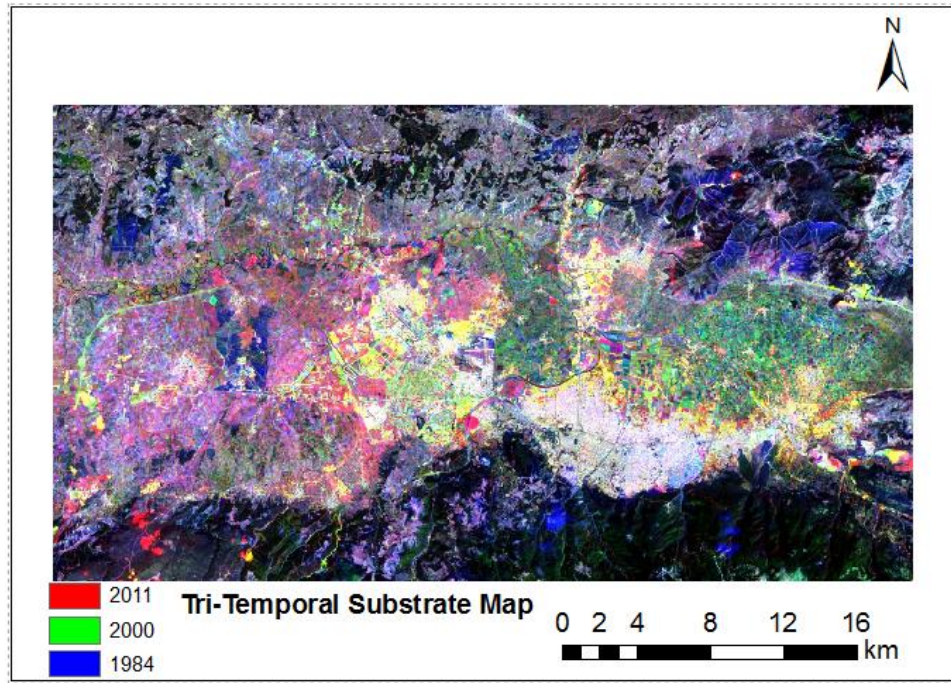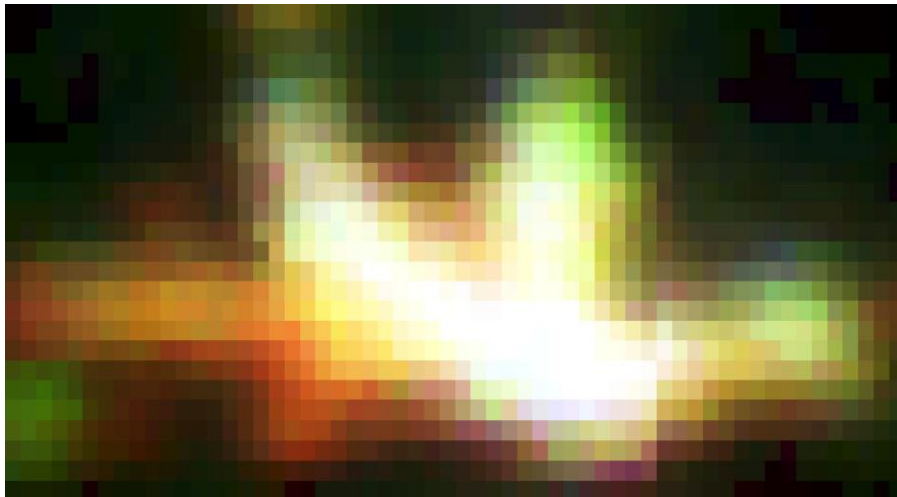SVD models were generated using a linear mixture model. Figures 5.85, 5.86 and 5.87 show the original Landsat images with 30 m spatial resolution for the selected years, with RGB layers matched to 7-4-2 bands respectively. Figures 5.88, 5.89 and 5.90 show substrate fractions for the selected years. These fraction maps has revealed that the organized industrial site has expanded in the west of the city since 1987. Figures 5.91, 5.92 and 5.93 show SVD models for the same years. There has been high substrate albedo in the study area like in Ankara study area. Therefore, DSVD maps with respect to the study area have been analysed.
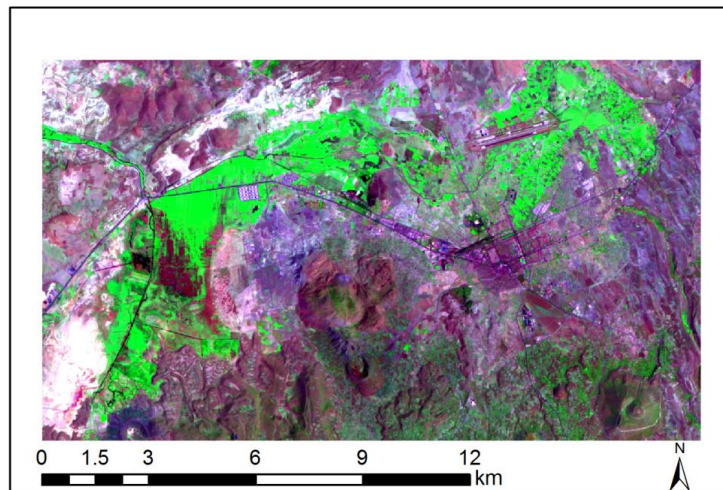
Figure 5.85 : Landsat TM image (20.07.1987).
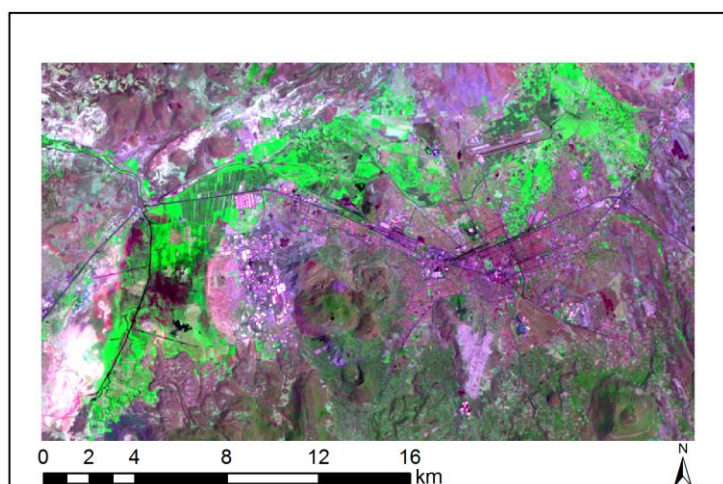
Figure 5.86 : Landsat TM image (18.07.1998).

80
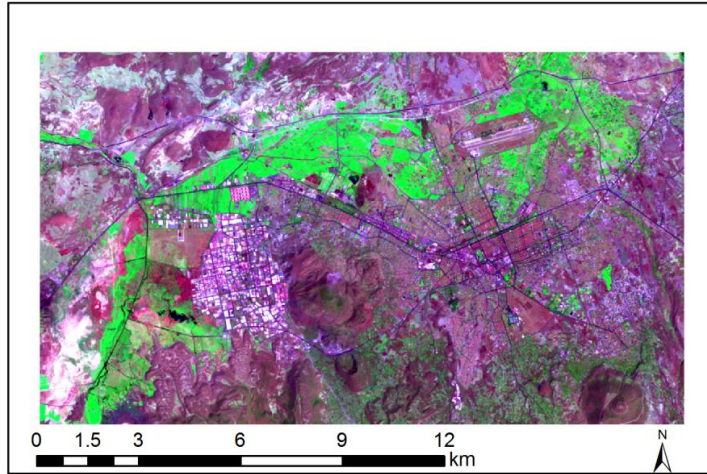
Figure 5.87 : Landsat TM image (04.08.2010).

1987 Substrate Fraction Map
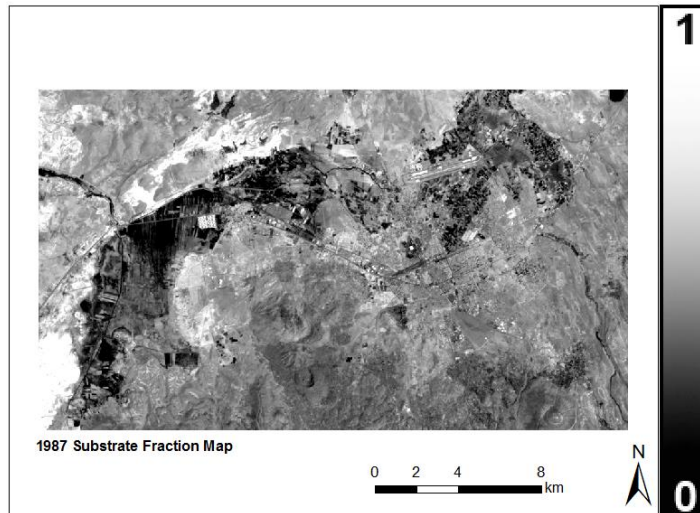
Figure 5.88 : Substrate fraction map of Kayseri (1987).

1998 Substrate Fraction Map
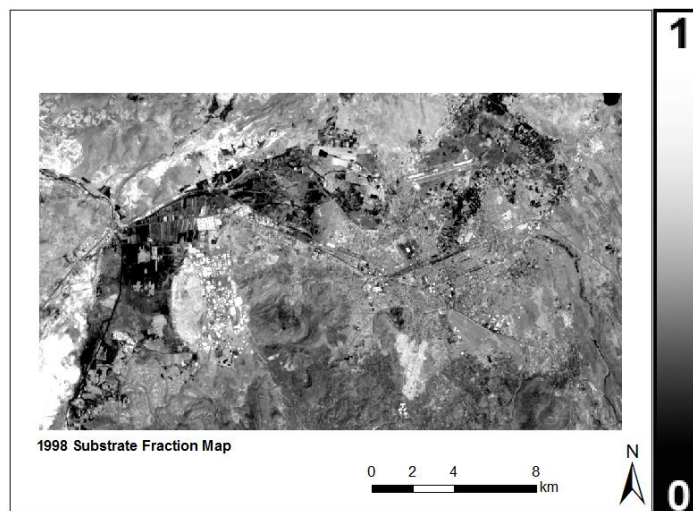
Figure 5.89 : Substrate fraction map of Kayseri (1998).
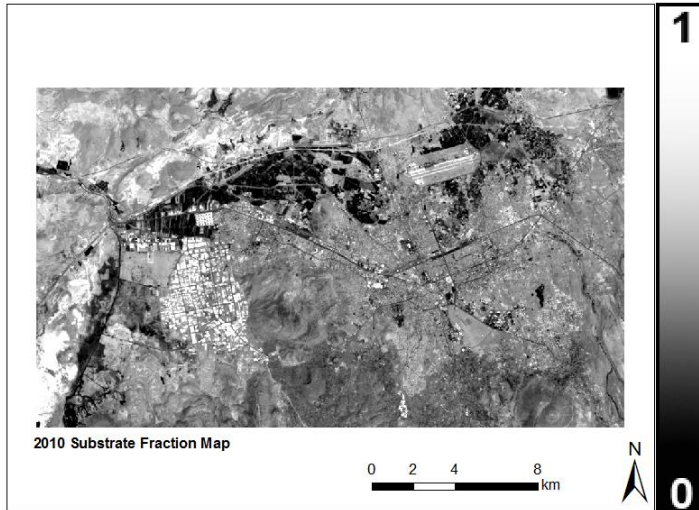
Figure 5.90 : Substrate fraction map of Kayseri (2010).
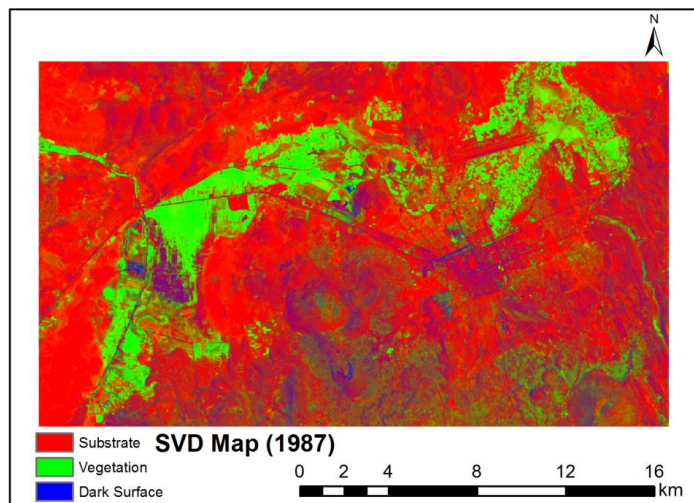
Figure 5.91 : SVD map of Kayseri (1987).
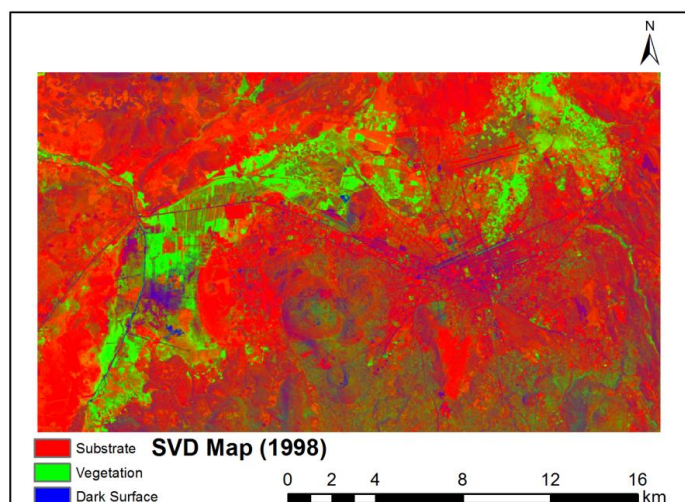
Figure 5.92 : SVD map of Kayseri (1998).
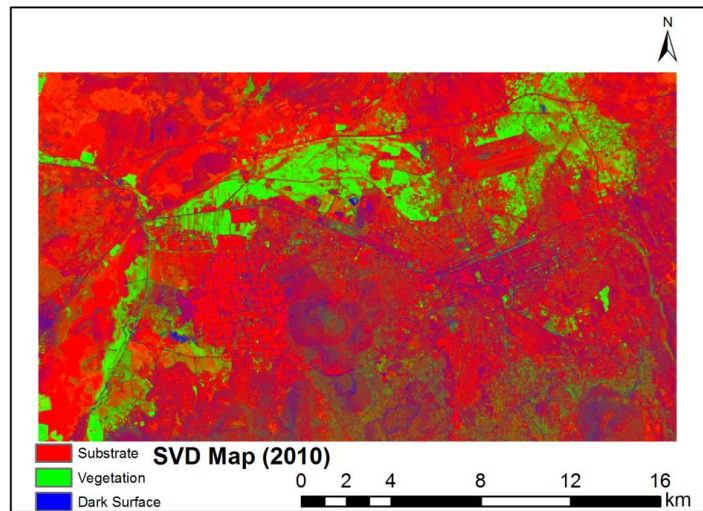
Figure 5.93 : SVD map of Kayseri (2010).

Figure 5.94 shows the SVD differences between 1998 and 1987. According to this map, some areas, where the organized industrial site has been in the west of the city, have as urban growth areas have increased in the west related to commercial activities. Also, new settlement areas in the south of the city has been detected. Figure 5.95 has shown the differences between 2010 and 1998 and this map has shown that there have been increasing some urban areas showing magenta (increased S+D) post 1998 especially in west side of the city.
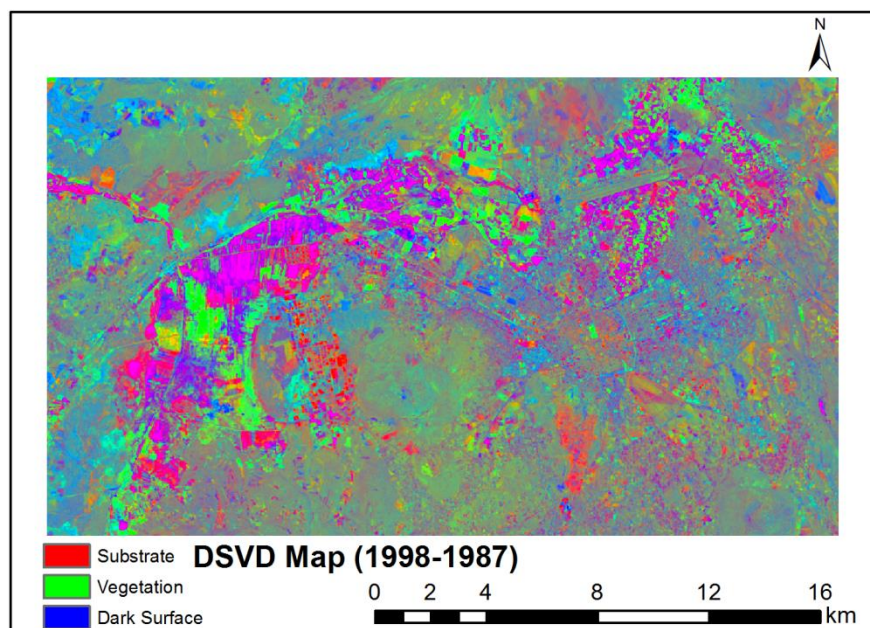
Figure 5.94 : DSVD map (1998-1987).
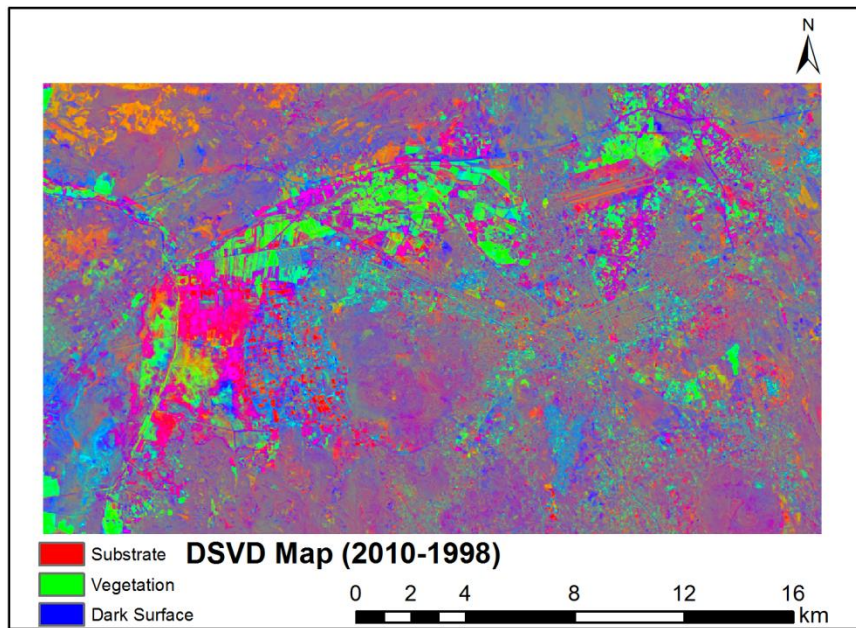
Figure 5.95 : DSVD map (2010-1998).
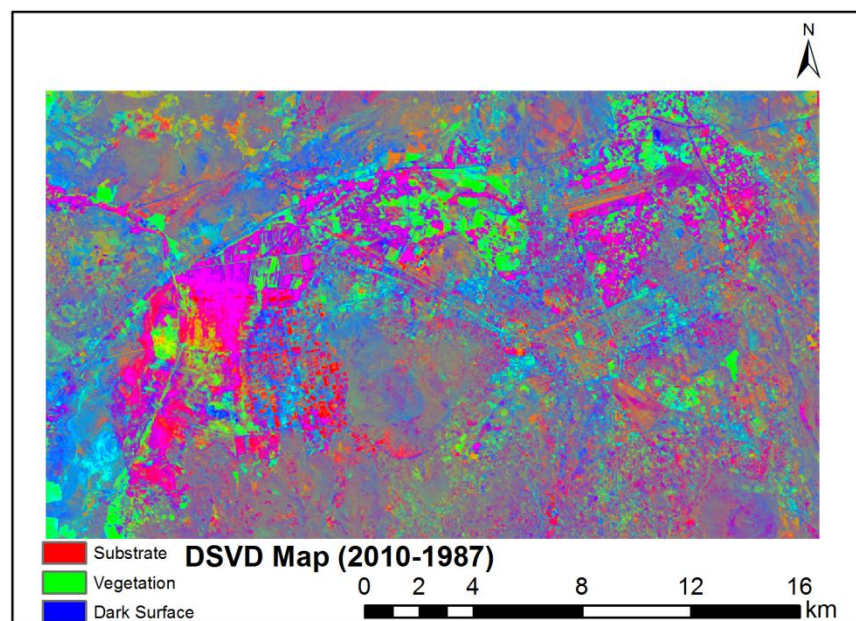
Figure 5.96 : DSVD map (2010-1987).

The SVD maps have not given enough information about urban growth and LCLU changes in the study area due to high substrate albedo. However, using tri-temporal substrate maps, which consist of only substrate layers for the selected years, has provided that new urban growth areas have been in the west and east limitedly (Figure 5.97). Also, the nightlight data and tri-temporal substrate maps have brought out similar results for the urban growth regions. However, SMA has indicated that there

has not been densely urban growth especially in the city center and surrounding of it (Figure 5.98).
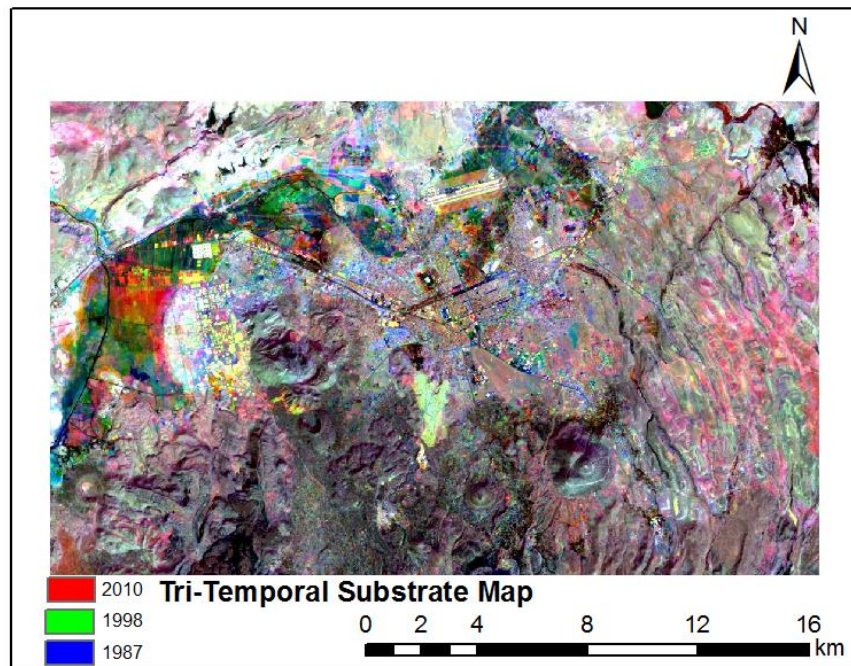
Figure 5.97 : Tri-temporal substrate map of Kayseri.
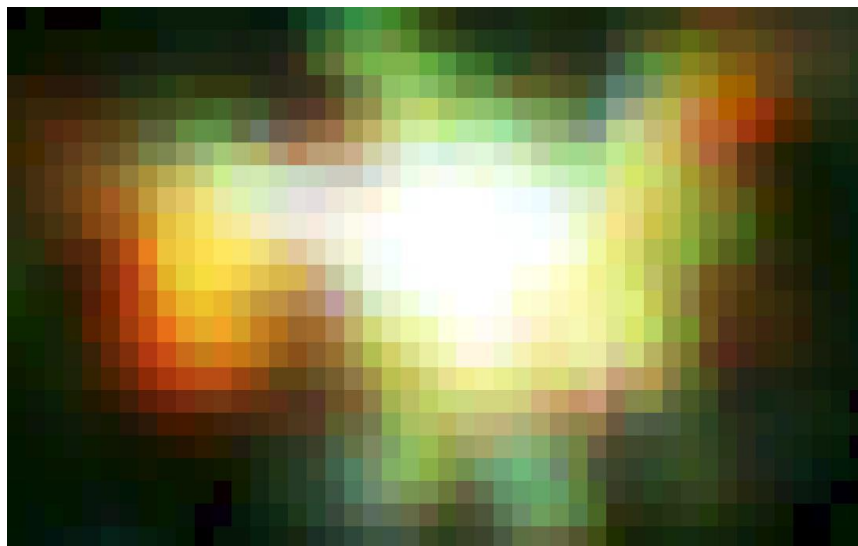
Figure 5.98 : Nighttime DMSP image for Kayseri (1992(B), 1999(G), 2009(R)).

Izmir

Figures 5.99, 5.100 and 5.101 have shown Landsat false color and SVD linear mixture model was applied to these calibrated images (Figures 5.105, 5.106 and 5.107). Substrate fraction maps have been generated for the selected years (Figures 5.102, 5. 103 and 5.104). The SVD maps were generated using the global endmembers. DSVD fraction maps were acquired by taking the differences of SVD values from the selected years. These maps have shown the changes in -S-, -V- and -D- values (Figures 5.108, 5.109 and 5.110).
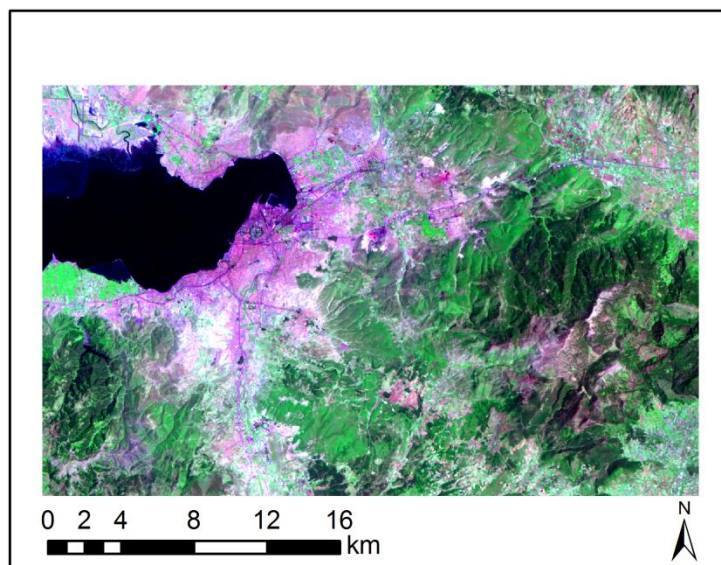
Figure 5.99 : Landsat TM map (12.06.1984).

Figure 5.100 : Landsat ETM map (16.06.2000).
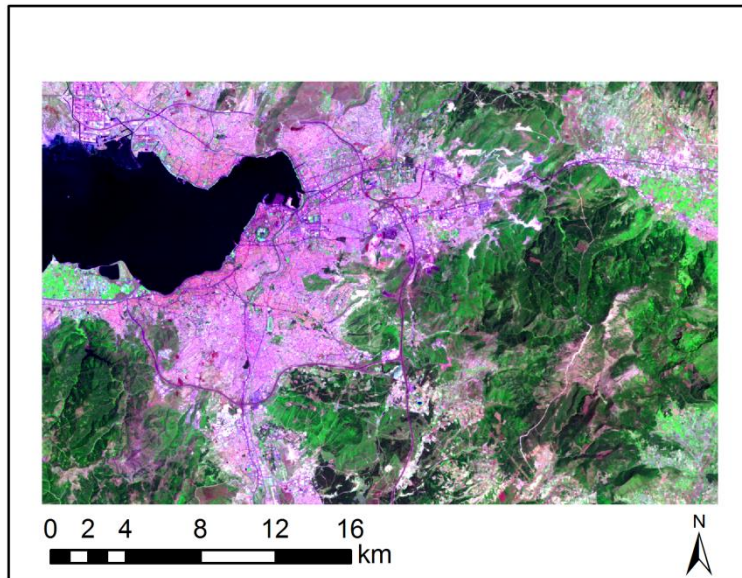
Figure 5.101 : Landsat TM map (17.06.2009).
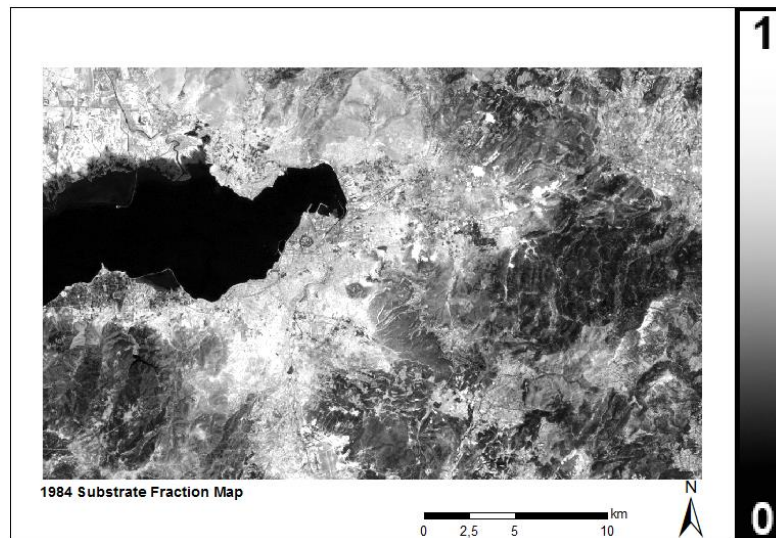
Figure 5.102 : Substrate fraction map of Izmir (1984).

Figure 5.103 : Substrate fraction map of Izmir (2000).

Figure 5.104 : Substrate fraction map of Izmir (2009).

SVD maps has shown that substrate areas were increased considerably between 1984 and 2000. Increase of urban growth areas towards to east of the city has resulted in S values between 1984 and 2000. Also, some mining areas in which have been mostly in Bornova district have caused to expansion of substrate values. In addition, vegetation values were decreased between 1984 and 2000 because of expansion of urban areas.
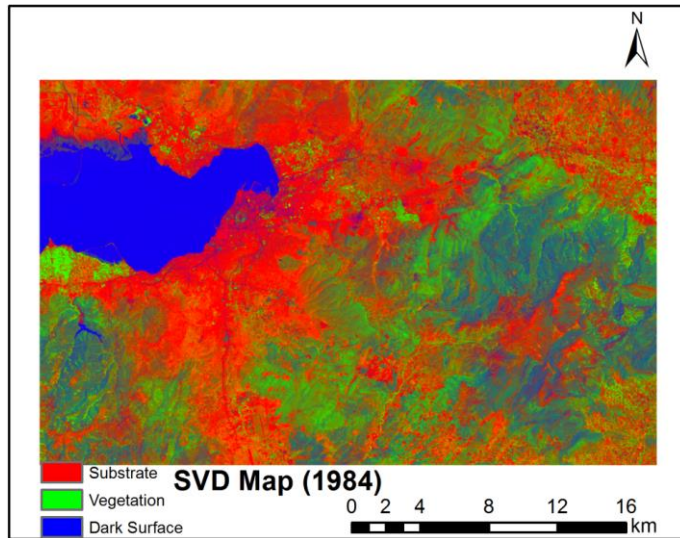
Figure 5.105 : SVD map of Izmir (1984).
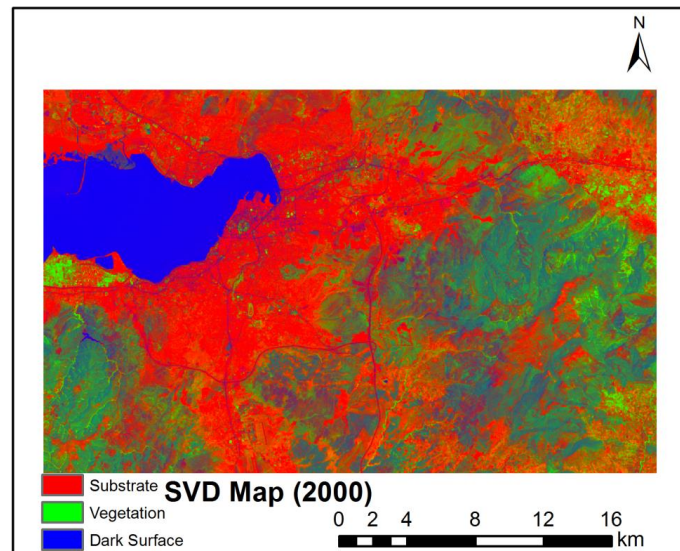
Figure 5.106 : SVD map of Izmir (2000).
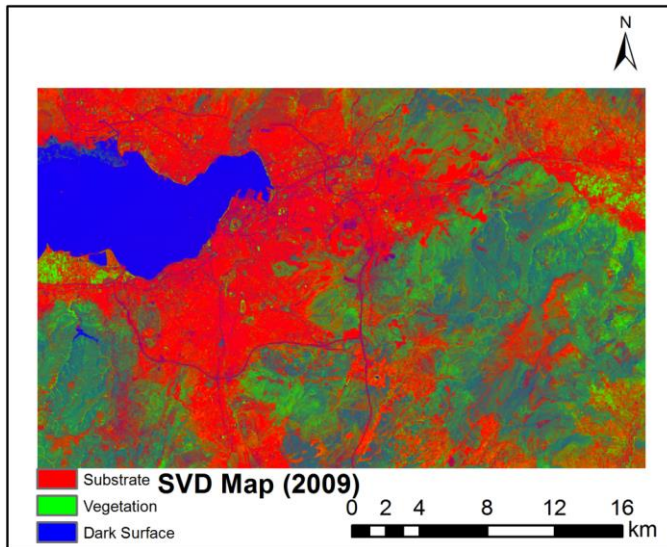
Figure 5.107 : SVD map of Izmir (2009).

DSVD maps in Figures 5.108, 5.109 and 5.110 have revealed not only new urban areas but also other land cover changes. According to this map, changes related to the coastline has been determined and also new breakwaters and port constructions have been detected in the Gulf of Izmir. DSVD maps also have indicated that S areas have increased in and surrounding of Kemalpasa district. This axis covers an important industrial region along the highways and agricultural areas have been changed to industrial areas in this region. This situation has caused to urbanization and other LCLU changes for outside of the city (Ozen et al., 2014).
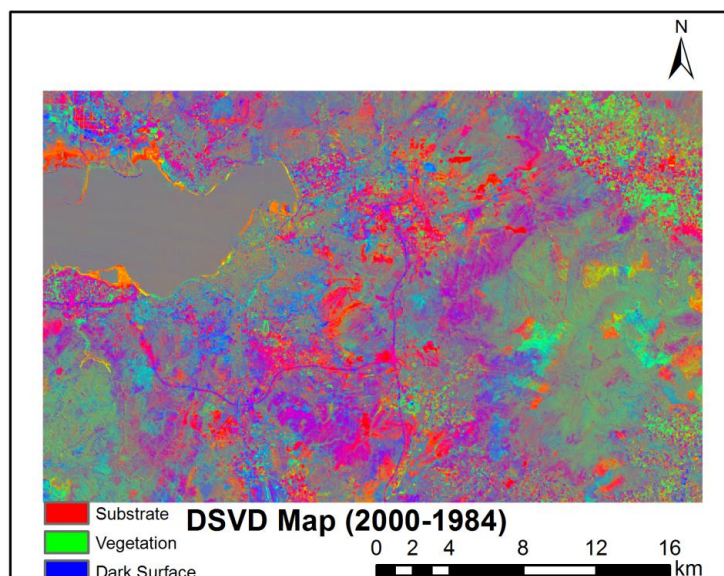
Figure 5.108 : DSVD map (2000-1984).
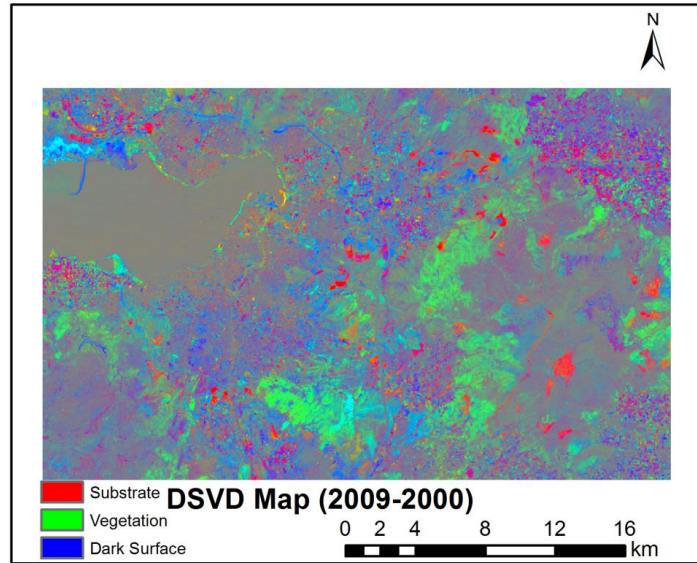
Figure 5.109 : DSVD map (2009-2000).
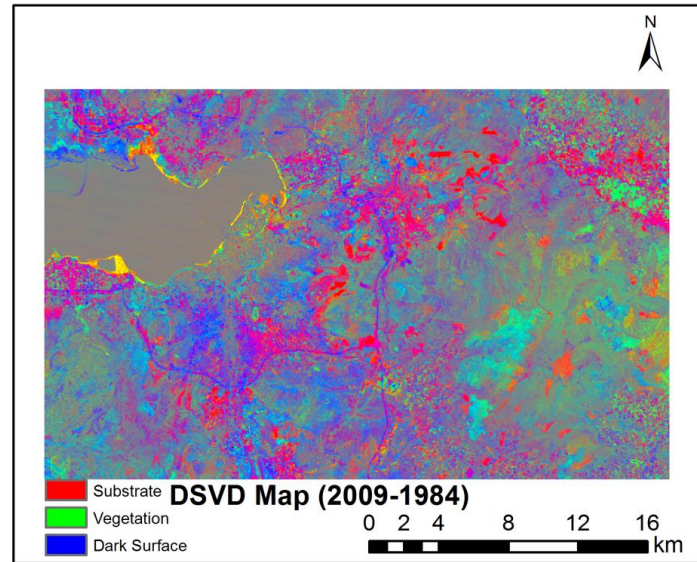
Figure 5.110 : DSVD map (2009-1984).

DSVD maps and tri-temporal substrate map have indicated that the city has grown towards to east along the highways which pass through Bornova and Kemalpaşa districts (Figure 5.111). In the north of the city, Karsiyaka, Cigli and Bayrakli districts are the other growth areas. The other urban growth axis has been in the south of the city and this region has covered districts such as Balcova, Narlidere and Buca. Gaziemir is the other growing region due to the fact that Adnan Menderes Airport has been in this district. The DMSP-OLS image related to Izmir has shown that growing regions have been especially in the east and south of the city (Figure 5.112).
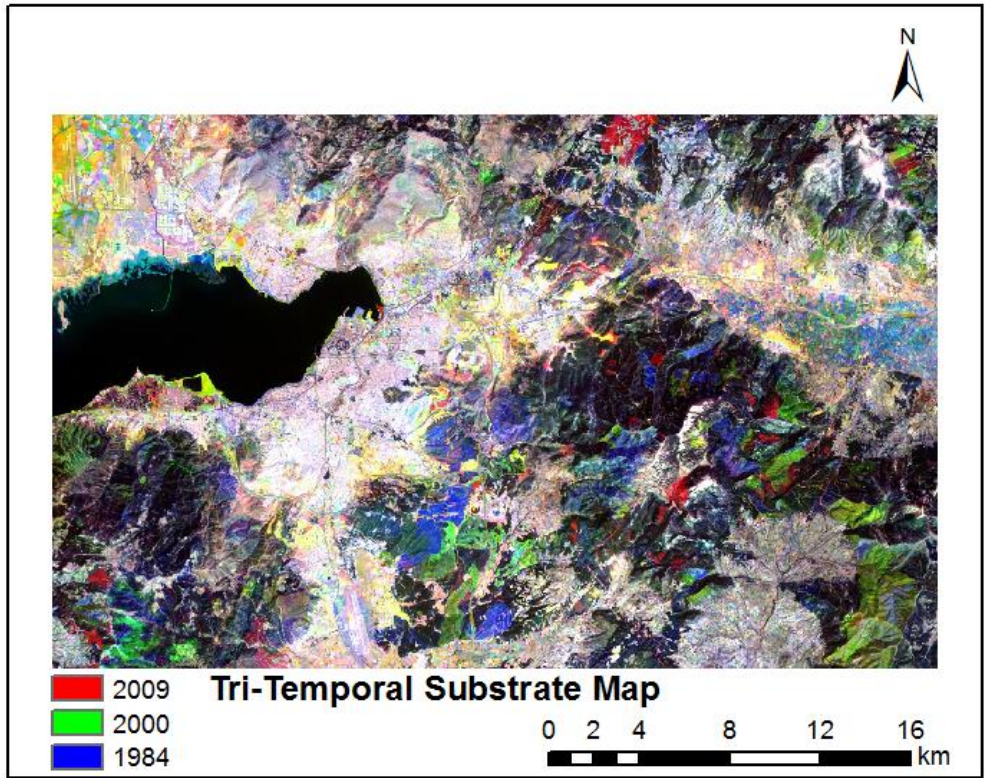
Figure 5.111 : Tri-temporal substrate map of Izmir.
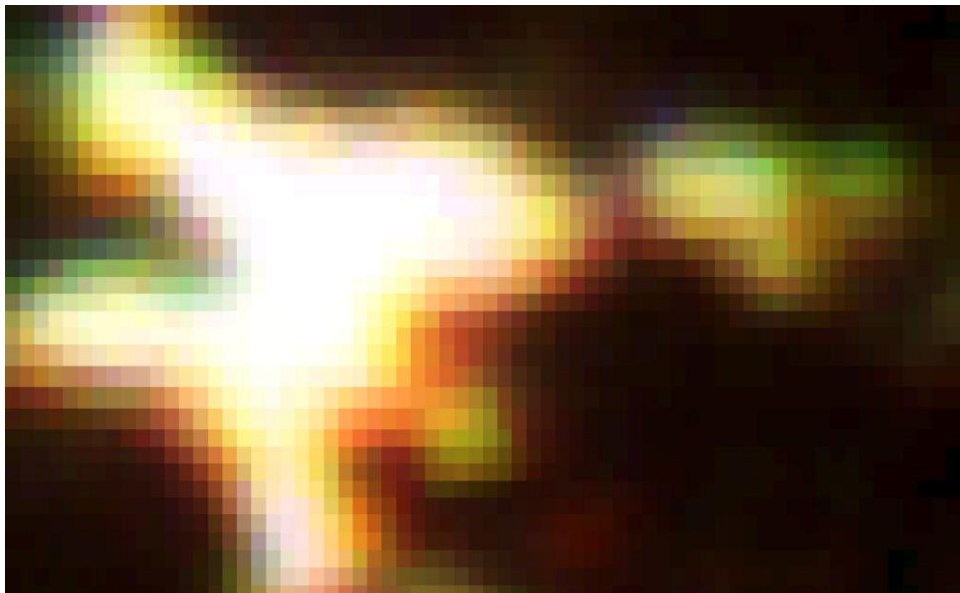
Figure 5.112 : Night-time DMSP image for Izmir (1992(B), 1999(G), 2009(R)).

Manisa

As Manisa and Izmir cities have been same Landsat path/row, Landsat data sets were selected same with Izmir which were acquired by 1984, 2000 and 2009. These Landsat images were then calibrated using their parameters in their filenames. After these processes, SVD models were generated using a linear mixture model. Figures 5.113, 5.114 and 5.115 show the original Landsat images with 30 m spatial resolution for the selected years, with RGB layers matched to 7-4-2 bands respectively. Figures 5.116, 5.117 and 5.118 show substrate fraction images for the selected years. Figures 5.119, 5.120 and 5.121 show SVD models for the same years.
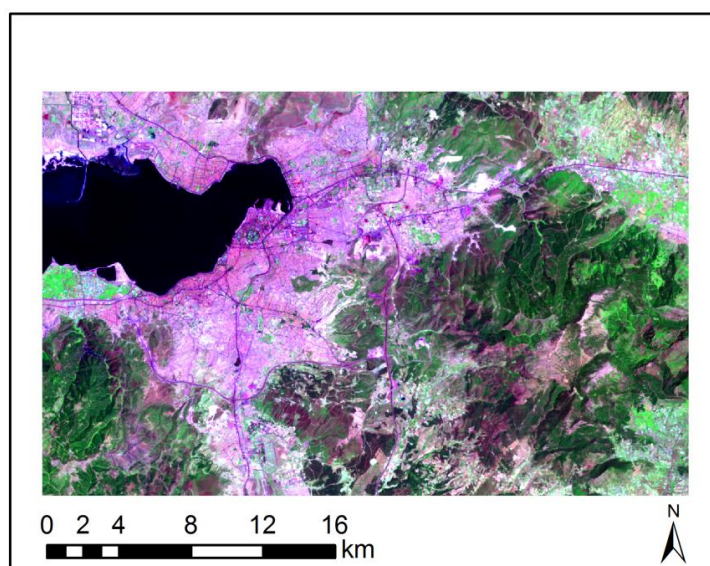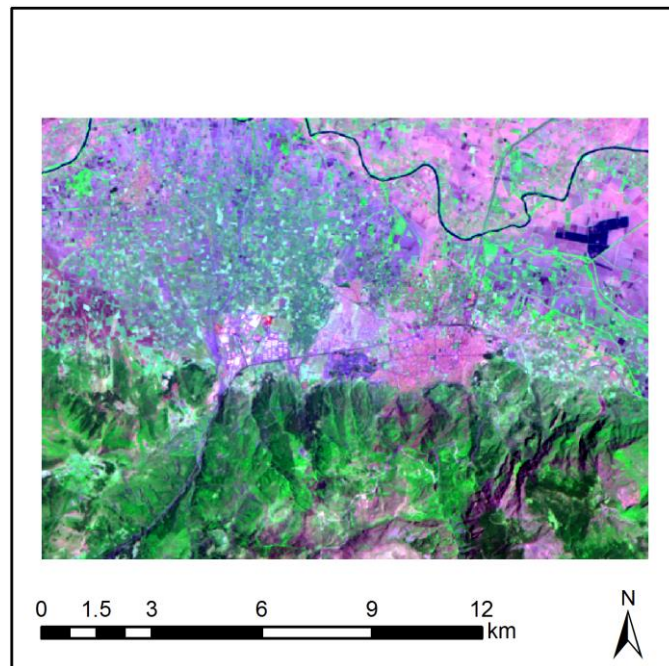

Figure 5.113 : Landsat TM map (12.06.1984).
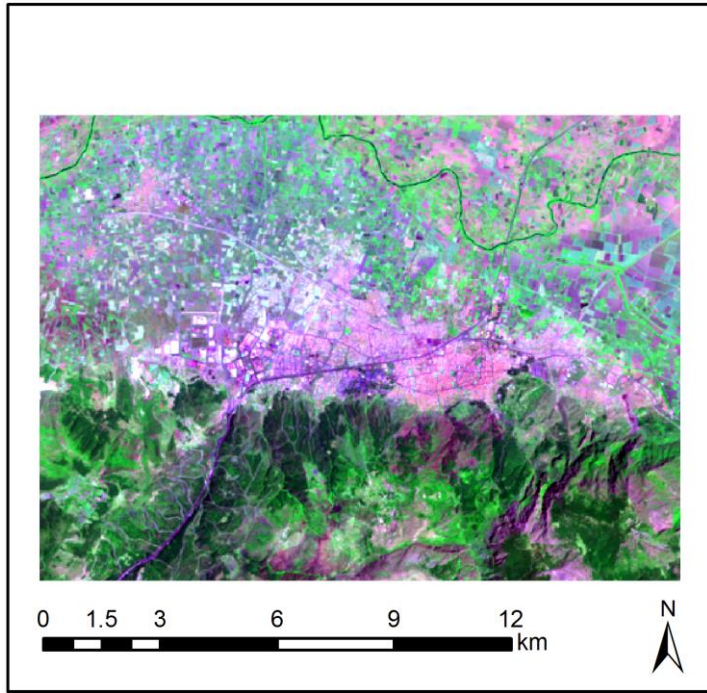
**Figure 5.114 :** Landsat ETM map (16.06.2000).
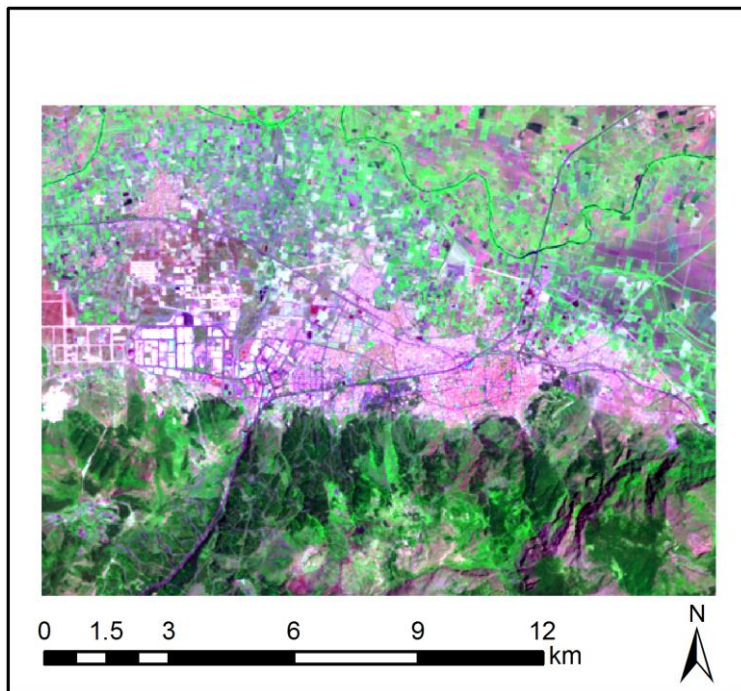

Figure 5.115 : Landsat TM map (17.06.2009).
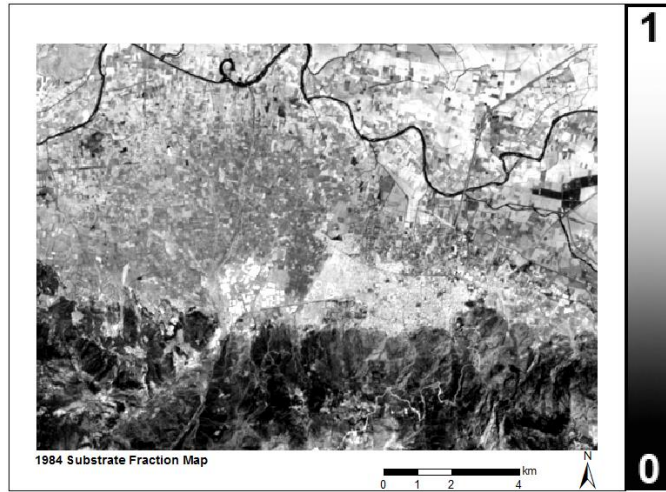
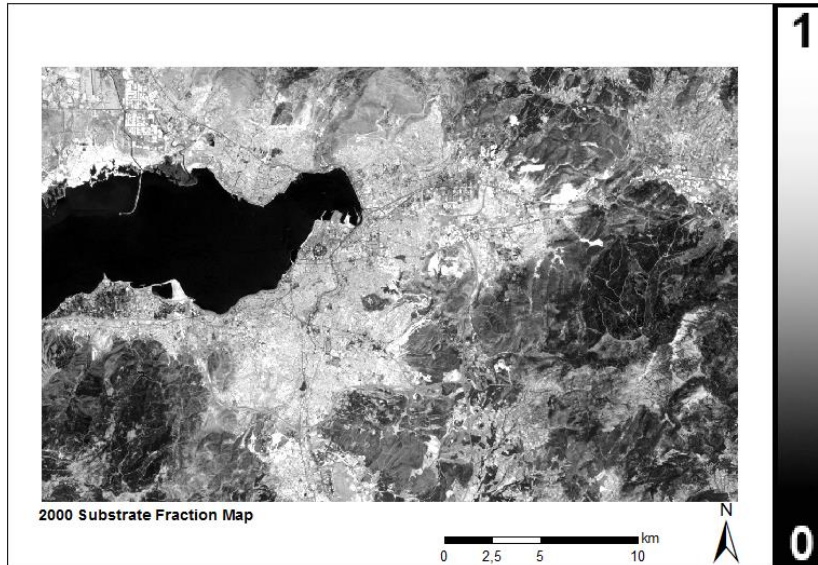**Figure 5.116 :** Substrate fraction map of Manisa (1984).
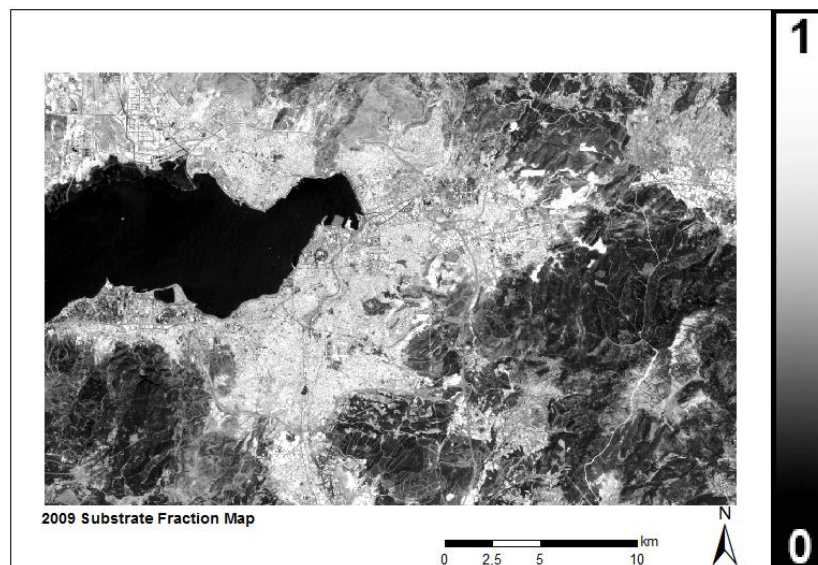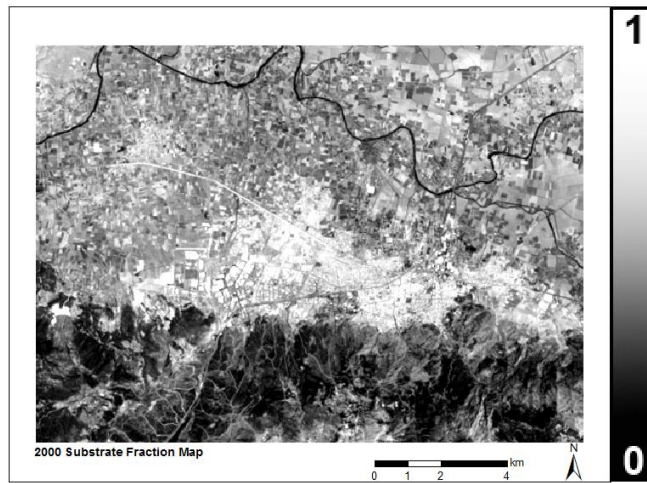

Figure 5.117 : Substrate fraction map of Manisa (2000).
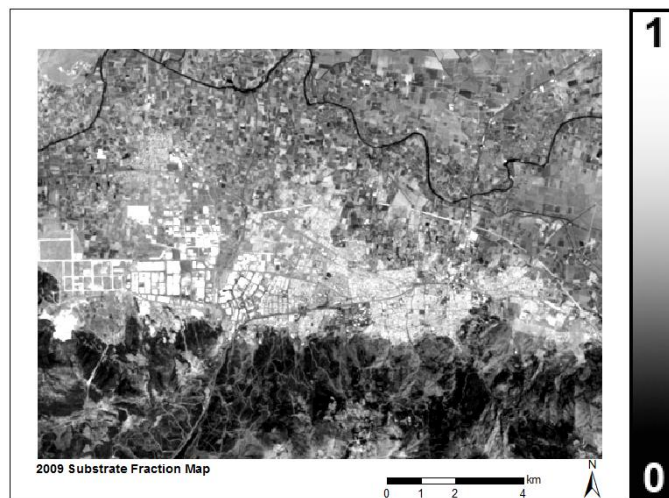
Figure 5.118 : Substrate fraction map of Manisa (2009).

According to SVD maps, substrate areas have increased since 1984. Figure 5.122 shows that substrate areas have increased especially west of the city due to organized industrial site. Also, there has been considerable increase towards to east side of the city. DSVD maps verifiy that the industrial region has increased dramatically after 2000 (Figure 5.123). Manisa is one of the cities showing industrial development and urban growth rapidly in Turkey (Gulersoy, 2013).
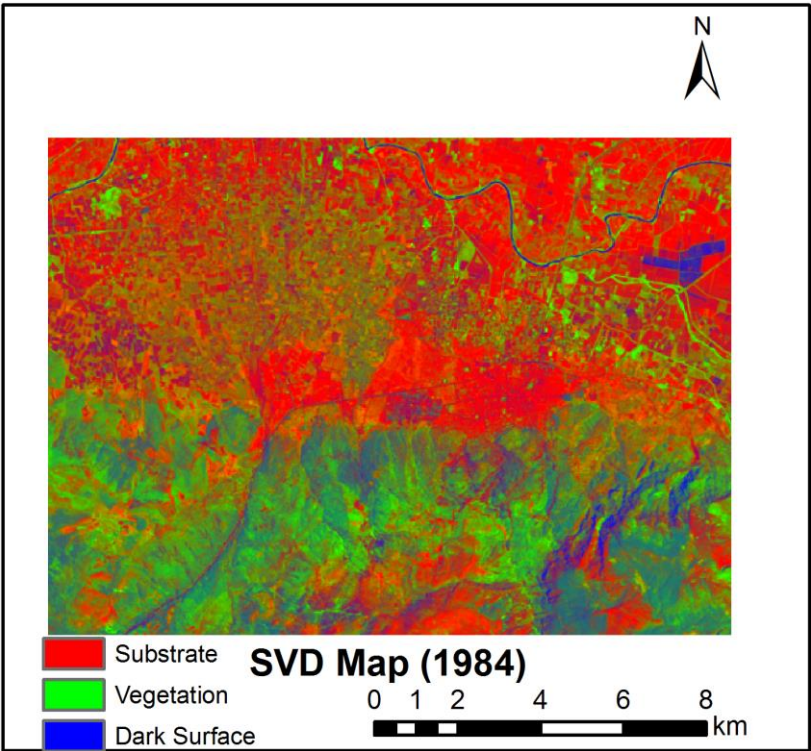
Figure 5.119 : SVD map of Manisa (1984).
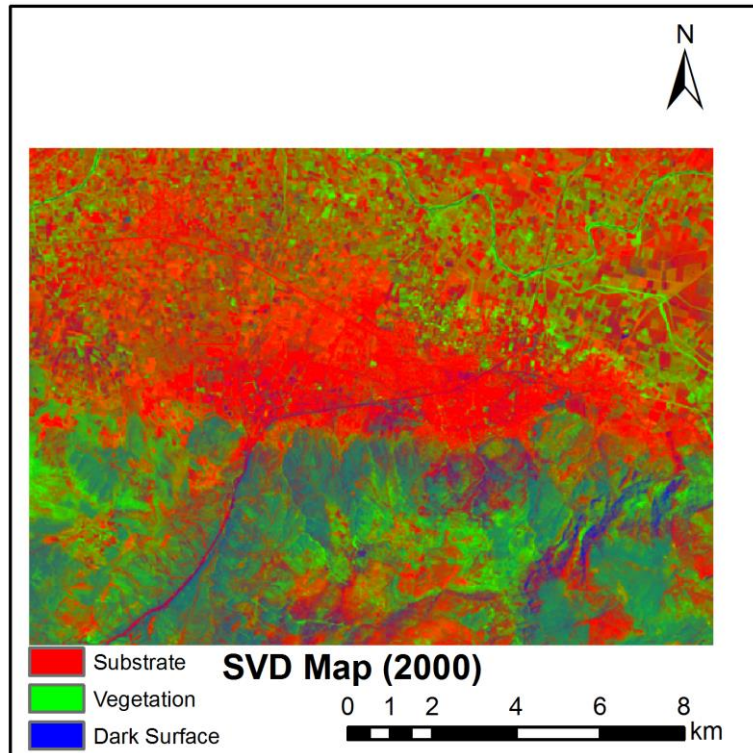
Figure 5.120 : SVD map of Manisa (2000).
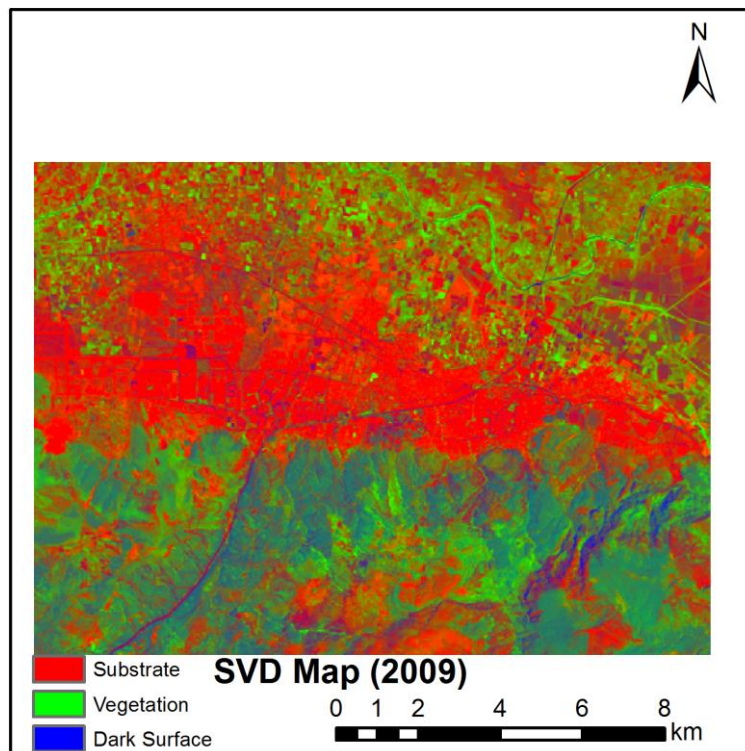
Figure 5.121 : SVD map of Manisa (2009).
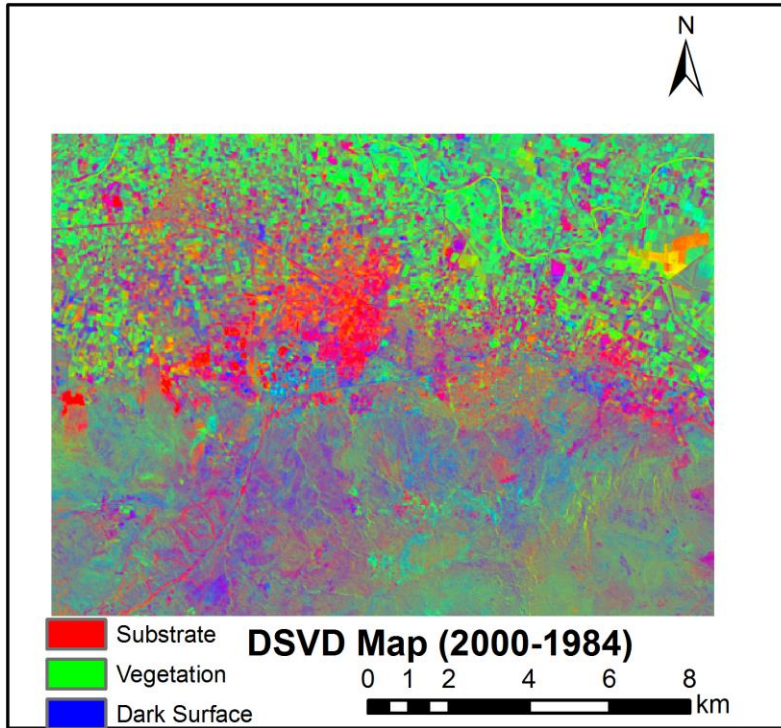
Figure 5.122 : DSVD map (2000-1984).
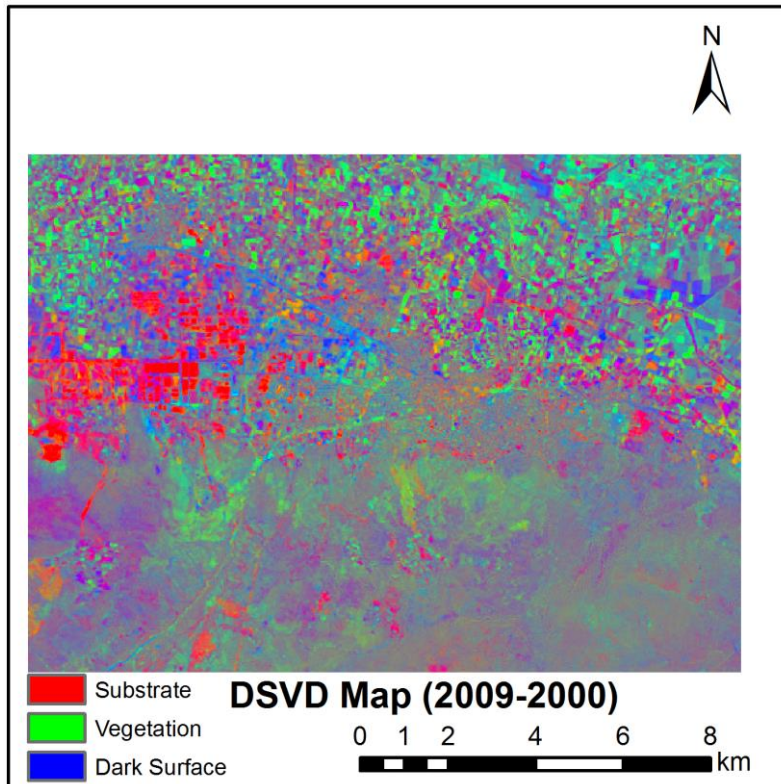
Figure 5.123 : DSVD map (2009-2000).
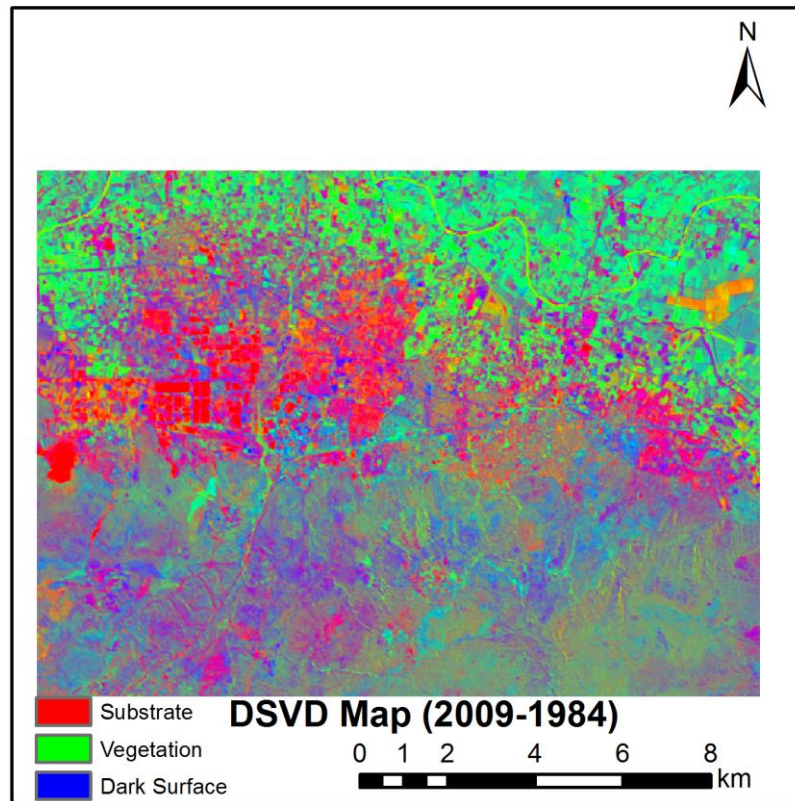
Figure 5.124 : DSVD map (2009-1984).

Apart from the DSVD maps, tri-temporal substrate maps that shows substrate changes using only the S layers were also generated (Figure 5.125). According to this map, regions in which urbanization increased after 1984 have spread towards west of the city across the highway which goes to Izmir. Also, DMSP-OLS image verifies the SMA results and they have indicated parallel results with respect to urban growth direction in Manisa (Figure 5.126).
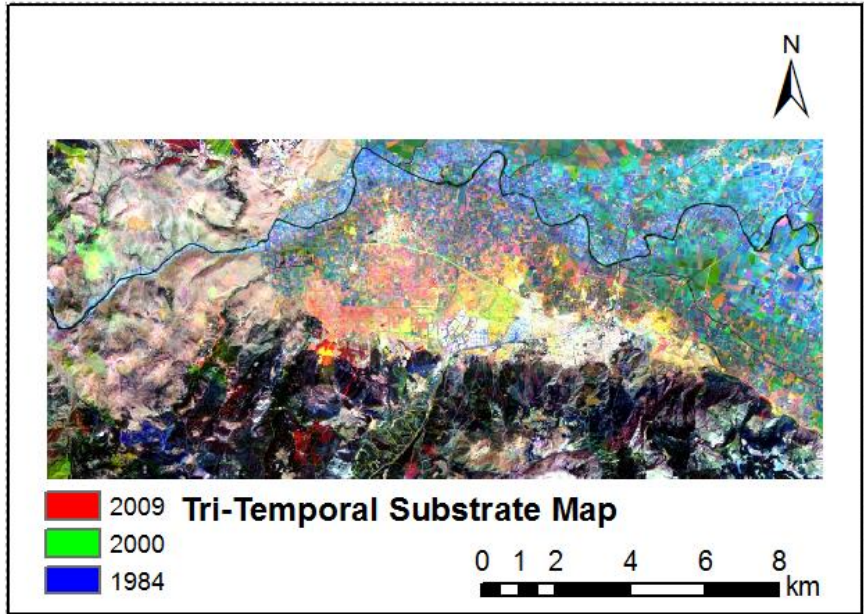
Figure 5.125 : Tri-temporal substrate map of Manisa.
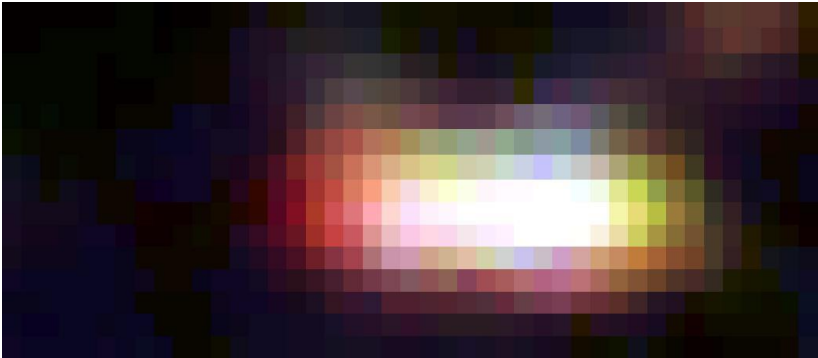
Figure 5.126 : Night-time DMSP image for Manisa (1992(B), 1999(G), 2009(R)).

5.6 Validation

In this study, vicarous validation has been applied to Istanbul which is one of the fastest growing cities in Europe and is the most densely populated city of Turkey. As there have not been enough high resolution images related to selected years for the other study areas, vicarous validation has not been applied to them. According to DSVD maps, new urban growth areas after 2000 Basaksehir, Avcilar, Esenyurt, Beylikduzu and Arnavutkoy were determined on the European side of the city (Figure 5.128). To provide accuracy of these results, high resolution Google Earth images of 2002 and 2011 were used and tested in districts of Basaksehir, Avcilar, Esenyurt (Figure 5.127).

These test areas showed that both results have strong correlation and these results are verified image pairs with high spatial resolution acquired in 2002 and 2011.
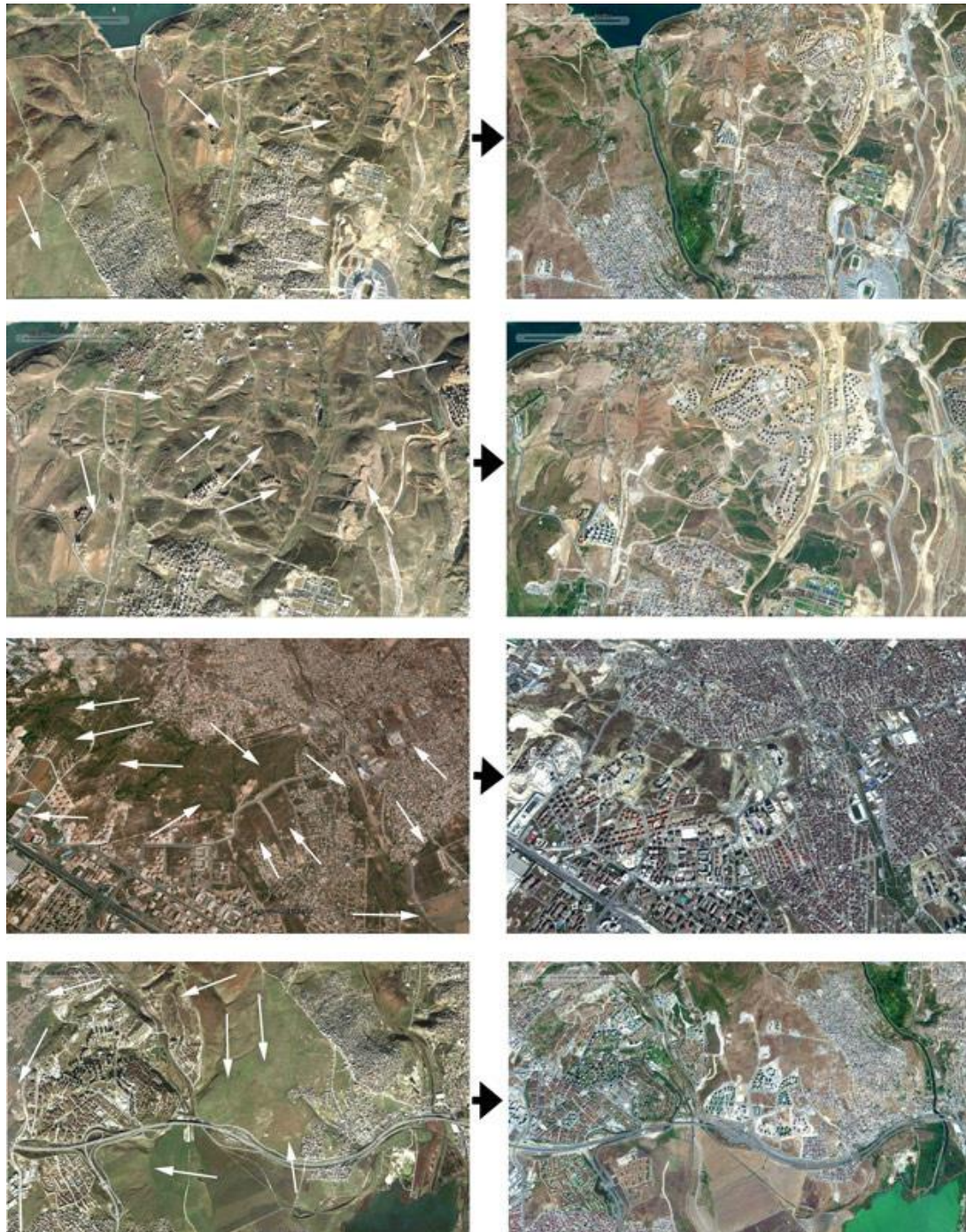
Figure 5.127 : The high resolution images taken from Google Earth show urban growth between 2002 and 2011 on the Europen side of the city. The images have been named as a, b, c and d from the top to bottom. While a and b show urban growth in Basaksehir district, urban growth changes in Esenyurt and Avcilar districts have been showed as c and d respectively in Figures 5.127 and 5.128.
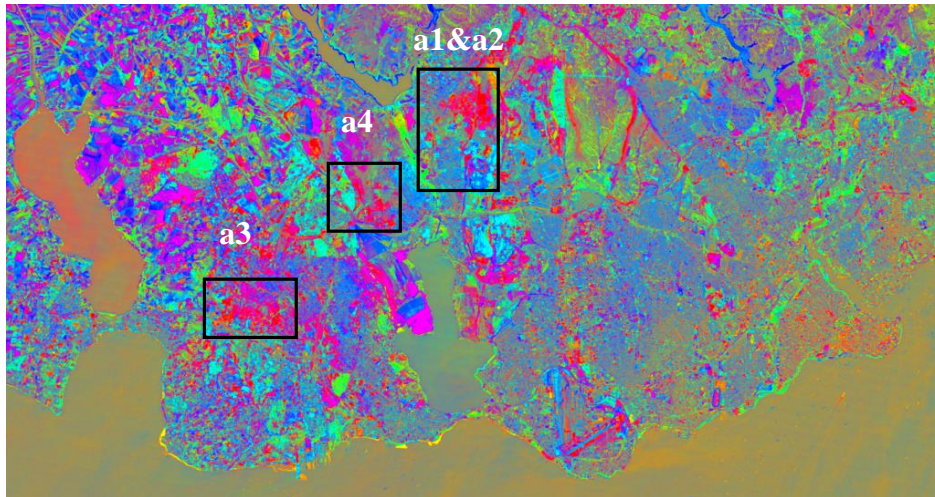
Figure 5.128 : The base map shows change areas where there has been conspicuous increases in both Substrate & Dark fractions on the DSVD maps between 2000 and 2011 years for the European side of the city.

Accuracy Assessment for urban areas in Istanbul has been applied in the study. 50 random points were created over the substrate fraction image using ArcMap 10.1 software (Figure 5.129). As a reference map, Google Earth images, which have high spatial resolution, have been used in the accuracy assessment (Figure 5.130). There have not been enough high resolution images in 2000 therefore, Google Earth images, which are 2001 and 2000 images, have been used to check new urban areas in Istanbul. Accuracy assessment was calculated as 90 % for the urban test area (Table 5.2).
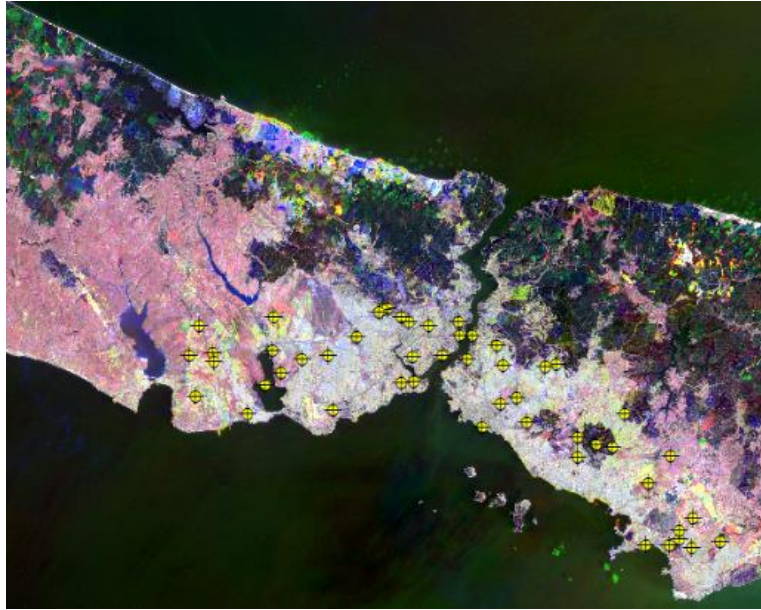
Figure 5.129 : Result map of urban change areas (substrate map).

Figure 5.130 : Reference map (Google Earth).

Table 5.2 : Accuracy Assessment.

points	Result Map	Reference map	points	Result Map	Reference map
1	U	U	26	U	U
2	U	U	27	U	U
3	U	U	28	U	U
4	U	U	29	U	U
5	U	U	30	U	U
6	U	U	31	U	U
7	U	NU	32	U	NU
8	U	U	33	U	U
9	U	U	34	U	U
10	U	U	35	U	NU
11	U	U	36	U	U
12	U	U	37	U	U
13	U	U	38	U	U
14	U	U	39	U	NU
15	U	U	40	U	U
16	U	U	41	U	U
17	U	U	42	U	U
18	U	U	43	U	U
19	U	U	44	U	U
20	U	U	45	U	NU
21	U	U	46	U	U
22	U	U	47	U	U
23	U	U	48	U	U
24	U	U	49	U	U
25	U	U	50	U	U
		Overall accuracy (%) = 90		U: Urban, NU: Non-Urban	

6. CONCLUSIONS AND RECOMMENDATIONS

Using the SMA method which is applied to determine the spatial and temporal changes in LCLU. In this study, urban growth was determined by monitoring and analyzing the different LCLU changes that occur in developed or developing cities of Turkey by applying SMA method to LANDSAT images usually from 1984, 2000 and 2011. The results showed that most of the cities entered into a rapid urban growth process from since 1984. Also, unchanged areas and LCLU changes with limited urban growth were detected in some study areas. Apart from urban growth, changes in areas covered with water and in mining areas were also observed. Thanks to the rapid applicability provided by this method, this was determined to be a suitable method to determine the changes in land use in other cities using the global endmember values. This method also can be used in many disaster monitoring and management applications.

Also, SMA method is not only limited to the horizontal urban growth different from other standard classification methods, but it may also provide useful information regarding the vertical urban growth. In this study, in inner parts in densely populated districts of cities especially in Istanbul, it is observed that S value decreases and D value increases when SVD maps from 1984 to 2011 are examined. This shows that the city reached a built-up position and that there are more complex pixels on the image. Also, dark surface fraction maps have supported that Istanbul has reached a built-up position and the city has grown vertically since 2000. For cities in such situation, it is only possible to talk about vertical growth in the form of inner city. The data approximately belonging to the same period of time and where the atmospheric impact is minimum, should be used to be able to mention such a vertical urban growth. However, such analyses are generally expected to produce trustable results only in well planned cities. In 2013, the digital surface model of Istanbul was obtained using the Lidar technology which will enable precise determination of the vertical growth of the city. Thus, the ability of SMA method to determine the areas where vertical urban growth occur will be revealed in a sounder manner. Detailed studies related to vertical urban growth for some test areas of Istanbul will be done in future studies.

In addition, spectral mixture model is used with integration of nighttime satellite images, they both provide more meaningful results in urban growth analysis. However, nighttime satellite images have provide limited information in small study areas. They should be used in big cities, regional and global applications.

REFERENCES

Adams, J. B., and Smith, M. O. (1986). Spectral Mixture Modeling: A New Analysis of Rock and Soil Types at the Viking Lander 1 Site, *Journal of Geophysical Research*, *91*(8), 8098-8112.

Adams, J., Sabol, V., and Kapos, V. (1995). Classification of multispectral images based on fraction endmembers, application to land cover change in the Brazilian Amazon, *Remote Sensing of Env.*, *52*(2), 137–154.

Adams, J. B., Smith, M. O., and Gillespie, A. R. (1993). *Imaging Spectroscopy: Interpretation based on spectral mixture analysis*, In remote geochemical analysis: elemental and mineralogical composition*,* 145–166. New York, Cambridge University Press.

Al-Bakri, J. T., Duqqah M., and Brewer T. (2013). Application of Remote Sensing and GIS for Modeling and Assessment of Land Use/Cover Change in Amman/Jordan, *Journal of Geographic Information System, 5*(5), 509-519. doi: 10.4236/jgis.2013.55048.

Al-Rawashdeh, S., and Saleh, B. (2006). Satellite Monitoring of Urban Spatial Growth in the Amman Area, Jordan, *Journal of Urban Planning and Development, 132*(4), 211-216. doi: 10.1061/(ASCE)0733-9488 (2006) 132:4(211).

Al-Tamimi S., and Al-Bakri J. T. (2005). Comparison between Supervised and Unsupervised Classifications for Mapping Land Use/Cover in Ajloun Area, *Jordan Journal of Agricultural Sciences, 1*(1), 2005, 73-83. Retrieved from *http://journals.ju.edu.jo/JJAS/article/view/1290.*

Atkinson, P., Cutler, M., and Lewis, H. (1997). Mapping subpixel proportional land cover with AVHRR imagery, *International Journal of Remote Sensing*, *18*(4), 917–935.

Aydoner C. (2005). Analysis of Land cover/Land use with Integration of Satellite Data and Ground Data after Earthquake, *PhD Thesis*, Istanbul Technical University, Istanbul.

Balaselvakumar, S., and Saravanan, S. (2006). Remote Sensing Techniques for Agriculture Survey. Retrieved from *http://www.gisdevelopment.net/ application/agriculture/overview/agrio014.htm.*

Batty M., and Howes D. (2001). *Predicting temporal patterns in urban development from remote imagery.* In: Donnay J. P, Barnsley M. J, Longley P .A (eds). Remote sensing and urban analysis, Taylor and Francis, London, 185–204.

Berni, J. A. J., Zarco-Tejada, P. J., Suárez, L,. and Fereres, E. (2009). Thermal and Narrowband Multispectral Remote Sensing for Vegetation Monitoring From an Unmanned Aerial Vehicle, *IEEE Transactions on Geoscience and Remote Sensing, 47*(3), 722-738.

Bernstein, R., and Ferneyhough, D. G. (1975). Digital image processing: *Photogrammetric Engineering, 41,* 1465-1476.

Boardman, J. W. (1993). *Automating spectral unmixing of AVIRIS data using convex geometry concepts*. In R. O. Green (Ed.), Fourth Airborne Visible/Infrared Imaging Spectrometer (AVIRIS) airborne geosciences workshop (pp.11-14), Pasadena, CA, Jet Propulsion Laboratory.

Buiten, H. J., and Clevers, J. G. P. W. (1993). *Land Observation by Remote Sensing Theory and Applications*, OPA Gordon and Breach Science Publishers, pp.10-11.

Campbell J. B. (2007). *Introduction to Remote Sensing*, 4th ed., The Guilford Publications, Inc.

Congress, U. S. (1994). Office of Technology Assessment, Civilian Satellite Remote Sensing: A Strategic Approach. OTA-ISS-607, Washington, DC: US *Government Printing Office*.

CRISP   (Centre for Remote Imaging, Sensing and Processing), (2014). http://www.crisp.nus.edu.sg/~research/tutorial/sar_int.htm> date retrieved 12.04.2014.

Dincer, I., Enlil, Z., Evren, Y., and Som, S. K. (2011). *Istanbul's historical and natural heritage values - Potential , Risks and Protection Issues*, Istanbul: Istanbul Bilgi University Publications, pp.74-75.

Dodgson, N. A. (1992). *Image Resampling*, University of Cambridge, Computer Laboratory, Cambridge.

Doll, C. N. H. (2008). CIESIN Thematic Guide to Night-time Light Remote Sensing and its Applications, Center for International Earth Science Information Network of Columbia University, Palisades, New York. Retrieved from *http://sedac.ciesin.columbia.edu/tg/.*

Donnay, J. P., Barnsley M. J., and Longley P. A. (2001). *Remote sensing and urban analysis.* In: Donnay J. P, Barnsley M. J, Longley P. A (eds), Remote sensing and urban analysis, Taylor & Francis, London, 3–18.

Elvidge, C. D., Bauhg, K. E. Kihn, E. A., Kroehl, H. W., and Davis, E. R. (1997). Mapping city lights with nighttime data from the DMSP Operationsl Linescan System, *Photogrammetric Engineering and Remote Sensing*, *63*(6), 727-734.

Elvidge, C. D., Imhoff., M. L., Baugh, K.E., Hobson, V. R., Nelson., I., Safran, J., Dietz, J. B,. and Tuttle., B. T. (2001). Night-time lights of the world: 1994-1995, *ISPRS Journal of Photogrammetry & Remote Sensing, 56*, 81-99.

ESRI,   (2009). Spatial Analyst: Cell size and resampling in analysis, *ArcGIS Help*.

Extension, (Geospatial Technology), (2014). Retrieved from http://www.extension.org/pages/9628/remote-sensing-resampling methods#.VWBgb9Iiq2w, date retrieved 08.12.2014.

Fichtner, A., Saygin, E., Taymaz, T., Cupillard, P., Capdeville, Y., and Trampert, J. (2013). The deep structure of the North Anatolian Fault Zone. *Earth and Planetary Science Letters*, *373*, 109–117. doi:10.1016/j.epsl.2013.04.027.

Foody, G. M. (1996). Approaches for the production and evaluation of fuzzy land cover classifications from remotely sensed data, *International Journal of Remote Sensing*, *17*, 1317–1340.

Fouquet, M., and Ward, J. (1998). Cost Driven Design of Small Satellite Remote Sensing Systems, *Journal of Reducing Space Mission Cost*, *1*(1), 159–175.

Geymen, A., and Baz, I. (2008). Monitoring urban growth and detecting land-cover changes on the Istanbul metropolitan area, *Environmental Monitoring and Assessment*, *136*, 449–459.

Gillespie, A. R., Smith, M. O., Adams, J. B., Willis, S. C., Fischer, A. F., and Sabol, D. E. (1990). Interpretation of residual images: spectral mixture analysis of AVIRIS images, Owens Valley, California. *Proceedings of the 2nd Airborne Visible/Infrared Imaging Spectrometer (AVIRIS) Workshop*, pp. 243–270, Pasadena, CA: NASA Jet Propulsion Laboratory.

Goldsmith, N. (2014). Resampling Raster Images. Retrieved from *http://www.jiscdigitalmedia.ac.uk/stillimages/advice/resampling raster-images/*, date retrieved 21.04.2014.

Gong, P., and Zhang, A. (1999). Noise Effect on Linear Spectral Unmixing, *The Association of Chinese Professionals in Geographic Information Systems*, *5*(1), 52-57.

Gonzalez, R. C., and Woods, R. E. (2007). *Digital Image Processing*, Prentice Hall.

Google Earth. (11.04.2001, 23.07.2002 and 17.05.2011). Istanbul map. Retrieved from *http://www.google.com/earth/index.html,* date retrieved 15.05.2015.

Gulersoy, A. E. (2013). Farklı Uzaktan Algılama Teknikleri Kullanılarak Arazi Örtüsü/Kullanımında Meydana Gelen Değişimlerin İncelenmesi: Manisa Merkez İlçesi Örneği (1986-2010), *Turkish Studies*, *8*(8), 1915-1934.

Haertel, V. F., and Shimabukuro, Y. E. (2005). Spectral Linear Mixture Model in Low Spatial Resolution Image Data, *IEEE Transactions on Geoscience and Remote Sensing, 43*(11), 2555-2562.

Hall, R. C. (2001). A History of The Military Polar Orbiting Meteorological Satellite Program, *National Reconnaissance Office*, 37 Pages.

Hapke, B. (1981). Bidirectional reflectance spectroscopy 1. Theory, *Journal of Geophysics Research*, *86*, 3039–3054.

Herold M., Roberts D., Gardner M., Dennison P. (2004). Spectrometry for urban area remote sensing-development and analysis of a spectral library from 350 to 2400 nm, *Remote Sensing of Environment, 91*, 304–319.

Huber, W. (2014). Map Algebra: Resampling. Retrieved from *http://www.quantdec.com/SYSEN597/GTKAV/section9/map_algebra.htm,* date retrieved 21.04.2014.

Jensen, J. R. (1996). *Introductory Digital Image Processing: A Remote Sensing Perspective* (second ed.), New Jersey, Prentice Hall.

Jensen J. R., and Cowen D. C. (1999). Remote sensing of urban/suburban infrastructure and socioeconomic attributes, *Photogram. Eng. and Remote Sens., 65*(5), 611–622.

Justice, C., Townshend, J., Vermote, E., Masuoka, E., Wolfe, R., Saleous, N., Roy, D., and Morisette J. T. (2002). An overview of MODIS Land data processing and product status, *Remote Sensing of Environment*, *83*(1-2), 3−15, doi: 10.1016/S0034-4257(02)00084-6.

Kaya, S., and Curran, P. J. (2006). Monitoring urban growth on the European side of the Istanbul metropolitan area: A case study, *International Journal of Applied Earth Observation and Geoinformation., 8*, 18-25.

Keshava, N., and Mustard, J. F. (2002). Spectral unmixing, *IEEE Processing Magazine*, *2*, 44–57.

Kramer, H. J. (1994). *Observation of the Earth and its Environment - Survey of Missions and Sensors*, 2nd ed., Berlin & New York, Springer.

Kuplich, T. M., Freitas, C. C., and Soares, J. V. (2000). The Study of ERS-1 and Landsat TM synergism for land use classification, *International Journal of Remote Sensing*, *21*(10), 2101 − 2111.

Lelong, C. C. D., Pinet, P. C., and Poilve, H. (1998). Hyperspectral Imaging and Stress Mapping in Agriculture: A Case Study on Wheat in Beauce (France), *Remote Sensing of Environ, 66*, 179-191.

Longley P. A., and Mesev V. (2000). On the measurement and generalization of urban form, *Environ. Plan, 32*, 473–488.

Longley P. A., Barnsley M. J., and Donnay J. P. (2001.) *Remote sensing and urban analysis: a research agenda.* In: Donnay J. P, Barnsley M. J, Longley P.A (eds), Remote sensing and urban analysis, Taylor and Francis, London, pp. 245–258.

Lu, D., Morana, E., and Batistella, M. (2003). Linear mixture model applied to Amazonian vegetation classification, *Remote Sensing of. Environ., 87*, 456–469.

Lunetta, R. S. (1998). *Applications, project formulation, and analytical approach*. In Remote Sensing Change Detection: Environmental Monitoring Methods and Applications. In: Lunetta, R. S. and Elvidge, C. D., (eds), 1–19, Taylor & Francis, London.

Maktav, D., and Erbek, F. S. (2005). Analyse of urban growth using multitemporal satellite data in Istanbul, Turkey, *International Journal of Remote Sensing, 26*(4),797–810.

Maktav, D., Erbek, F. S., and Jurgens, C. (2005). Remote sensing of urban areas, *International Journal of Remote Sensing*, *26*(4), 655-659.

Maktav, D., Sunar, F., Taberner, M., and Akgun, H. (2000). Monitoring Urban Expansion in the Buyukcekmece District of Istanbul Using Satellite Data, *ISPRS*, Amsterdam, Holland.

Masek, J. G., Vermote, E. F., Saleous, N. E., Wolfe, R., Hall, F. G., Huemmrich, K. F., Gao, F., Kutler, J., and Lim T. K. (2006). A Landsat surface reflectance dataset for North America, 1990–2000, *IEEE Transactions on Geoscience and Remote Sensing Letters*, *3*, 68−72.

Manolakis, D., Marden, D., and Shaw, G. A. (2003). Hyperspectral Image Processing for Automatic Target Detection Applications, *Lincoln Laboratory Journal*, *14*(1), 79–116.

Moran, M. S., Jackson, R. D., Slater, P. N., and Teillet, P. M. (1992). Evaluation of simplified procedures for retrieval of Landsat surface reflectance factors from satellite sensor output, *Remote Sens. Environ.*, *41*, 169-184.

NRC (Natural Resources Canada), (2014). Retrieved from www.nrcan.gc.ca/files/earthsciences/pdf/resource/tutor/fundam/pdf/fundamentals_e.pdf, date retrieved 05.06.2014.

NASA, GOES Project Science, (2015). *http://goes.gsfc.nasa.gov/*, date retrieved 22.02.2015.

NASA, Landsat Science, (2015). *http://landsat.gsfc.nasa.gov/?p=5112*, date retrieved 16.03.2015.

Navulur, K. (2007). Multispectral Image Analysis Using the Object-Oriented Paradigm, *Taylor & Francis Group*.

NOAA (National Oceanic and Atmospheric Administration), 2014. *http://www.nesdis.noaa.gov/index.html*, date retrieved 20.08.2014.

Ozen F., Esetlili M. T., Bolca M., and Kurucu Y. (2014). Impact of Land Use Changes on Agricultural Ecosystem: A Case Study of Kemalpasa-Izmir, *Journal of Environmental Protection and Ecology ,15*(4),1801–1809.

Palanisamy, S., Yu-Hwan, A., and Shanmugam, S. (2006). A comparison of the classification of wetland characteristics by linear spectral mixture modelling and traditional hard classifiers on multispectral remotely sensed imagery in southern India, *ecological modelling*, *194*, 379–394.

Parker, D. C., Manson S. M., Janssen M. A., Hoffmann M. J., and Deadman P. (2003). Multi-agent systems for the simulation of land-use and land-cover change: a review, *Annual Assoc. Amer. Geograph 93*(2), 314–337.

Pons, X., Pesquer, L., Cristóbal, J., and González-Guerrero, O. (2014). Automatic and improved radiometric correction of landsat imagery using reference values from MODIS surface reflectance images, *International Journal of Applied Earth Observation and Geoinformation*, *33*(1), 243–254. doi:10.1016/j.jag.2014.06.002.

Price, J. C. (1997). Spectral band selection for visible-near infrared remote sensing: Spectral-spatial resolution tradeoffs, *IEEE Transactions on Geoscience and Remote Sensing, 35*(5), 1277 – 1285.

Quarmby, N., Townshend J., Settle, J. J., White, K. H., Milnes, M., Hindle, T. L., and Silleos, N. (1992). Linear mixture modeling applied to AVHRR data for crop area estimation, *International Journal of Remote Sensing*, *13*, 415–425.

Quintano, C., Fernández-Manso, A., Shimabukuro, Y. E., and Pereira, G. (2012). Spectral unmixing, *International Journal of Remote Sensing, 33*(17), 5307-5340.

Ridd, M. K. (1995). Exploring a V-I-S model for urban ecosystem analysis through remote sensing: comparative anatomy for cities, *Remote Sensing. J. Int., 16,* 2165- 2185.

Rutgers (Department of Marine and Coastal Sciences, (2015). *http://marine.rutgers.edu/main/Table/IMCS-Publications/,* date retrieeved 15.03.2015.

Sabins, F. F. (1987). *Remote sensing; principles and interpretation*, New York: W. H. Freeman. *http://www.ciesin.org/docs/005-477/005-477.html*, date retrieved 06.05.2014.

Scawthorn, C., Eidinger, J. M., and Schiff, A. J. (2005). Fire Following Earthquake, Technical Council on Lifeline Earthquake Engineering Monograph, *American Society of Civil Engineers, Reston, 26*

Schowengerdt, R. (1997). *Remote Sensing: Models and Methods for Image Processing,* 2nd edition, Academic Press, London.

SERDP, DoD's Environmental Research Programs, (2014). *http://www.gis.usu.edu/~doug/SERDP/tools/ATMOS/e.htm,* date retrieved 19.12.2012.

Settle, J. J., and Drake, N. A. (1993). Linear mixing and the estimation of ground cover proportions, *International Journal of Remote Sensing*, *15*, 2381– 239.

Singh, A. (1985). Thematic Mapper radiometric correction research and development results and performance, *Photogrammetric Engineering and Remote Sensing, 51*(9), 1379-1383.

Small, C. (2001a). Estimation of urban vegetation abundance by spectral mixture analysis, *International Journal of Remote Sensing*, *22*, 1305-1334.

Small, C. (2001b). Spectral dimensionality of urban radiance, *In Proceedings of 10th JPL Airborne Earth Science Workshop*, NASA Jet Propulsion Laboratory, Pasadena, CA.

Small, C. (2002). Multitemporal analysis of urban reflectance, *Remote Sensing of Environment, 81*, 427-442.

Small, C. (2004). The Landsat ETM+ spectral mixing space, *Remote Sensing of Environment, 93,* 1-17.

Small, C., and Milesi, C. (2013). Multi-scale standardized spectral mixture models, *Remote Sensing of Environment, 136*, 442-454.

Studley, H., and Weber, K. T. (2011). *Comparison of Image Resampling Techniques for Satellite Imagery,* Pages 185-196 in K. T. Weber and K. Davis (Eds.), Final Report: Assessing Post-Fire Recovery of Sagebrush-Steppe Rangelands in Southeastern Idaho, 252.

Sudhira, H. S., Ramachandra, T. V., and Jagdish, K. S. (2004) Urban sprawl: metrics, dynamics and modelling using GIS, *International Jour. Appl Earth Obs. Geoinf. 5*, 29–39.

Sunar, F. (1998). An analysis of changes in a multi-date data set: A case study in the Ikitelli area, Istanbul, Turkey, *International Journal of Remote Sensing*. doi:10.1080/014311698216215.

Taragi, R. C. S., and Pundir, P. P. S. (1997). Use of satellite data in urban sprawl and land use studies - a case of Lucknow city, *Jour. Indian Soc. Remote Sens. 25*(2), 113–118.

Teillet, P. M. (1986). Image correction for radiometric effects in remote sensing, *Int. Journal of Remote Sensing, 7(*12), 1637-1651.

Tompkins, S., Mustard, J. F., Pieters, C. M., and Forsyth, D. W. (1997). Optimization of endmembers for spectral mixture analysis, *Remote Sensing of Environment, 59*, 472-489.

TurkStat (Turkish Statistical Institute), (2014). Nüfus verisi ve yüzölçümü. *<http://www.tuik.gov.tr>*, date retrieved 25.06.2014.

Url-1 *< http://www.sc.chula.ac.th/courseware/2309507/Lecture/remote18.htm>* date retrieved 24.06.2014.

Url-2 *<http://eoimages.gsfc.nasa.gov/ve//1438/land_lights_16384.tif/>* date retrieved 07.03.2013.

Url-3 *< http://ngdc.noaa.gov/eog/dmsp/downloadV4composites.html/>* date retrieved 09.03.2013.

Url-4 *< http://cwcaribbean.aoml.noaa.gov/bilko/module7/lesson3/>* date retrieved 21.09.2013.

U.S. Congress, Office of Technology Assessment, (1994). Civilian Satellite Remote Sensing: A Strategic Approach, OTA-ISS-607, Washington, DC: U.S. *Government Printing Office*, September 1994.

USGS (United States Geological Survey), Global Visualization Viewer (Glovis) (2012). *http://glovis.usgs.gov/*, date retrieved 19.11.2012

USGS (United States Geological Survey), (2014). *http://landsat.usgs.gov/* , date retrieved 17.06.2014 and 08.04.2015.

Uysal, C., and Maktav D. (2015). Landsat Verileri ve Lineer Spektral Ayrıştırma (Unmixing) Yöntemi Kullanılarak İzmit Körfezi Çevresinde Kentsel Değişim Alanlarının Belirlenmesi, *Havacılık ve Uzay Teknolojileri Dergisi, 8*(1), 47-53.

Verbyla, D. L. (2002). *Practical GIS analysis*, London: Taylor & Francis application/agriculture/overview/agrio014pf.htm> accessed at 26.04.2014.

Wade, T., and Sommer, S. (2006). *A to Z GIS:* An illustrated dictionary of geographic information systems, *Journal of Planning Literature*, 23, doi:10.1177/0885412208327016.

Weng, Q. (2009). *Remote Sensing and GIS Integration: Theories, Methods, and Applications,* 1st Edition*,* ISBN-13: 978-0071606530, McGraw-Hill Professional, New York, 416 pages.

Wu, C., and Murray, A. T. (2002). Estimating impervious surface distribution by spectral mixture analysis, *Remote Sensing of Environment*, *84,* 493-505.

Yagi, H., Hesiletu, M. H., and Nishio F. (2010). Estimation of Night Light from the DMSP/OLS, *International Archives of the Photogrammetry, Remote Sensing and Spatial Information Science*, *38*(8), Kyoto, Japan.

Yale University, (2014). *http://www.yale.edu/ceo /Projects/swap/landcover/ Unsupervised_classification.htm,* date retrieved 04.05.2014.

YCEO, (2010). Converting Digital Numbers to Top of Atmosphere (ToA) Reflectance, The Yale Center for Earth Observation, *http://www.yale.edu/ceo,* date retrieved 11.02.2013.

Zhu, L., and Tateishi, R. (2001). Application of Linear Mixture Model to Time Series AVHRR NDVI Data, *22nd Asian Conference on Remote Sensing*, 5-7 November, Singapore.

APPENDICES

APPENDIX A.1: Global Endmember Table.

Table A.1 : Global Endmember Table.

λ	S	V	D
0.479	0.265	0.095	0.074
0.561	0.351	0.088	0.045
0.661	0.403	0.048	0.023
0.835	0.518	0.619	0.015
1.651	0.561	0.193	0.003
2.208	0.477	0.065	0.001

CURRICULUM VITAE

Name Surname: Cihan Uysal

Place and Date of Birth: Salihli, 1 April 1981

E-Mail: uysalc@yahoo.com

EDUCATION:

B.Sc.: ITU Geodesy and Photogrammetry

M.Sc.: ITU Geomatics Engineering

PROFESSIONAL EXPERIENCE AND REWARDS:

Project Experience

- The application of remote sensing and field surveys to investigate the late Roman and Byzantine water supply system of Istanbul, 2007-2009 (TÜBİTAK project #106K350).
- Gaining additional urban space, 2009-2012 (TÜBİTAK IntenC project no# 108Y247) website: www.gaus-project.info.

Rewards

- TÜBİTAK (The Scientific and Technological Research Council of Turkey) 2214 PhD Thesis Research Grant (2012-2013), Columbia University in New York City, USA.

PUBLICATIONS, PRESENTATIONS AND PATENTS ON THE THESIS:

▪ **Uysal C**., and Maktav D. (2015). Landsat Verileri ve Lineer Spektral Ayrıştırma (Unmixing) Yöntemi Kullanılarak İzmit Körfezi Çevresinde Kentsel Değişim Alanlarının Belirlenmesi. *Havacılık ve Uzay Teknolojileri Dergisi, 8*(1), sayfa 47-53, Ocak 2015, İstanbul, Türkiye (Makale).

▪ **Uysal C**., and Maktav D. (2014). Determination of urban development in Istanbul by using the spectral unmixed Landsat images. *EARSeL 34th Symposium*, 16-20 June 2014, Warsaw, Polond (paper/oral presentation).

▪ **Uysal C**., and Maktav D. (2014). DMSP-OLS ve Landsat verileri ve Lineer Spektral Unmixing yöntemi kullanılarak kentsel değişim alanlarının belirlenmesi: İzmit örneği, *UZAL-CBS Sempozyumu*, 14-17 Ekim 2014, YTÜ, İstanbul,Türkiye (Bildiri/Sözlü sunum).

OTHER PUBLICATIONS, PRESENTATIONS AND PATENTS :

- Akar, I., **Uysal, C**., and Maktav, D. (2008). Determination Of Natural Disaster Risks By Integration Of Remote Sensing And Gis: A Case Of Yeniciftlik Stream Basin Model In Istanbul/Turkey, *ISPRS Symposium*, 3-11 July 2008, Beijing, China (paper/oral presentation).

- Maktav, D., Akar, I., and **Uysal, C**. (2008). Determination of Flood Risks Using Remote Sensing and GIS techniques in Yeniçiftlik Stream Basin. *European Association of Remote Sensing Laboratories (EARSeL 28th)*, 2-5 June 2008, Istanbul, Turkey (paper/poster presentation).

- Maktav, D., Crow, J., Kolay, C., Yeğen, B., Önöz, B., Sunar, F., Coşkun,G., Karadoğan, H., Çakan, M., Akar, İ., **Uysal, C**., Güçlüer, D., Geze,B., İnce, G. (2008). Arkeolojide uzaktan algılama ve CBS entegrasyonu, *Uzaktan Algılama – Coğrafi Bilgi Sistemleri Sempozyumu (UZAL-CBS 2008)*, 13-15 Eylül 2008, Kayseri, Türkiye (Bildiri).

- **Uysal, C**., Maktav, D., and Crow, J. (2008). Su Kemerlerinin 3d Modellenmesinde Uzaktan Algılama ve CBS Kullanımı; Kurşunlugerme/İstanbul Örneği. *Uzaktan Algılama – Coğrafi Bilgi Sistemleri Sempozyumu (UZAL-CBS 2008)*, 13-15 Eylül 2008, Kayseri, Türkiye (Bildiri/poster sunum).

- Maktav, D., Crow, J., Kolay, C., Yeğen, B., Önöz, B., Sunar, F., Coşkun,G., Karadoğan, H., Çakan, M., Akar, İ., **Uysal, C**., Güçlüer, D., Geze,B., İnce, G. 2009: A Integration Of Remote Sensing And GIS For Archaeological Investigations, *International Journal Of Remote Sensing*, *30*(7), 1661-1674 (SCI article).

- Maktav, D., Crow, J., Kolay, C., Yeğen, B., Önöz, B., Sunar, F., Coşkun,G., Karadoğan, H., Çakan, M., Akar, İ., **Uysal, C**., Güçlüer, D., Geze,B., İnce, G. 2009: A Study in the Application of Remote Sensing and GIS for the Archaeology of the Hinterland of Medieval Constantinople/Istanbul, *29. EARSeL Symposium and Workshops*, 15-18 June 2009, Crete, Greece (paper).

- Thunig, H., Wolf, N., Naumann, S., Siegmund, A., Jürgens, C., **Uysal, C**., and Maktav, D. 2011: Land use/land cover classification forapplied urban planning - the challenge of automation, in *Proc. JURSE*, 11-13 April 2011, pp. 229 – 232 (paper).

- Carsten Jurgens, Nils Wolf, Alexander Siegmund, Derya Maktav, Filiz Sunar, Hayriye Eşbah, Tüzin Baycan, **Cihan Uysal**, Kaan Kalkan, Onat Yiğit Mercan, İrfan Akar, 2011: Extraction and Multi-criteria Evaluation of Potential Space for Inner-Urban Development by Means of Optical VHR Satellite Imagery, *Geomatics Technologies in the City, (GTC)*, Jeddah, 10-13 May 2011, http://geomaticsksa.com/GTC2011/S2/PDF/11.pdf (paper).

- Derya Maktav, Carsten Jurgens, Alexander Siegmund, Filiz Sunar, Hayriye Eşbah, Kaan Kalkan, **Cihan Uysal**, Onat Yiğit Mercan, İrfan Akar, Holger Thunig, Nils Wolf, 2011: Multi-Criteria Spatial Decision Support System for Valuation of Open Spaces for Urban Planning, *5th International Conference on Recent Advances in Space Technologies (RAST)*, İstanbul, 09-11 June 2011, http://dx.doi.org/10.1109/RAST.2011.5966812 (paper).

- Holger Thunig, Carsten Jurgens, Alexander Siegmund, Derya Maktav, Filiz Sunar, Hayriye Eşbah, Tüzin Baycan, **Cihan Uysal**, Kaan Kalkan, Onat Yiğit Mercan, 2011: Potential Open Space Detection and Decision Support for Urban Planning by Means of Optical VHR Satellite Imagery, *31st EARSeL Symposium*, Prague, Czech Republic, 30.05.2011-02.06.2011, http://kaankalkan.com/pub/open_space_detection_earsel_2011.pdf (paper).

- **Cihan Uysal**, Derya Maktav, 2011: Comparison of the Accuracies of DTM's Obtained from SRTM, Topographic Maps and ALOS PRISM. *31st EARSeL Symposium*, 30.05.2011-02.06.2011, Prague, Czech Republic (Poster/paper).